DOT/FAA/TC-12/5

Federal Aviation Administration
William J. Hughes Technical Center
Aviation Research Division
Atlantic City International Airport
New Jersey 08405

Application of Rotorcraft Damage Tolerance Methodology to Rotor Masts

October 2012

Final Report

This document is available to the U.S. public through the National Technical Information Services (NTIS), Springfield, Virginia 22161.

This document is also available from the Federal Aviation Administration William J. Hughes Technical Center at actlibrary.tc.faa.gov.

U.S. Department of Transportation
Federal Aviation Administration

NOTICE

This document is disseminated under the sponsorship of the U.S. Department of Transportation in the interest of information exchange. The U.S. Government assumes no liability for the contents or use thereof. The U.S. Government does not endorse products or manufacturers. Trade or manufacturer's names appear herein solely because they are considered essential to the objective of this report. The findings and conclusions in this report are those of the author(s) and do not necessarily represent the views of the funding agency. This document does not constitute FAA policy. Consult the FAA sponsoring organization listed on the Technical Documentation page as to its use.

This report is available at the Federal Aviation Administration William J. Hughes Technical Center’s Full-Text Technical Reports page: actlibrary.tc.faa.gov in Adobe Acrobat portable document format (PDF).

Technical Report Documentation Page

1. Report No. DOT/FAA/TC-12/5	2. Government Accession No.	3. Recipient's Catalog No.
4. Title and Subtitle APPLICATION OF ROTORCRAFT DAMAGE TOLERANCE METHODOLOGY TO ROTOR MASTS		5. Report Date October 2012 6. Performing Organization Code
7. Author(s) X. Li, B.R. Krasnowski, S. Lin, W.P. Green, R.L. Mueller, and C.J. Tzeng		8. Performing Organization Report No.
9. Performing Organization Name and Address Bell Helicopter Textron Inc. P.O. Box 482 Fort Worth, TX 76101		10. Work Unit No. (TRAIS) 11. Contract or Grant No. DTFACT-07-C-00009
12. Sponsoring Agency Name and Address U.S. Department of Transportation Federal Aviation Administration Southwest Region – Aircraft Certification Service, Rotorcraft Directorate 2601 Meacham Blvd. Fort Worth, TX 76137		13. Type of Report and Period Covered Final Report 2/2007 – 1/2011 14. Sponsoring Agency Code ASW-112

15. Supplementary Notes

The Federal Aviation Administration William J. Hughes Technical Center Aviation Research Division COR was Ms. Traci Stadtmueller.

16. Abstract

The purpose of this research was to develop a practical rotorcraft damage tolerance (RCDT) methodology for the rotorcraft drive system, using a rotor mast for demonstration. The research effort focused on gaining a better understanding of (1) the mixed-mode crack growth behavior driven by the complex loading of thrust, bending, and torque; (2) the effect of residual stresses induced during the heat and surface treatments on the damage tolerance (DT) characteristics of drive system parts; (3) fatigue crack growth (FCG) properties and behavior of rotorcraft drive system materials; and (4) crack growth analysis (CGA) capability for rotorcraft drive system DT analysis.

The technical approach addressed three key technical elements: (1) DT certification testing for crack growth parameters, (2) FCG analysis capability, and (3) effects of the residual stresses on life enhancement. A fracture mechanics-based CGA method was used to evaluate the FCG in a rotor mast. A building-block approach was employed as a baseline for development of the DT certification test method, which was tied with FCG analysis for implementation of data inputs and CGA verification. Evaluations of life enhancement methods were aligned with the baseline test program to support and validate the CGA. The method was validated by crack growth tests at the coupon and element levels.

The material threshold data were obtained. The element tests generated detailed information on the FCG pattern with the given loads, verified the damage-tolerant critical design features, and provided guidance for the full-scale tests. The current NASGRO® Fracture Mechanics and Fatigue Crack Growth Analysis Software CGA capability for FCG analysis of a rotorcraft drive system was evaluated. The comparability of the analysis results versus surface flaw FCG (Kb-Bar) and fillet radius element test data confirmed the feasibility of the NASGRO FCG analysis. The potential of the finite element analysis tool ANSYS® for rotorcraft drive system CGA was also evaluated. ANSYS demonstrated advantages in stress-intensity factor computation. It allowed users to implement macros to perform CGA. Although ANSYS is not ideal for CGA, its capabilities may be expanded to cover this special area of analysis in the future.

The effect of residual stress on FCG behavior of rotor mast was investigated by testing and analysis. Kb-Bar and fillet radius element were used. The as-machined, shot-peened, and carburized surface conditions were considered. The existence of residual stress (1) changed the stress ratio on the surface layer, (2) affected the crack shape, and (3) delayed the crack initiation.

Further investigation and data are needed to understand and model the FCG behavior with surface treatments. A full-scale evaluation is necessary to prove the applicability of the RCDT technologies to the drive system.

17. Key Words Damage tolerance, Rotorcraft, Drive system, Mast	18. Distribution Statement This document is available to the U.S. public through the National Technical Information Service (NTIS), Springfield, Virginia 22161. This document is also available from the Federal Aviation Administration William J. Hughes Technical Center at actlibrary.tc.faa.gov.

19. Security Classif. (of this report) Unclassified	20. Security Classif. (of this page) Unclassified	21. No. of Pages 123	22. Price

Form DOT F 1700.7 (8-72) Reproduction of completed page authorized

TABLE OF CONTENTS

			Page
EXECUTIVE SUMMARY			xiii
1.	INTRODUCTION		1
	1.1	Background	1
	1.2	Program Objectives and Goals	2
	1.3	Technical Approach	2
2.	THE DT CERTIFICATION TEST METHOD FOR ROTOR MAST		3
	2.1	Building-Block Approach	4
	2.2	The M(T) Tests	5
		2.2.1 The M(T) Test Requirements and Test Matrix	6
		2.2.2 The M(T) Test Results	6
		2.2.3 Discussion of M(T) Test Results	7
	2.3	The Kb-Bar Tests	8
		2.3.1 The Kb-Bar Test Matrix	8
		2.3.2 The Kb-Bar Test Results	9
		2.3.3 Comparison of 4340 Steel and 9310 Steel Kb-Bar Test Results	13
		2.3.4 Comparison of Kb-Bar and M(T) Test Results	14
	2.4	Element Test Program	15
		2.4.1 Test Matrix and Loads	16
		2.4.2 Element Testing Fixture Design	18
		2.4.3 Element Test Results	18
		2.4.4 Discussion of Element Test Results	22
3.	EVALUATION OF CGA CAPABILITY OF CURRENT ANALYSIS TOOLS (TASK 4)		23
	3.1	Evaluation of Current NASGRO CGA Capability	24
		3.1.1 The Kb-Bar FCG Simulation Using NASGRO	25
		3.1.2 The NASGRO Kb-Bar Simulation Results	32
		3.1.3 Fillet Radius FCG Analysis With NASGRO: SIF Solutions	38
		3.1.4 Fillet Radius FCG Analysis With NASGRO: CGA	45
		3.1.5 The Current NASGRO CGA Capability	49

3.2 Evaluation of ANSYS on CGA Capability 50

3.2.1 The Kb-Bar SIF Solutions With ANSYS 51
3.2.2 ANSYS FCG Analysis of Kb-Bar 57
3.2.3 Modeling of Fillet Radius Subelement With ANSYS Workbench™ 63
3.2.4 ANSYS SIF Solutions for Crack at Fillet Radius Element Specimen 65
3.2.5 ANSYS FCG Analysis for Fillet Radius Element Specimen 71

4. EVALUATION OF LIFE ENHANCEMENT METHODS ON ROTOR MAST 74

4.1 Residual Stress of As-Machined Baseline Kb-Bar 75
4.2 Residual Stress Profiles 76

4.2.1 In-Depth Residual Stress Profiles 76
4.2.2 Residual Stress on Surfaces 77

4.3 Effect of Residual Stress on Kb-Bar FCG 79

4.3.1 The FCG Behavior of Baseline Kb-Bar With As-Machined Residual Stress 79

4.3.2 The FCG Behavior of Shot-Peened Kb-Bar 81

4.3.3 The FCG Behavior of Carburized Kb-Bar 83

4.3.4 Comparison of Kb-Bar Test Results Between Baseline and Shot-Peened Specimens 84

4.3.5 The Kb-Bar CGA Results of Shot-Peened vs Baseline 85

4.4 Effect of Residual Stress on Fillet Element FCG 85

5. SUMMARY 86

6. REFERENCES 89

APPENDICES

A—Fatigue Crack Growth Properties of 4340 Steel and 9310 Steel
B—Stess-Intensity Factor Solution for Fillet Radius Element
C—Flow Charts for Kb-Bar Stess-Intensity Factor Solution
D—Residual Stress Distributions in 4340 Steel and 9310 Steel Kb-Bars

LIST OF FIGURES

Figure		Page
1	Illustration of Rotorcraft Main Rotor Mast	1
2	Key Elements of the Technical Approach	3
3	Load Conditions for Rotor Mast DT Testing and Analysis	4
4	The M(T) Coupon	5
5	The 4340 Steel M(T) FCG Curves: R = -1, -0.5, 0.05, 0.5, and 0.8	6
6	The 9310 Steel M(T) FCG Curves: R = 0.05, 0.5, and 0.8	7
7	The Kb-Bar Specimen	8
8	The 4340 Steel Kb-Bar Baseline Test Results: R = -1, 0.05, and 0.8	10
9	The 4340 Steel Shot-Peened Kb-Bar FCG Curves: R = -1, 0.05, and 0.8	11
10	The 9310 Steel Baseline, Shot-Peened, and Carburized Kb-Bar FCG Curves: R = 0.05	12
11	Comparison of 4340 Steel and 9310 Steel Kb-Bar *da*/*dN*	13
12	Comparison Between Kb-Bar and M(T) *da*/*dN* Curves of Baseline 4340 Steel Coupons	14
13	Comparison of Kb-Bar and M(T) *da*/*dN* Data (9310 Steel, R = 0.05)	15
14	Fillet Radius Element Test Specimen	16
15	The FE Model of the Fillet Radius Element Specimen	17
16	Calculated Crack Plane Normals (for Notch Orientation)	17
17	Fillet Element Test Setup	18
18	Crack Depth (a) vs Cycles for M = T Loading Case	20
19	Crack Chordal Length (2c) vs Cycles for M = T Loading Case	20
20	Crack Depth (a) vs Cycles for M = 2T Loading Case	21

21	Crack Chordal Length (2c) vs Cycles for M = 2T Loading Case	21
22	Crack Shape Aspect Ratio of Baseline Fillet Radius Element FCG	22
23	Crack Shape Aspect Ratio of Shot-Peened Element Specimen FCG	22
24	Evaluation of the Capability of CGA Analysis Tools	24
25	The NASGRO SC17 Model for SIF Solution	26
26	Stress History Applied in Load-Shedding Simulation (Case 3)	29
27	The NASGRO Equation Curve Fits for 4340 Steel M(T) FCG Data	31
28	Crack Growth Rate History in Case 1: Kb-Bar Simulations as a Function of ΔK (R = 0.05)	32
29	Calculated Crack Size History in Case 1: Kb-Bar Load-Shedding Simulation (R = 0.05)	33
30	Crack Growth Rate History in Case 1: Kb-Bar Load-Shedding Simulations With Strip-Yield and Noninteraction Models (R = 0.05)	33
31	Calculated Crack Size History of Kb-Bar Simulation With Residual Stress (R = 0.05)	34
32	The *a*-N Curves for Baseline 4340 Steel Kb-Bar Specimen With Load Shedding (a) NASGRO Simulation With Default Material Properties, (b) NASGRO Simulation With 20% Reduced Crack Growth Rate, and (c) Testing *a*-N Curve	35
33	Variation of da/dN (dc/dN) vs ΔK During FCG Simulation of (a) Baseline and (b) Shot-Peened Kb-Bar (4340 Steel)	36
34	Variation of Stress Ratio (R) as a Function of Cycles for (a) Baseline and (b) Shot-Peened Kb-Bar	36
35	The da/dN vs ΔK for Baseline Kb-Bar (a) R = 0.05 and (b) R = -1	37
36	The *a*-N and *c*-N Comparison for Baseline Kb-Bar	37
37	The *a*-N and *c*-N Comparison for Shot-Peened Kb-Bar	38
38	Fillet Radius Element Geometry for the NASGRO Analysis	39
39	Crack Position of the Fillet Radius Element for the NASGRO Analysis	39
40	The FADD-3D Hybrid FE/BE Model of the Fillet Radius Element for SIF Solutions	41

41	The SIF Solutions as a Function of Elliptical Angle Subjected to Remote Tension	41
42	The SIF Solutions as a Function of Elliptical Angle Subjected to Remote Bending	41
43	The SIF Solutions as a Function of Elliptical Angle Subjected to Remote Torsion	42
44	Actual Test Specimen Geometries of the Fillet Radius Element for SIF and NASGRO Simulation	42
45	The SIF Solution Matrix for Actual Test Loading Conditions	43
46	Boundary Element Section of Hybrid Models for a 30° Crack in a Fillet Radius Element (a) Irregular Surface Crack and (b) Irregular Through-Thickness Crack	44
47	Normalized SIF Variations Along the Crack Front of Surface Crack (θ = 30°, a/t = 0.04484, and a/c = 0.5 under remote shear)	44
48	The SIF Variations Along the Crack Tip Perimeter of c_2-Tip of Through-Thickness Crack (θ = 15° and $c_1 = c_2$ = 0.223 in., under remote shear)	45
49	Computed Crack Lengths as a Function of Fatigue Life Cycles Based on NASGRO Library Material Data (a) M = T Load Case and (b) M = 2T Load Case	47
50	Computed Crack Lengths as a Function of Fatigue Life Cycles Based on M(T) Test Data (a) M = T Load Case and (b) M = 2T Load Case	48
51	Comparison of Test Data and NASGRO Simulation: *a*-N Curves for Baseline Fillet Radius Element With (a) M = T Load Case and (b) M = 2T Load Case	48
52	The CGA	51
53	An FE Model of Kb-Bar Configuration	52
54	Half a Kb-Bar FE Model With the Elliptical Crack Surface	52
55	Stress Fields in Crack Area of a Kb-Bar Specimen	52
56	β vs a/t for the Kb-Bar With a Semicircular Crack	53
57	β vs a/t for Kb-Bar of a Semielliptical Crack With a/c = 0.8	54
58	A Semicircular Crack Displacement-Controlled SIF Solution of a Kb-Bar	55
59	Residual Stress Distribution Used for Analysis	56

60 The K_I Distribution Along a Semielliptical Crack Front Embedded in a Kb-Bar With Imposed Residual Stress (a = 0.050 and c = 0.063) 56

61 The SIF Solutions of a Kb-Bar With a Semielliptical Crack Under Applied Stresses (a = 0.050 and c = 0.063) 57

62 Flow Chart of Kb-Bar's CGA 58

63 The a-N Curves of a Kb-Bar CGA Using ANSYS 59

64 Crack Growing From Kb-Bar CGA Using ANSYS 59

65 ANSYS Kb-Bar da/dN With the Crack Closure Effect Considered, Using Elber's Equation and SwRI f-Value, Compared to the Test Data for a Kb-Bar With R = 0.05 60

66 ANSYS Kb-Bar dc/dN With the Crack Closure Effect Considered, Using Elber's Equation and SwRI f-Value, Compared to the Test Data for a Kb-Bar With R = 0.05 61

67 ANSYS Kb-Bar a-N Curves With the Crack Closure Effect Considered, Using Elber's Equation and SwRI f-Value, Compared to the Test Data for a Kb-Bar With R = 0.05 61

68 ANSYS Kb-Bar da/dN With the Crack Closure Effect Considered, Using Elber's Equation and SwRI f-Value, Compared to the Test Data for a Kb-Bar With R = 0.8 62

69 ANSYS Kb-Bar dc/dN With the Crack Closure Effect Considered, Using Elber's Equation and SwRI f-Value, Compared to the Test Data for a Kb-Bar With R = 0.8 62

70 ANSYS Kb-Bar a-N Curves With the Crack Closure Effect Considered, Compared to the Test Data With R = 0.8 63

71 Solid Model Geometry of the Fillet Radius Element Shown With Spline in Crack Region and Without 63

72 An FE Mesh of the Fillet Radius Element Without Spline in Crack Region 64

73 Boundary Conditions of the Fillet Radius Element 64

74 Fillet Radius Element Principal Stress (S_1) Contours for the Bending Equal to the Torsion Load Condition 65

75 Fillet Radius Element Principal Stress (S_1) Contours at the Fillet Radius for the Bending Equal to Twice the Torsion Load Condition 65

76 Typical FE Mesh for the Fillet Radius Surface Crack, Excluding Residual Stress Effects 66

77 The SIF Solutions for the Fillet Radius Surface Crack Under Thrust, Bending, and Torsion (crack plane orientation: 0°, 15°, 30°, and 45°) 66

78 Local Refinement of the FE Mesh for the Fillet Radius Surface Crack, Including Residual Stress Effects 67

79 The SIF Solutions for the Fillet Radius Surface Crack Oriented at 0° Under 0-, 5-, 20-, 35-, and 50-ksi Thrust, Bending, and Torsion, Including Residual Stress 68

80 The SIF Solutions for the Fillet Radius Surface Crack Oriented at 15° Under 0-, 5-, 20-, 35-, and 50-ksi Thrust, Bending, and Torsion, Including Residual Stress 69

81 The SIF Solutions for the Fillet Radius Surface Crack Oriented at 30° Under 0-, 5-, 20-, 35-, and 50-ksi Thrust, Bending, and Torsion, Including Residual Stress 70

82 The SIF Solutions for the Fillet Radius Surface Crack Oriented at 45° Under 0-, 5-, 20-, 35-, and 50-ksi Thrust, Bending, and Torsion, Including Residual Stress 71

83 Definition of Crack Local Coordinate System 72

84 The K_I RSs for Fillet Radius Surface Crack 73

85 Paris Region Properties Used in the CGA 73

86 The CGA of the Fillet Radius Surface Crack With two Loading Conditions and an Initial Flaw Size of $a = c = 0.015''$ 74

87 Profiles of Residual Stress In-Depth for 4340 Steel and 9310 Steel Kb-Bars 77

88 The *a*-N and *c*-N Curves of Baseline Kb-Bar Tests During Load Shedding (4340 Steel) 79

89 Crack Front Aspect Ratio Comparison of Simulation to Test—Baseline 80

90 Crack Growth Scenario of Baseline Kb-Bar With As-Machined Residual Stress 80

91 Crack Front Profile of Baseline Kb-Bar With As-Machined Residual Stress 80

92 The *a*-N and *c*-N Curves of Shot-Peened Kb-Bar Tests During Load Shedding (4340 Steel) 81

93 Crack Front Aspect Ratio Comparison of Simulation to Testing—Shot-Peened Kb-Bar Tests 82

94 Crack Growth Scenario in the Shot-Peened Kb-Bar Tests 82

95 Typical Shot-Peened Kb-Bar Specimen 82

96 Shot-Peened Kb-Bar Specimen 105-7, Showing Marker Bands 83

97 Predicted Crack Surface of a Carburized 9310 Steel Kb-Bar Specimen 83

98 Actual Crack Surface of a Carburized 9310 Steel Kb-Bar Specimen 84

99 Baseline and Shot-Peened Kb-Bar FCG Curves: R = -1, 0.05, and 0.8 (4340 Steel) 84

LIST OF TABLES

Table		Page
1	Materials and Test Methods for the Building-Block Tests	5
2	The M(T) Coupon Test Matrix	6
3	Test Matrix for Kb-Bar Specimens	9
4	Test Conditions and Results for 4340 Steel Baseline Kb-Bar Tests	9
5	Test Results for 4340 Steel Shot-Peened Kb-Bar Tests	10
6	The 9310 Steel Baseline Kb-Bar Test Results	11
7	Test Results of 9310 Steel Carburized Kb-Bar Tests	12
8	The 9310 Steel Shot-Peened Kb-Bar Test Results	13
9	Fillet Element Test Matrix	16
10	Crack Plane Normal Angles (for Notch Orientation)	17
11	Baseline Fillet Element Specimen Test Summary	19
12	Shot-Peened Fillet Element Specimen Test Summary	19
13	Challenges of Applying DT Method to a Rotor Mast	24
14	The FCG Analysis Matrix Using NASGRO	25
15	Loads for Kb-Bar Simulation (Cases 1 and 2)	27
16	Residual Stress Gradient for Kb-Bar FCG Simulation	27
17	Specified Load Shedding History for Kb-Bar Analysis	28
18	Initial Crack Sizes Kb-Bar FCG Simulation (Cases 4 and 5)	30
19	Residual Stress Distribution	30
20	Key Parameters Derived From NASGRO Equation Fit	31
21	Analysis Matrix for SIF Solutions of the Fillet Radius Element	40
22	Crack Geometry Variations	40
23	Alternative Fillet Element Geometry Variations	40
24	Actual Testing Loads for NASGRO Simulation of Baseline Fillet Element Specimen	43
25	Predicted Fatigue Life of Fillet Radius Element (Baseline)	47
26	Average Stress Relief Results for Each Process	76
27	Test Matrix for Residual Stress In-Depth	76
28	Residual Stress In-Depth of Kb-Bar Test Coupons	77
29	The Kb-Bar Specimen Residual Stress Profile	78

LIST OF SYMBOLS AND ACRONYMS

da/dN	Crack *a*-tip growth rate (in/cycle)
dc/*dN*	Crack *c*-tip growth rate (in/cycle)
2D	Two-dimensional
3D	Three-dimensional
a/c	Crack shape aspect ratio
BE	Boundary element
BH	Bell Helicopter
CGA	Crack growth analysis
CP	Critical part
DT	Damage tolerance
EDM	Electrical discharge machining
FAA	Federal Aviation Administration
FCG	Fatigue crack growth
FE	Finite element
FEA	Finite element analysis
Kb-Bar	Surface flaw fatigue crack growth
M(T)	Middle tension
PD	Potential drop
RCDT	Rotorcraft damage tolerance
RS	Response surface
SIF	Stress-intensity factor
SwRI®	Southwest Research Institute®
TRL	Technology readiness level

EXECUTIVE SUMMARY

The purpose of this research was to develop a practical rotorcraft damage tolerance (RCDT) methodology for the rotorcraft drive system, using a rotor mast for demonstration. The research focused on gaining a better understanding of (1) the mixed-mode crack growth behavior driven by the complex loading of thrust, bending, and torque, as the rotor mast is usually subjected to; (2) the effect of residual stresses induced during the heat and surface treatments on the damage tolerance (DT) characteristics of drive system parts; (3) fatigue crack growth (FCG) properties and behavior of rotorcraft drive system materials and the effect of specimen and test conditions to FCG data; and (4) crack growth analysis (CGA) capability for rotorcraft drive system.

The technical approach addressed three key technical elements: (1) DT certification testing for crack growth parameters, (2) FCG analysis capability that can account for manufacturing deviations in geometrical details such as radii, and (3) effects of the residual stresses on life enhancement. A fracture mechanics-based CGA method was used to evaluate the FCG in a rotor mast. A building-block approach was used as a baseline for developing the DT certification test method, tied with fatigue crack analysis for implementation of data inputs and CGA verification. Evaluations of life enhancement methods were aligned with the baseline testing program to validate the CGA. The method was validated by crack growth testing at the coupon and element levels.

The building-block certification tests were performed at the coupon and element levels. The material threshold data were obtained by using the middle tension test method. The surface flaw FCG (Kb-Bar) specimen was used to demonstrate the effect of surface conditions on the growth of a part-through surface crack. The element tests generated detailed information on the FCG pattern with the given loads, verified the DT critical design features, and provided guidance for full-scale tests.

The current CGA capability of NASGRO® Fracture Mechanics and Fatigue Crack Growth Analysis Software was evaluated for the FCG analysis of rotorcraft drive systems. Although simplifications were made to accommodate the limitation of the tool, to improve computational efficiency, and to reduce the probability of inaccuracy in complex modeling, the consistency between the analysis results and the fillet radius element test data confirmed the feasibility of NASGRO for FCG analysis. The potential of the finite element analysis tool ANSYS® for rotorcraft drive system CGA was evaluated with the Kb-Bar and fillet radius element configuration. ANSYS demonstrated advantages in stress-intensity factor computation due to its strength in modeling and stress analysis. It has a great capability for implementing a crack with complex geometries. ANSYS allows users to input macros to perform CGA, although it was not originally designed for this purpose. For simple geometries like Kb-Bar, the CGA can be automated for efficiency. However, it is difficult to automate the analysis for complex components, such as the fillet radius element, because the modeling requires user inputs for each crack extension. Even though ANSYS is currently not ideal for CGA, its capabilities may be expanded by the software developer in the future to cover this special area of analysis.

Testing and analysis was used to investigate the effect of residual stress on FCG behavior of the rotor mast. Kb-Bar and fillet radius element were used. As-machined, shot-peened, and

carburized surface conditions were considered. It was found that existence of residual stress (1) changed the stress ratio on the surface layer, (2) affected the crack shape, and (3) delayed the crack initiation.

Further investigation and data are needed to understand and model the FCG behavior with surface treatments. Full-scale part evaluation is necessary to prove the applicability of the RCDT technologies to the drive system.

1. INTRODUCTION.

1.1 BACKGROUND.

Crack growth damage tolerance (DT) technology has been successfully used in fixed-wing structures and engine components. However, rotorcraft pose unique requirements for DT design and certification due to the complexity of the structure and loading conditions. Over the past two decades, the Federal Aviation Administration (FAA) and the rotorcraft industry have made significant efforts to leverage this technology in addition to the traditional safe-life approach. While the technology development shows promise, application of the DT methodology to rotorcraft structures remains challenging. The challenges are associated with the complexity of structural configurations and loading (highly mixed high-cycle and high-load/low-cycle environment), the incomplete crack growth material properties database, and the lack of the availability of analytical tools that can predict complex, three-dimensional (3D), nonplanar crack growth behavior under these conditions. These difficulties have hindered the application of DT technology to rotorcraft structures, particularly the dynamic rotor and drive system components [1-31].

The rotor mast, which is a critical part (CP), is an extremely challenging area to apply the rotorcraft DT (RCDT) method. As shown in figure 1, a rotor mast is a vital component of each rotorcraft, and the diameter of this part can directly affect the size of the transmission and rotor components that support it. Failure in a rotor mast, which is nonredundant, would result in the loss of the aircraft. In addition, rotor masts, which are made from high-purity steel forgings, are subjected to finely tuned heat and surface treatments to obtain the best static and fatigue performance. The complex stress field created at the stress concentration areas, such as fillet radii and splines, must be considered, as they are sensitive to crack growth. Together, these issues make DT of the rotor mast highly desirable, giving robustness to the CP at minimum weight and cost growth.

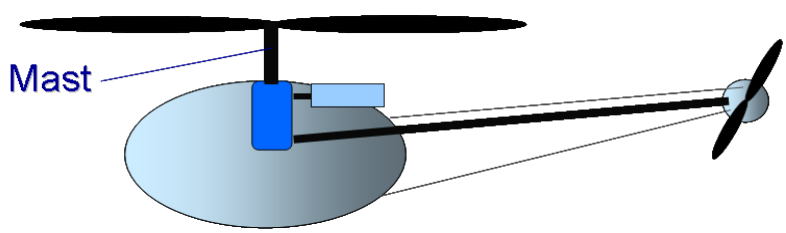

Figure 1. Illustration of Rotorcraft Main Rotor Mast

This research focused on gaining a better understanding of

- the mixed-mode crack growth behavior driven by the complex loading of thrust, bending, and torque, as the rotor mast transfers the rotor lift and bending loads to the transmission case, and provides the torque to the hub during ground and flight operations

- the effect of residual stresses induced during the heat and surface treatments on the DT characteristics of the rotor mast

- the effect of the complex geometrical details, such as fillet radii, flanges, and splines

- the effect of the usage spectra on the crack growth in rotor masts, as rotor masts are sensitive to the ground-air-ground cyclic loading resulting from the torque cycles (e.g., the repeated heavy lift cycles accumulated during logging missions and one-per-revolution cycles from shear loading)

The research addressed these areas by developing an RCDT methodology applicable to rotorcraft drive systems to advance the state-of-the-art technology. A subelement of representative rotor mast geometry was designed and tested for demonstrating the RCDT methodology at the element level. Based on the outputs of this research, the full-scale demonstration can be further conducted upon availability of FAA funding, which will validate the methodology as a complete building-block approach and support FAA DT certification requirements, such as FAA Title 14 Code of Federal Regulations 29.571.

1.2 PROGRAM OBJECTIVES AND GOALS.

The goal of the program was to develop a practical RCDT methodology for the rotorcraft drive system, demonstrated on a rotor mast from the selected rotorcraft, to meet the FAA DT certification requirements and support FAA rulemaking. The focus was to (1) improve safety and reliability while reducing maintenance time and cost, (2) potentially reduce the weight of rotor masts and other drive system parts, and (3) improve the technology readiness level (TRL) of the RCDT methodology.

The technical objectives were to:

- Develop a DT certification test methodology for the rotor mast, and be applicable to other drive system parts.

- Understand the current technology status and potential of crack growth analysis (CGA) capability for the rotor mast and other transmission components.

- Understand the effects of residual stress on fatigue crack growth (FCG) life of rotor mast and transmission components.

The TRL levels for the abovementioned areas were TRL 3 and TRL 4 [32] at the beginning of the program and they were TRL 5 and TRL 6 at its conclusion [32]. The methodology provides guidance in performing DT analysis, design, and certification of rotor masts and other drive system components. The methodology is applicable to different material systems and surface treatment conditions.

1.3 TECHNICAL APPROACH.

The technical approach addressed the following three key technical elements:

- DT certification test for crack growth parameters

- FCG analysis capability that can account for manufacturing deviations in geometrical details such as radii

- Effects of the residual stresses on life enhancement, as shown in figure 2

The overall approach was to use fracture mechanics based on the CGA method to evaluate the FCG in a rotor mast. A building-block approach was used as a baseline for development of the DT certification test method, in conjunction with FCG analysis as an implementation of data inputs and CGA verification. Evaluations of life enhancement methods were aligned with the baseline test program to support and validate the CGA. The method was validated by CGA tests at the coupon and element levels.

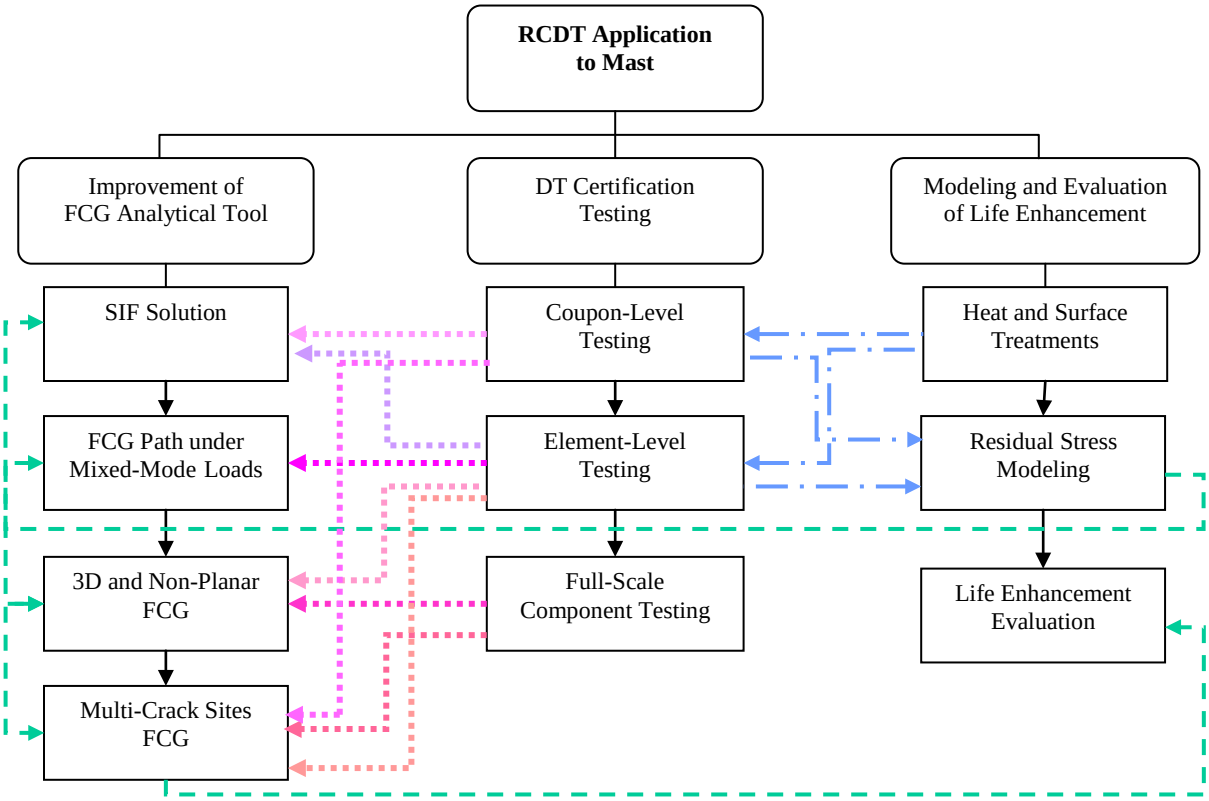

Figure 2. Key Elements of the Technical Approach

2. THE DT CERTIFICATION TEST METHOD FOR ROTOR MAST.

The test program was designed to collect FCG material property data, to provide part-through crack growth data, to verify the FCG analysis, and to implement the CGA capability for the rotor mast. In particular, the objective of Task 3 was to develop a test procedure to support DT qualification and certification testing of a rotor mast.

2.1 BUILDING-BLOCK APPROACH.

The RCDT methodology for the rotor mast included two primary elements: (1) the certification test method and (2) CGA. The effort on certification test method leverages a previously developed building-block test approach to develop and validate the DT methodology for designing, analyzing, and certifying a rotorcraft component. This consisted of first conducting coupon-level testing, then element-level testing and analysis, followed by full-scale testing and analysis. However, due to budget limitations, the full-scale tests were removed from the program.

The load and stress spectra were defined prior to the testing and analysis programs. Such spectra were generated based on the collected usage spectra of four categories and provided fundamental inputs for the loading conditions that are needed to determine the test load level and to perform CGA. Figure 3 shows the four categories of helicopter usage and types of loading on the rotor mast. The combination of bending, torsion, and shear were applied to the element specimen at constant amplitude.

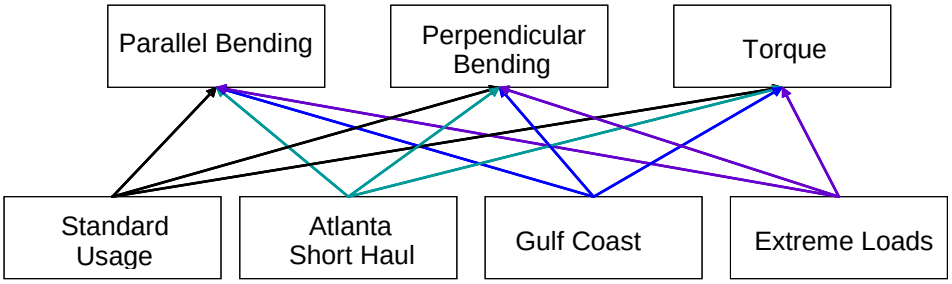

Figure 3. Load Conditions for Rotor Mast DT Testing and Analysis

Two types of coupon-level tests were conducted: middle tension (M(T)) test and surface flaw FCG (Kb-Bar) specimen test. The M(T) tests were performed to characterize the FCG properties of the two representative rotor mast materials, and the Kb-Bar tests were performed to investigate part-through crack growth and the effect of surface treatment on the FCG behavior of rotor mast materials. The test results were also used to evaluate the FCG analysis methods at the level of simple geometry and loading.

The materials representative to the rotor masts and the tests necessary to reflect DT design features of rotor masts are further defined in table 1. These materials are 4340 180- to 200-ksi UTS steel (denoted as 4340 steel) and 9310 180- to 200-ksi UTS steel (denoted as 9310 steel).

Table 1. Materials and Test Methods for the Building-Block Tests

Material	4340 Steel	9310 Steel
Coupon FCG	M(T)	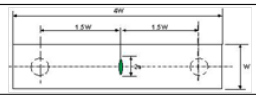
	Kb-Bar	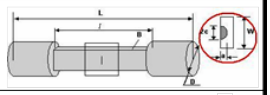
Element FCG	Radius Fillet	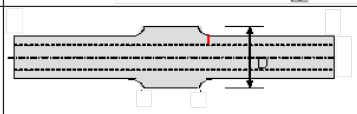
	Spline	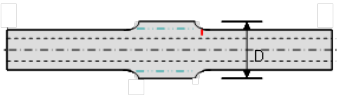
Full-Scale FCG		

2.2 THE M(T) TESTS.

The purpose of the M(T) test was to develop the threshold and Paris regions of the FCG curve under steady-state, cyclic conditions for 4340 steel and 9310 steel. The M(T) test method was chosen because the crack configuration was representative of the through cracks typically observed in drive shafts. The FCG (crack *a*-tip growth rate (*da*/*dN*)) tests were all performed at laboratory temperature, following the specification of ASTM Standard E 647-05. An automated data acquisition system, using the direct current electric potential drop (PD) method, was used for crack measurement. Further details on the M(T) tests are in appendix A.

A schematic of the M(T) coupon specimen is shown in figure 4.

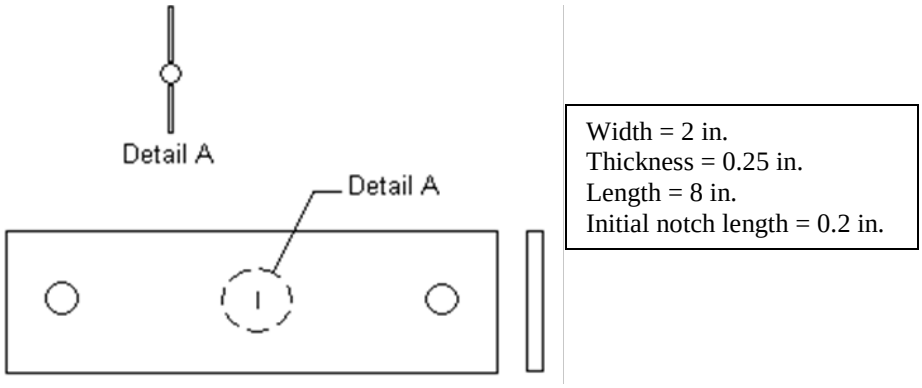

Figure 4. The M(T) Coupon

2.2.1 The M(T) Test Requirements and Test Matrix.

Sixteen M(T) FCG specimens were tested at five stress ratios (R = -1, -0.5, 0.05, 0.5, and 0.8), with several replicates for each stress ratio. These five stress ratios were chosen because they are close to the real loading applications of a rotor mast. Table 2 shows the test matrix for the M(T) tests. The original plan included 22 tests, with three replicates for R = 0.05 (4340 and 9310 each) and two replicates for the other stress ratios. Challenges were encountered for the 9310 steel tests, and 6 of the 11 tests were lost, leaving 5 completed M(T) tests for 9310 steel, as indicated in table 2.

Table 2. The M(T) Coupon Test Matrix

Material	R = -1	R = -0.5	R = 0.05	R = 0.5	R = 0.8
4340 steel	2	2	3	2	2
9310 steel	--	--	1	2	2
Total	16				

2.2.2 The M(T) Test Results.

The *da*/*dN* threshold and Paris regions, obtained via M(T) tests, are shown in figure 5 for 4340 steel and in figure 6 for 9310 steel. Additional details are in appendix A.

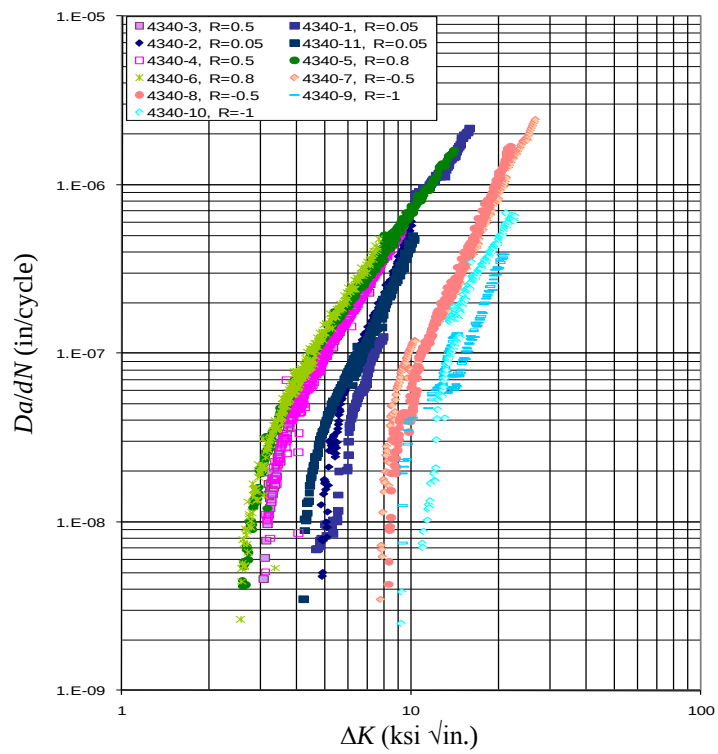

Figure 5. The 4340 Steel M(T) FCG Curves: R = -1, -0.5, 0.05, 0.5, and 0.8

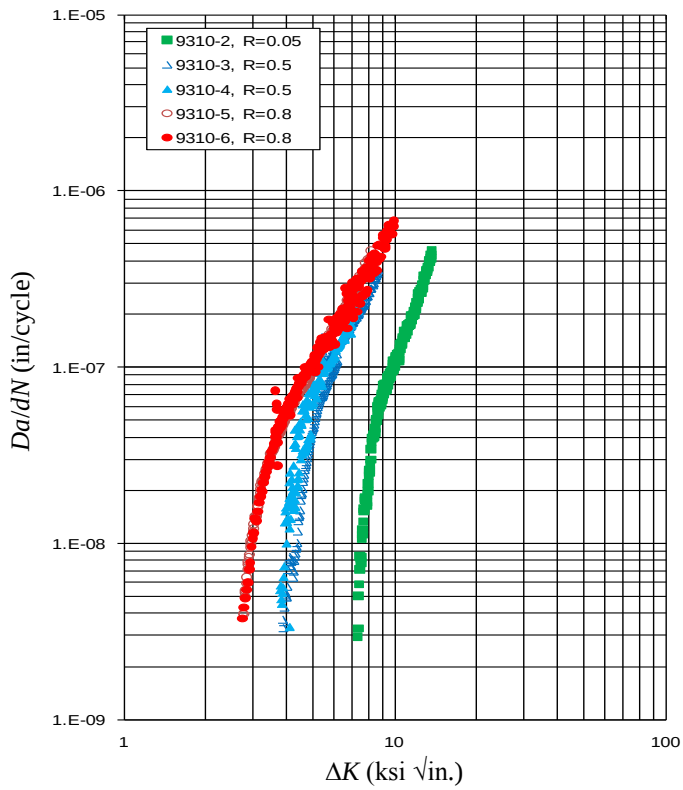

Figure 6. The 9310 Steel M(T) FCG Curves: R = 0.05, 0.5, and 0.8

2.2.3 Discussion of M(T) Test Results.

The M(T) data gathered for this project correlated well with similar data available from third-party sources. In all cases, the data were reviewed for validity, and invalid data points were removed. The primary causes for invalidation of data were uneven growth of the crack tips and crack tips too close to the edge of the specimen.

The M(T) tests for the load applications of negative stress ratios were very challenging for 4340 steel and 9310 steel. That is, introduction of compressive load makes the FCG behavior of 4340 steel and 9310 steel M(T) coupons deviate from the expected results and the *da*/*dN* curves slightly dissimilar from one another. This is shown in figure 5 for R = -1 of 4340 steel. This phenomenon is particularly exhibited with 9310 steel, of which the M(T) tests of negative stress ratio, namely R = -0.5 and -1, were all lost with uneven and unstable crack growth, resulting in incomplete threshold data for 9310 steel (figure 6) versus the original plan.

It is interesting to compare the FCG behavior of an M(T) through-thickness crack of 4340 steel and 9310 steel. For tension-tension fatigue, 4340 steel has a lower threshold ΔK_{th} than 9310 steel does. This difference, however, tends to be insignificant when the load ratio increases. Both materials have a similar crack growth rate in the Paris region for all three shown tension-tension R-ratios, and the entire *da*/*dN* curve tends to be nearly identical when subjected to a large load ratio; e.g., R = 0.8.

2.3 THE Kb-Bar TESTS.

Kb-Bar tests are used for characterizing the FCG of surface cracks. However, the obtained crack *a*-tip growth rate (*da*/*dN*) and crack *c*-tip growth rate (*dc*/*dN*) curves are more useful for FCG quantification as a mini-element of a surface crack, rather than for the material threshold property. This is because the stress-intensity factor (SIF) varies along the crack front at each crack increment, and the data reduction method of the Kb-Bar test does not capture the complete details of the crack front SIF. In this program, the Kb-Bar test was performed as a mini-element test to gain a basic understanding of the surface crack FCG behavior of the rotor mast materials and to validate the FCG analysis method. In this program, Kb-Bar tests were specifically associated with the evaluation of surface treatment effects on surface crack FCG, which is described in section 4. A schematic of the Kb-Bar specimen is shown in figure 7.

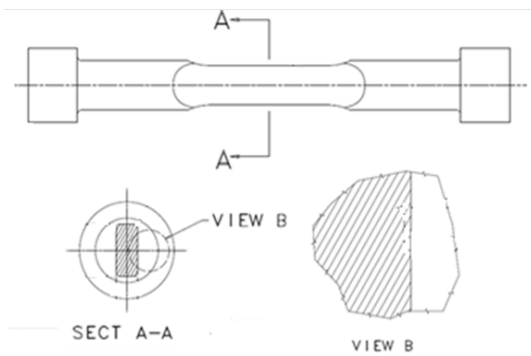

Width = 0.170 in.
Thickness = 0.4 in.
Length = 5 in.
EDM notch = 0.005 in. deep x 0.010 in. long

Figure 7. The Kb-Bar Specimen

2.3.1 The Kb-Bar Test Matrix.

Table 3 shows the test matrix for the Kb-Bar tests. Three stress ratios were applied to the Kb-Bar tests (i.e., R = -1, 0.05, and 0.8) and three surface conditions were applied (i.e., baseline, carburized, and shot-peened). The baseline test was performed as the mini-element test of the building-block method. The shot-peened and carburized tests were performed to investigate the influence of surface treatments on the FCG behavior of a surface crack. The test results for all the surface conditions are reported in this section. Further discussion on the effects of the surface treatment on FCG behavior of a surface crack is presented in section 4.

Note that the tests were primarily performed with the 4340 steel for the conditions of baseline, shot-peened, and carburized surfaces. For the 9310 steel, only stress ratio R = 0.05 tests were performed. It was intended to make the 4340 steel tests complete from coupon level to the upper level and to have the 9310 tests start at a certain level so the FCG behavior of both steels can be compared on a fundamental basis. The details of the test setup, procedures, and data requirements are shown in appendix A.

Table 3. Test Matrix for Kb-Bar Specimens

Surface	Steel	R = -1	R = 0.05	R = 0.8
Baseline	4340	3	5	3
	9310	--	3	--
Carburized	9310	--	2	--
Shot peened	4340	2	5	3
	9310	--	3	--
4340 steel total		21		
9310 steel total		8		
Total		29		

2.3.2 The Kb-Bar Test Results.

2.3.2.1 The 4340 Steel Test Conditions and Results for Baseline Tests.

The results for the 4340 steel baseline Kb-Bar tests are listed in table 4. The obtained Kb-Bar *da*/*dN* curves for the 4340 steel are shown in figure 8.

Table 4. Test Conditions and Results for 4340 Steel Baseline Kb-Bar Tests

Specimen Number	Load Ratio (R) Min/Max	K-Gradient Threshold (1/in.)	Max Load Paris (lbf)	ΔK Threshold (ksi√in.)
101-2	0.05	-30.0	2278	3.91
101-3	0.05	-30.0	2404	3.55
101-11	0.05	-30.0	2173	3.94
101-12	0.05	-20.0	1786	4.05
101-7	0.05	N/A	5973	N/A
101-4	0.80	-30.0	4680	2.54
101-5	0.80	-30.0	5934	2.51
101-6	0.80	-30.0	5857	2.59
101-8	-1.00	-30.0	2329	5.99
101-9	-1.00	-30.0	2436	7.61
101-10	-1.00	-30.0	2687	8.34

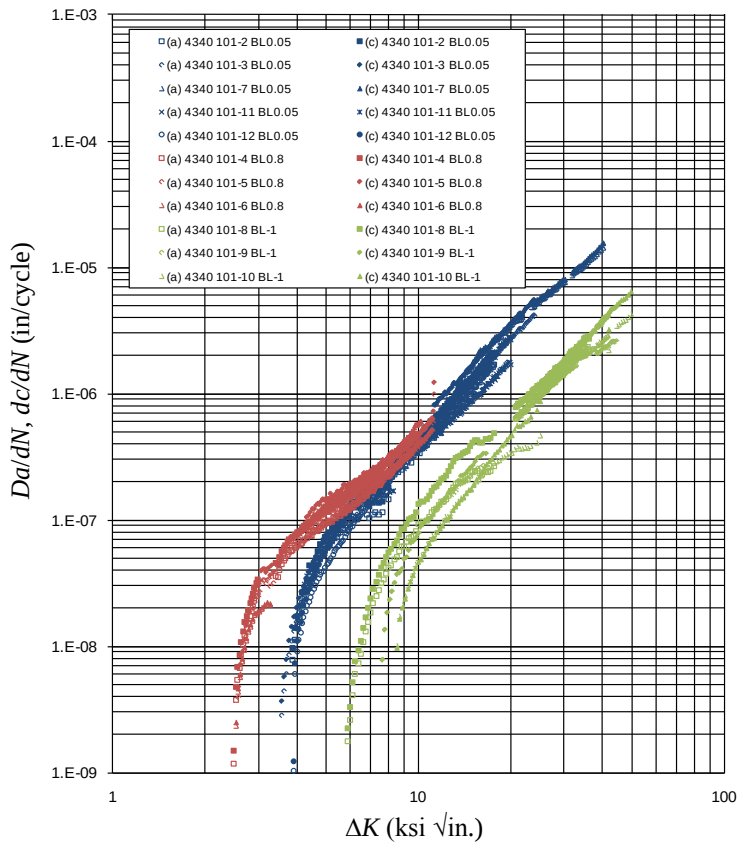

Figure 8. The 4340 Steel Kb-Bar Baseline Test Results: R = -1, 0.05, and 0.8

2.3.2.2 The 4340 Steel Test Conditions and Results for Shot-Peened Tests.

The results for the 4340 steel shot-peened Kb-Bar tests are listed in table 5. The *da*/*dN* curves for the 4340 steel shot-peened specimens are shown in figure 9.

Table 5. Test Results for 4340 Steel Shot-Peened Kb-Bar Tests

Specimen Number	Load Ratio (R) Min/Max	K-Gradient Threshold (1/in.)	Max Load Paris (lbf)	ΔK Threshold (ksi√in.)
105-1*	0.05	N/A	5966	N/A
105-2	0.05	-30.0	2580	3.41
105-3	0.05	-30.0	2782	3.11
105-4	0.80	-30.0	5700	2.44
105-5	0.80	-30.0	5827	2.35
105-6	0.80	-30.0	5748	2.77
105-7	0.05	N/A	5968	N/A
105-8	-1.00	-30.0	2178	6.93

* Specimen failed during precrack operation because operator could not see surface crack. Subsequent specimens were precracked under K-control automation.

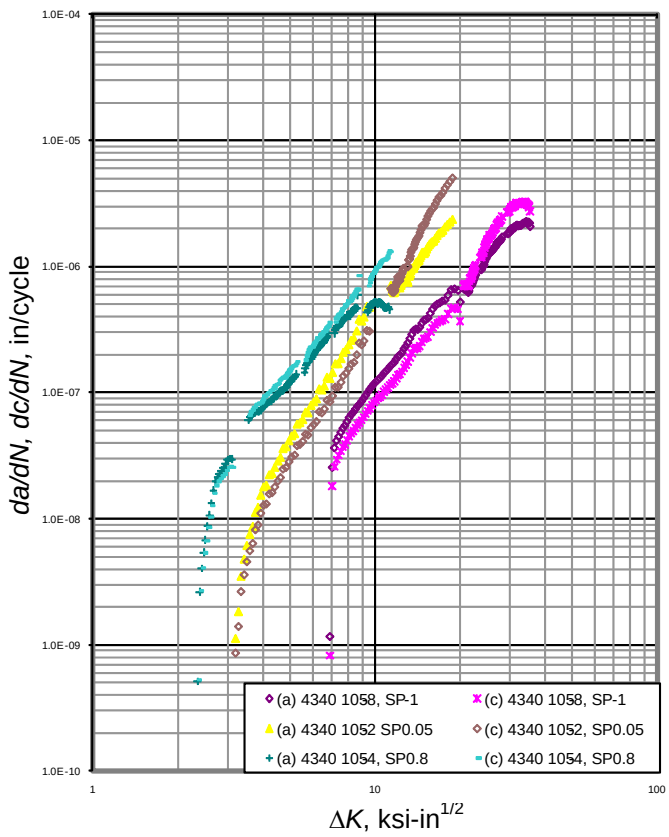

Figure 9. The 4340 Steel Shot-Peened Kb-Bar FCG Curves: R = -1, 0.05, and 0.8

2.3.2.3 The 9310 Steel Test Conditions and Results for Baseline Tests.

The results for the 9310 steel baseline Kb-Bar tests are listed in table 6. The obtained Kb-Bar *da*/*dN* curves for the 9310 steel baseline specimens are shown in figure 10.

Table 6. The 9310 Steel Baseline Kb-Bar Test Results

Specimen Number	Load Ratio (R) Min/Max	K-Gradient Threshold (1/in.)	Max Load Paris (lbf)	ΔK Threshold (ksi√in.)
111-1	0.05	-30.0	2486	4.11
111-2	0.05	-30.0	2165	3.97
111-3	0.05	---	5946	N/A

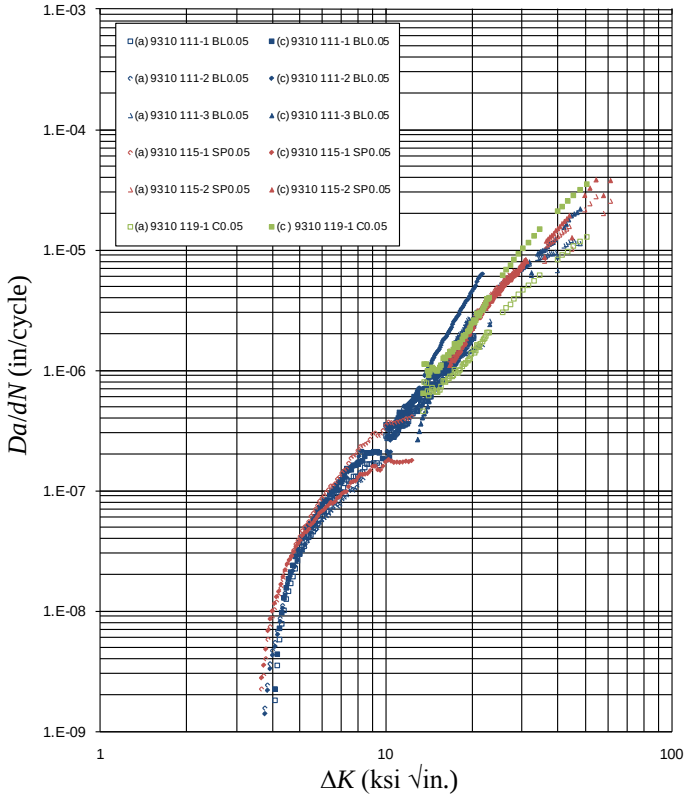

(a) = *da*/*dN* curve BL = Baseline C = Carburized
(c) = *dc*/*dN* curve SP = Shot-peened

Figure 10. The 9310 Steel Baseline, Shot-Peened, and Carburized Kb-Bar FCG Curves: R = 0.05

2.3.2.4 The 9310 Steel Test Conditions and Results for Carburized Tests.

The results for the 9310 steel carburized Kb-Bar tests are listed in table 7. The obtained Kb-Bar *da*/*dN* curves for the 9310 steel carburized specimens are shown in figure 10.

Table 7. Test Results of 9310 Steel Carburized Kb-Bar Tests

Specimen Number	Load Ratio (R) Min/Max	K-Gradient Threshold (1/in.)	Max Load Paris (lbf)	ΔK Threshold (ksi√in.)
119-1	0.05	N/A	6007	N/A
119-2	0.05	-15.0	2950	N/A

2.3.2.5 The 9310 Steel Test Conditions and Results for Shot-Peened Tests.

The results for the 9310 shot-peened Kb-Bar tests are listed in table 8. The obtained Kb-Bar *da*/*dN* curves for the 9310 steel shot-peened specimens are shown in figure 10.

Table 8. The 9310 Steel Shot-Peened Kb-Bar Test Results

Specimen Number	Load Ratio (*R*) Min/Max	K-Gradient Threshold (1/in.)	Max Load Paris (lbf)	Δ*K* Threshold (ksi√in.)
115-1	0.05	-30.0	2204	3.74
115-2	0.05	N/A	7882	N/A
111-4	0.05	-20.0	1420	2.05

For comparison, the *da*/*dN* curves for the 9310 steel specimens under baseline, carburized, and shot-peened surface conditions are plotted in figure 10. The blue curves show the baseline tests, the red curves show the shot-peened, and the green curves show the carburized. All the tests were performed under stress ratio $R = 0.05$ (tension-tension).

2.3.3 Comparison of 4340 Steel and 9310 Steel Kb-Bar Test Results.

Figure 11 shows a comparison of the FCG *da*/*dN* behavior between 4340 steel and 9310 steel. Since the Kb-Bar tests for 9310 steel were all performed at $R = 0.05$, the comparison is shown for the $R = 0.05$ data. This raw data does not show a distinguishing difference of the *da*/*dN* behavior between the two materials.

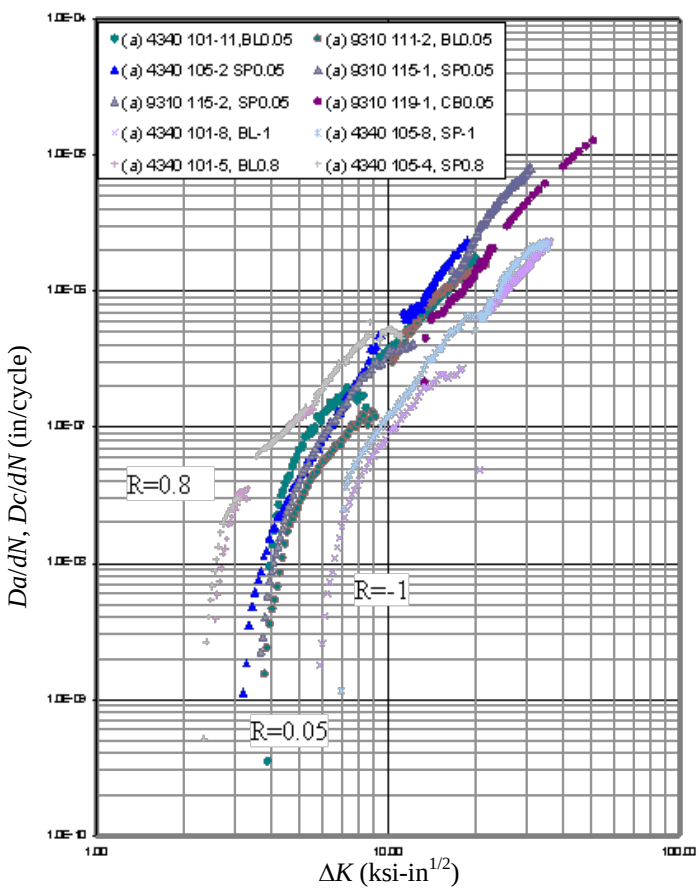

Figure 11. Comparison of 4340 Steel and 9310 Steel Kb-Bar *da*/*dN*

2.3.4 Comparison of Kb-Bar and M(T) Test Results.

Figure 12 shows a comparison of the FCG behavior with the 4340 steel baseline Kb-Bar test specimens and with the 4340 steel M(T) coupons. The bright-colored curves are the M(T) tests, while the light-colored curves are the Kb-Bar tests. Green represents R = -1, blue represents R = 0.05, and purple represents R = 0.8. The thresholds are very similar for both the 4340 steel Kb-Bar and M(T) tests at R = 0.8, and the threshold of the Kb-Bar tests tend to be greater than the M(T) tests with decreasing stress ratio R. For the larger stress ratio R = 0.8, both the Kb-Bar and M(T) tests have quite a large segment in the Paris region at which the crack growth rates are also very similar. This identical segment tends to be shorter with decreasing stress ratio R, and the M(T) crack coincided with the faster growth segment quicker than the Kb-Bar crack.

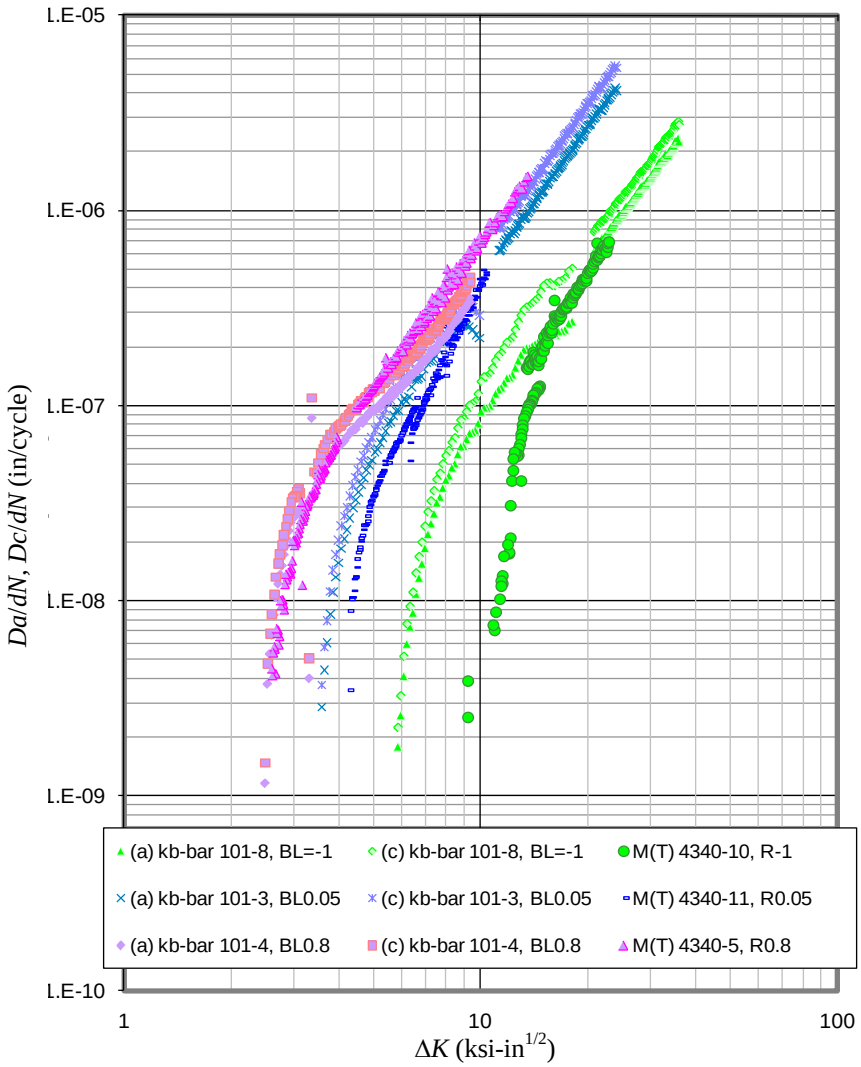

Figure 12. Comparison Between Kb-Bar and M(T) *da/dN* Curves of Baseline 4340 Steel Coupons

The FCG behavior for 9310 steel are different between the Kb-Bar and M(T) tests, as shown in figure 13. The Kb-Bar data of the baseline, shot-peened, and carburized surface conditions were compared to the M(T) data under baseline conditions at R = 0.05. A crossover occurs when the M(T) crack has a higher FCG threshold, a much shorter Paris region, and an earlier fast growth region.

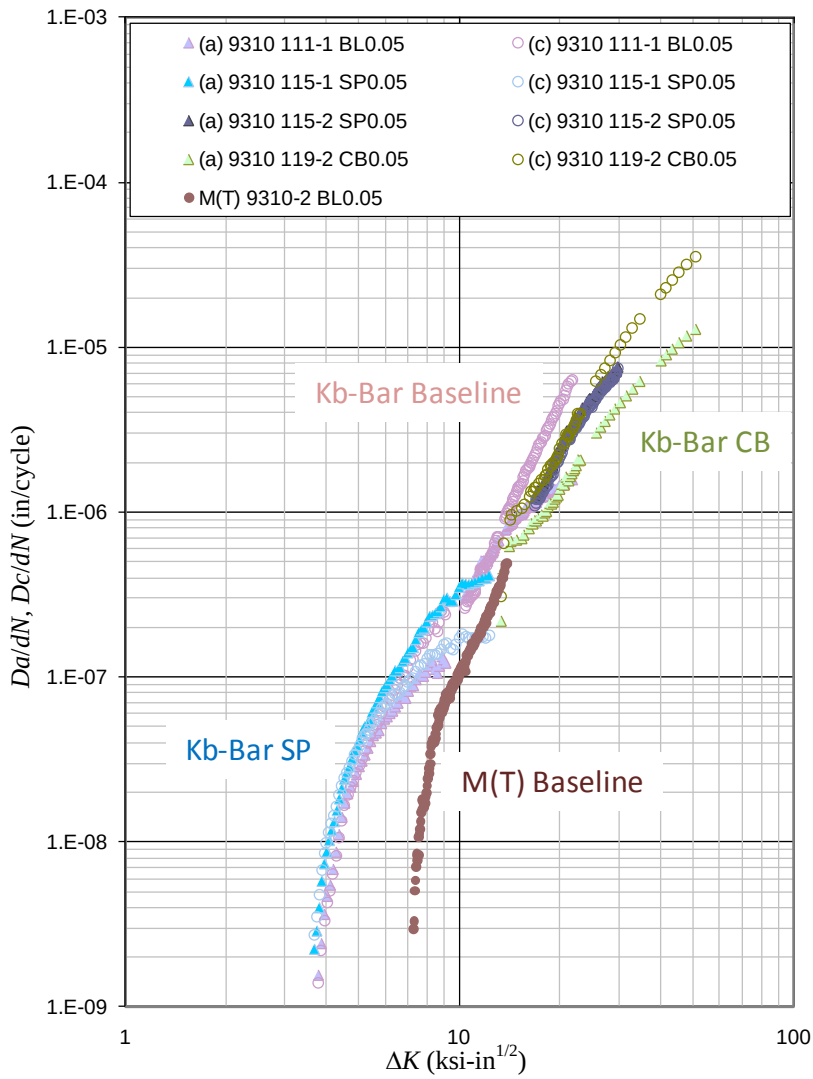

Figure 13. Comparison of Kb-Bar and M(T) *da*/*dN* Data (9310 Steel, R = 0.05)

2.4 ELEMENT TEST PROGRAM.

The next level of testing in the building-block method involved an element specimen containing representative geometric features that were subject to load inputs representative of real-time load applications, although simplifications were made to facilitate ease of testing.

The purpose of the element tests was to quantify the FCG behavior of the DT critical design feature and verify the DT capability of such a design feature. The test data obtained from the M(T) and Kb-Bar tests referred to the magnitude of the load applications and the design of the

test fixture. Finite element analysis (FEA) was performed to determine the design parameters and to verify the location and position of the notch for crack initiation and growth. The achieved element testing results provide a basis for the design of the next level full-scale testing.

Figure 14 shows a fillet radius element test specimen. The elements were fabricated using 4340 steel. 9310 steel was not used in order to stay within budget. The element design included a surface crack at a typical design feature and a fillet radius, which is representative of a typical rotor mast design. Flats were machined in the grip region for specimen positioning and mounting to the testing frame. Splines were cut into the specimen for the purpose of load introduction.

Figure 14. Fillet Radius Element Test Specimen

2.4.1 Test Matrix and Loads.

The element tests were performed with combinations of bending, torsion, and shear loads: bending moment equal to torsional moment; and bending moment twice the torsional moment. The shear and bending moment remained unchanged for the two loading combinations. For each loading combination, the specimens were divided into groups of peened and unpeened. Table 9 shows the test matrix, in which there were two replicates for each case.

Table 9. Fillet Element Test Matrix

Condition	Load	
	Bending = Torsion	Bending = 2 x Torsion
Baseline	2	2
Shot-peened	2	2
Total	8	

Determination of the loads and notch orientation was supported by FEA, as shown in figures 15 and 16. The two sets of loads were applied to the finite element (FE) model in two bending moment-to-torsion ratios (1:1 and 2:1) so the resulting principal stress at the fillet root was a prescribed value (55 or 80 ksi). The design was verified so the maximum principal stress occurred at the tangential point of the fillet radius area, as desired (figure 15). The normal to the direction of the first principal stress at the fillet root was calculated and used to determine the proper orientation of the notch, as shown in figure 16. In figure 16, α is the angle of the normal orientation versus longitudinal axis, and β is the angle of the notch plane versus normal cross section of the shaft. The calculated angles are listed in table 10 along with the simplifications used in the test.

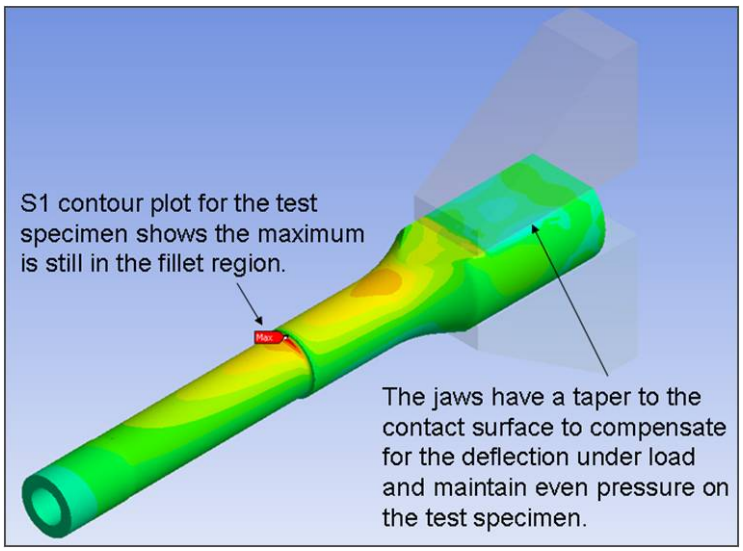

Figure 15. The FE Model of the Fillet Radius Element Specimen

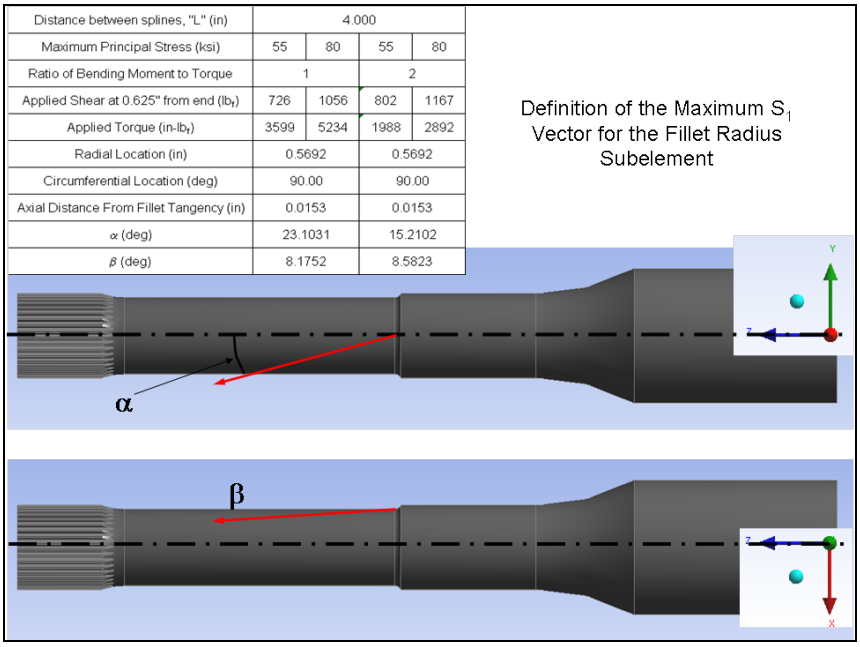

Figure 16. Calculated Crack Plane Normals (for Notch Orientation)

Table 10. Crack Plane Normal Angles (for Notch Orientation)

	α		β	
	Calculated	Applied	Calculated	Applied
M = T	23.1°	30°	8.2°	0°
M = 2T	15.2°	15°	8.6°	0°

2.4.2 Element Testing Fixture Design.

The test setup is shown in figure 17. A point load was introduced by a tension bar that was connected to the load actuator at one end and to a link arm at the other end. The link arm was designed in such a way that the tension bar could be connected to the end or to the middle position. The link arm was perpendicularly connected to the test specimen through a spline so that the point load conveyed by the tension bar could be transformed into bending and torsion to the test specimen. The length of the link arm was designed to generate torsion and bending of the same magnitude (M = T) or bending of twice the torsion magnitude (M = 2T), depending on the joint position of the tension bar to the end or to the middle of the link arm.

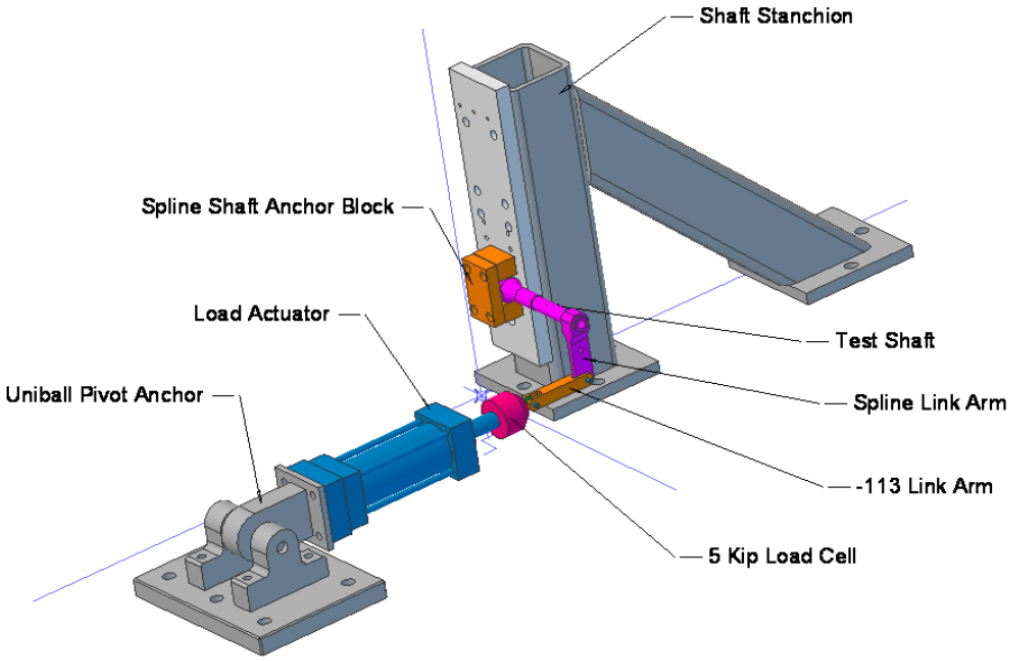

Figure 17. Fillet Element Test Setup

In each test, the specimen was cycled at a specified precrack load to develop a starting crack from the electrical discharge machining (EDM) notch; the crack then grew to failure at a defined fatigue load. During the fatigue portion of the test, a series of high-frequency, high-stress ratio cyclic blocks were applied to the specimen to change the crack front texture. This was done to enhance posttest analysis and allow comparison of the observed chordal crack length with the actual chordal crack length. Using this "buzz cycle" method, the crack front appears as bright striations on the crack plane. After the final buzz cycle application, the fatigue loads were applied to the failure of the specimen.

2.4.3 Element Test Results.

Table 11 shows the results for four baseline fillet element specimens, and table 12 shows the results for four shot-peened fillet element specimens.

Table 11. Baseline Fillet Element Specimen Test Summary

Specimen Number	M:T	Notch Angle	Load Level	Maximum Load (lb)	Minimum Load (lb)	Cycles to Failure
S5	1	30°	Precrack	688	34	87,790
			Precrack	764	38	99,329
			Fatigue	764	38	303,070
S6	1	30°	Precrack	764	38	100,290
			Fatigue	764	38	278,669
S7	2	15°	Precrack	760	38	180,048
			Precrack	844	42	80,005
			Fatigue	844	42	326,093
S8	2	15°	Precrack	844	42	100,023
			Fatigue	844	42	292,395

Table 12. Shot-Peened Fillet Element Specimen Test Summary

Specimen Number	M:T	Notch Angle	Load Level	Maximum Load (lb)	Minimum Load (lb)	Cycles to Failure
P1	1	30°	Precrack	1105	55	70,116
			Fatigue	1228	61	94,555
P2	1	30°	Precrack	1000	50	200,021
			Fatigue	764	38	408,058
P3	2	15°	Precrack	1105	55	120,029
			Fatigue	844	42	297,263
P4	2	15°	Precrack	760	38	470,161
			Fatigue	844	42	224,199

Figures 18 and 19 show crack length versus fatigue cycles for the depth (a) and surface (2c) crack dimensions, respectively, for the M = T loading case. Figures 20 and 21 show crack length versus fatigue cycles for the M = 2T load case. In all plots, the cycle counts have been shifted to allow for direct comparison between specimens by aligning initial crack lengths. Crack growth shapes are shown as crack shape aspect ratios *a/c* for the baseline fillet radius FCG elements in figure 22 and for the shot-peened fillet radius FCG elements in figure 23.

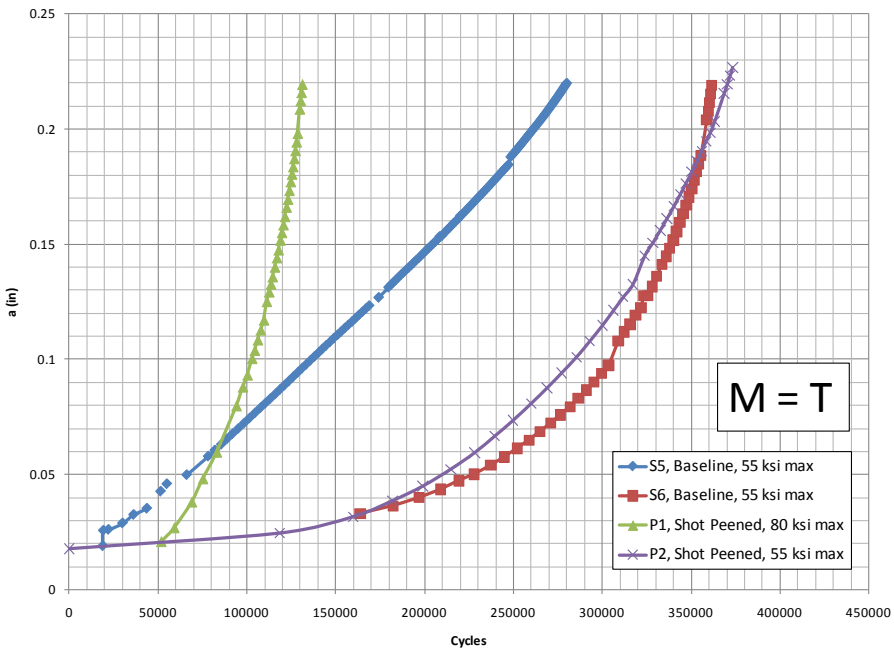

Figure 18. Crack Depth (a) vs Cycles for M = T Loading Case

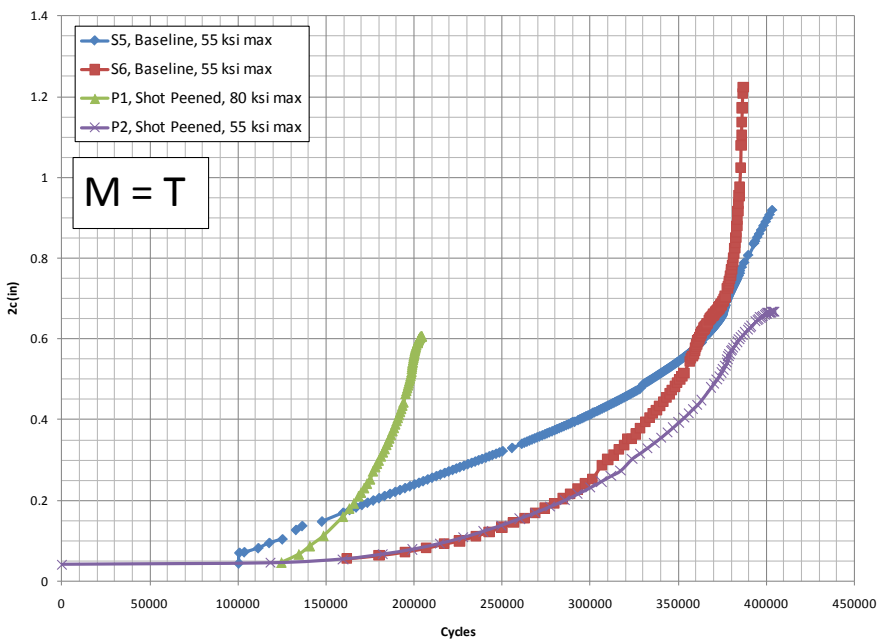

Figure 19. Crack Chordal Length (2c) vs Cycles for M = T Loading Case

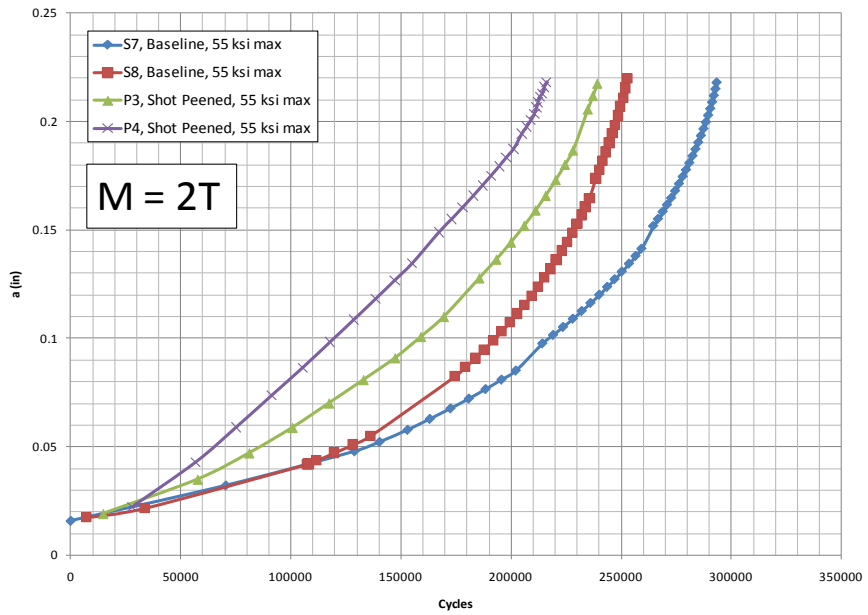

Figure 20. Crack Depth (a) vs Cycles for M = 2T Loading Case

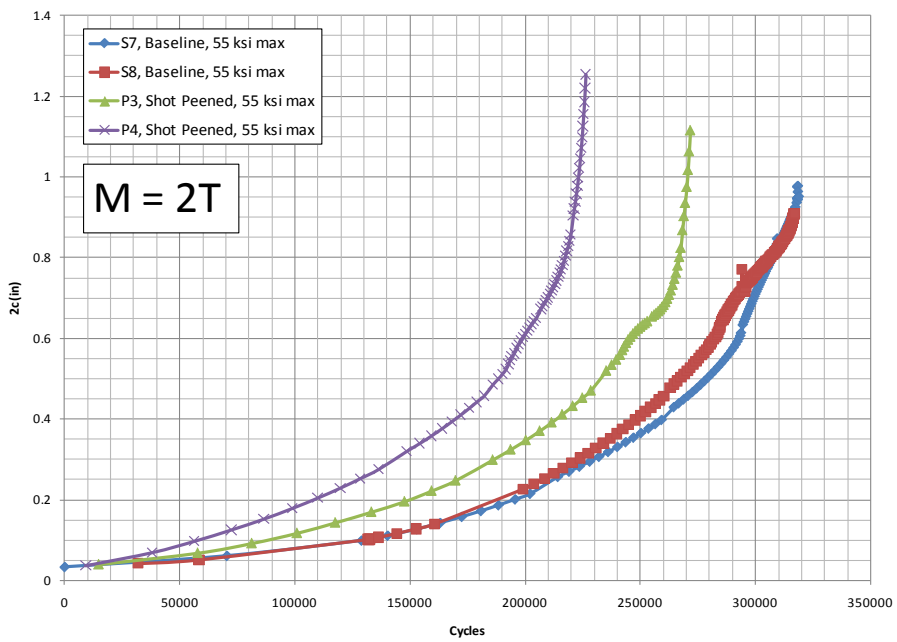

Figure 21. Crack Chordal Length (2c) vs Cycles for M = 2T Loading Case

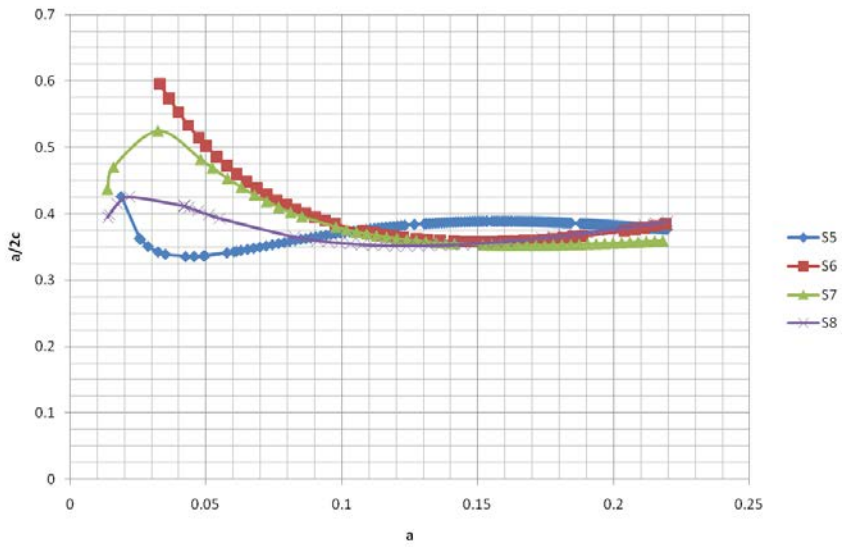

Figure 22. Crack Shape Aspect Ratio of Baseline Fillet Radius Element FCG

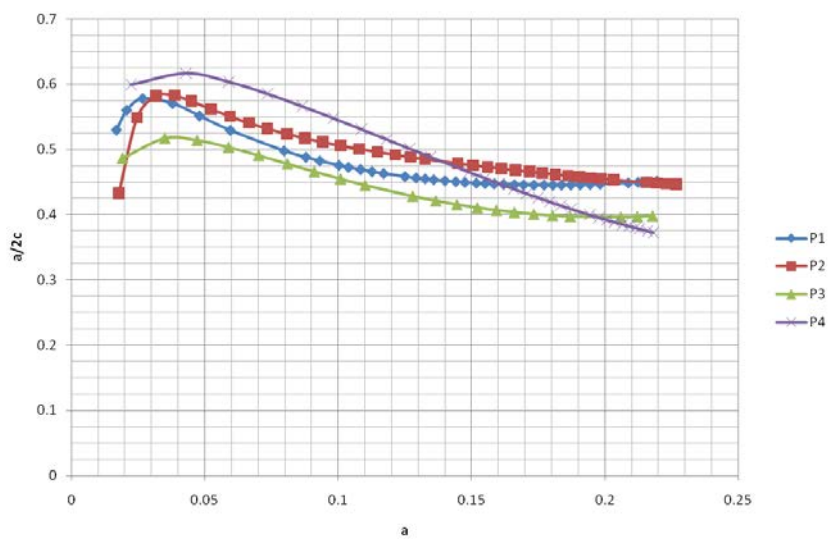

Figure 23. Crack Shape Aspect Ratio of Shot-Peened Element Specimen FCG

2.4.4 Discussion of Element Test Results.

The data shown in figures 19 through 22 should be observed with two significant caveats. First, the surface dimension of the crack (2c) is a chordal length encompassing both crack tips. Due to the asymmetry of the specimen geometry in the vicinity of the notch, one crack tip grows faster than the other. A better comparison would be to show the growth of each crack tip individually. The second caveat is also related to the specimen geometry: the crack plane may not remain planar as the crack grows through the thickness. This may have a considerable impact on crack growth behavior, which is not accounted for in this discussion.

The first observation evident from figures 18 and 19 is that the crack in specimen P1 grew significantly faster than the cracks in the other specimens loaded with the same bending moment-to-torsion ratio. This is clearly due to the difference in load magnitude, resulting in a local stress of approximately 80 ksi for specimen P1, compared to 55 ksi for all other specimens.

Specimen S5 produced unusual data, which may be attributable to poor PD calibration. However, the results for the baseline specimen S6 and shot-peened specimen P2 appear reasonable, and may be compared directly for the M = T loading case. These two specimens were run at the same fatigue load level, and both had a notch of 30° with respect to the cross section plane.

Figures 20 and 21 show crack depth and length versus cycles for the M = 2T (i.e., twice the bending moment relative to torsion) loading case. Specimens S7 and S8 are the baseline specimens, and specimens P3 and P4 are the shot-peened specimens. All four specimens have a notch centered at the tangent of the fillet radius, oriented at a 15° angle with respect to the cross section plane. Here, two replicates of each surface condition may be compared under identical loading conditions.

In summary, the building-block certification test method was demonstrated up to the element test at constant amplitude. The FCG properties obtained from the M(T) tests and the surface crack behavior observed from the Kb-Bar tests provided the basis and guidelines to determine the notch and loads for the element tests. The element FCG tests provide information on the relationship of crack onset and growth with the applied load to certain fillet geometries, which supports full-scale test designs to determine the fatigue life of a rotor mast in terms of FCG.

3. EVALUATION OF CGA CAPABILITY OF CURRENT ANALYSIS TOOLS (TASK 4).

The objective of this effort was to evaluate the current CGA capability of several analysis platforms to apply FCG analysis to a rotorcraft drive system, as demonstrated by the rotor mast.

There are certain challenges when applying CGA to a rotor mast, as listed in table 13. This effort focused on the evaluation of several commonly used FEA and CGA tools and their capability to handle analysis of complex geometry, mixed load, nonplanar cracks, and residual stress effects. The technical approach is outlined below:

- Data obtained from the test program were implemented into the CGA analysis for the rotor mast as input for the variables and analyses validations.
- Closed-form calculations and FEA were performed to correlate SIF solutions that were used for FCG analysis of the rotor mast.
- Existing analytical CGA tools NASGRO® Fracture Mechanics and Fatigue Crack Growth Analysis Software and the FEA platform ANSYS® were specifically examined for their capability to handle DT design features of a rotor mast.

An illustration of the approach is shown in figure 24.

Table 13. Challenges of Applying DT Method to a Rotor Mast

Features of Drive System Components (to be reflected in analysis)	Challenges
Material	Lack of or incomplete reference data
Surface treatment	Existence of residual stress due to surface treatments
Spectrum load	Complex loading due to its unique function of a rotor mast
Complex loads	Nonplanar crack due to complex geometries and stresses
Complex geometry	3D stress state, complex stress distribution through the part

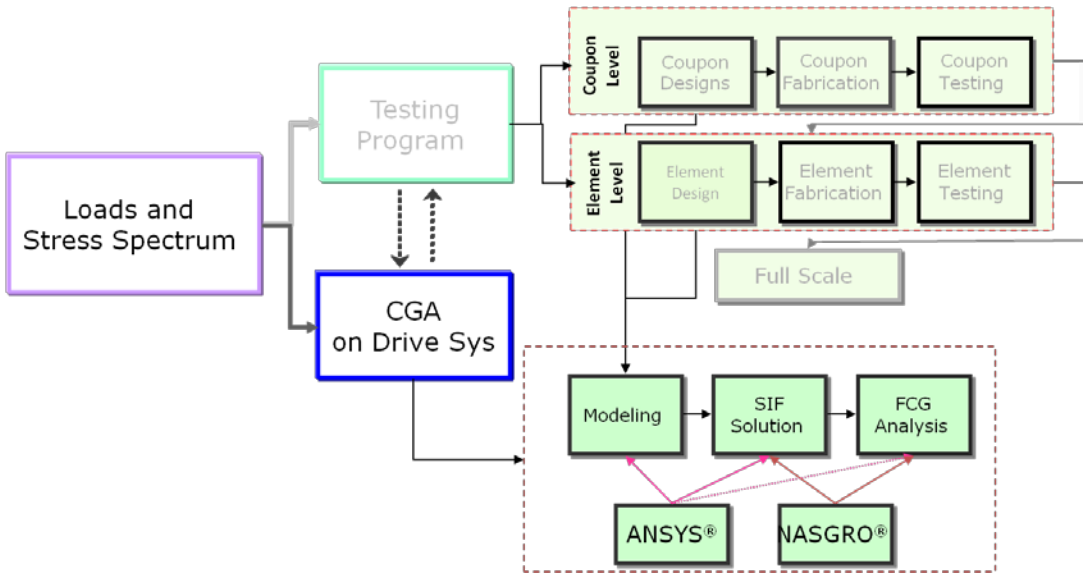

Figure 24. Evaluation of the Capability of CGA Analysis Tools

The crack growth data obtained from the coupon-level and element-level tests were implemented in the evaluation of the crack growth analytical tool capabilities. Full-scale tests were planned for complete implementation, but were later removed from the program due to a budget cut. In addition, Kb-Bar tests were used to evaluate the analytical capability of the tools on the life enhancement effect of shot-peening and carburizing surface treatments.

3.1 EVALUATION OF CURRENT NASGRO CGA CAPABILITY.

A two-phase approach was used for the evaluation. The Phase I analysis was at the coupon level with Kb-Bar geometry, and the Phase II analysis was at the element level with typical geometrical features and representative loading applications of the rotor mast. The 4340 steel was assumed for both phases. Kb-Bar geometry was chosen for the coupon-level evaluation because its semielliptic surface crack is representative of the crack geometries observed in rotor masts. The simple tension application made Kb-Bar an ideal test configuration for characterizing surface crack growth of the material. The Kb-Bar simulation, with known SIF solutions, was

able to validate the model by comparing it with existing test data. The crack growth properties of 4340 steel and SIF solutions are available in the NASGRO library, to which the prescribed Kb-Bar analysis can be compared. The method can then be applied with confidence to the more complex element specimen. The element configuration used for the NASGRO analysis was a simplified rotor mast element. It contained a fillet radius, which is specifically sensitive to crack initiation and growth.

Having the FCG data obtained from the building-block test program (section 2.3) and the measured residual stress profile (section 4.2), the NASGRO CGA capability was also evaluated with incorporated residual stress to the Kb-Bar configuration.

The NASGRO CGA capability was evaluated with "blind" analyses. The input variables and parameter for modeling and analysis were determined by Bell Helicopter (BH) based on test design and/or test results. The outputs of the NASGRO FCG analysis were then compared to the test results at BH. The analysis matrix is shown in table 14.

Table 14. The FCG Analysis Matrix Using NASGRO

Analysis		NASGRO
Kb-Bar	SIF	(Available in NASGRO Library)
	FCG	Performed using given load, library SIF, and given material *da*/*dN*
Residual Stress Kb-Bar	SIF	Performed using given load and residual stress profile
	FCG	Performed using calculated SIF and given material *da*/*dN*
Fillet Radius	SIF	Performed using given geometry and loads
	FCG	Performed using calculated SIF and given material *da*/*dN*

3.1.1 Kb-Bar FCG Simulation Using NASGRO.

The Kb-Bar geometry is a simple rectangular cross section with a semielliptical part-through surface crack. This geometry is already included in NASGRO as model SC17 (figure 25). Kb-Bar geometry was chosen for the evaluation of NASGRO CGA's capability at the coupon level for rotor mast FCG because the semielliptic surface crack of Kb-Bar is representative of the surface cracks and part-through cracks that have been observed in rotor masts. With the simple planar crack and tension-tension (or tension-compression) loading, the Kb-Bar simulation checked the validity of the FCG model and analysis of NASGRO. The analyses were performed using the following five cases:

- Case 1—FCG simulation during load shedding without residual stress under designed load
- Case 2—FCG simulation during load shedding with residual stress under designed load
- Case 3—FCG simulation during load shedding without residual stress under given load history

- Case 4—FCG simulation of actual Kb-Bar test
- Case 5—FCG simulation of actual shot-peened Kb-Bar test

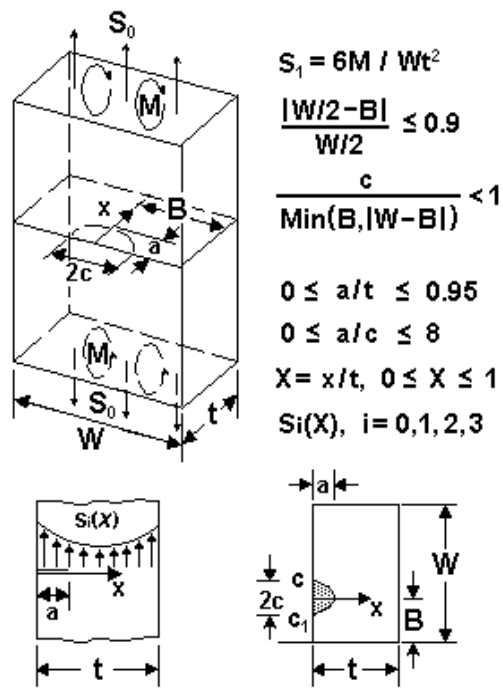

Figure 25. The NASGRO SC17 Model for SIF Solution

3.1.1.1 Kb-Bar FCG Simulation Under Designed Load (Cases 1 and 2 With and Without Residual Stress).

The analysis was performed with and without a specified residual stress field at three different stress ratios (R = 0.8, 0.05, and -1) and at a normalized K-gradient, C = -30/in. $(1/K)(dK/da)$, and then repeated using the NASGRO noninteraction crack growth model. The NASGRO strip-yield model was modified to facilitate the simulation of crack closure behavior and to compute crack growth rates during load reduction tests for a surface crack geometry following the general ASTM E 647 load reduction procedure.

The Kb-Bar cross section dimensions were width = 0.400 in. and thickness = 0.168 in. The initial EDM notch was 0.010 in. (width) and 0.005 in. (depth). A precrack was grown under constant-amplitude loading until $2c$ = 0.020 in., where c is the center-to-tip distance of the crack measured on the surface. The load shedding began at this crack size and continued until the threshold was reached. But, after the crack had stopped growing, the load amplitude was increased and cycling was continued under constant-amplitude loading. The specific values of the loads for each stress ratio are specified in table 15. For the cases involving residual stress, the specific residual stress gradient applied is given in table 16.

Table 15. Loads for Kb-Bar Simulation (Cases 1 and 2)

R	P_{max} for Precracking	P_{max} After end of Load Shed
0.05	4300 lb (63.99 ksi)	1400 lb (20.83 ksi)
0.8	5000 lb (74.67 ksi)	2150 lb (31.99 ksi)
-1.0	4500 lb (66.96 ksi)	1400 lb (20.83 ksi)

P_{max} = Maximum load

Table 16. Residual Stress Gradient for Kb-Bar FCG Simulation

Depth (in.)	Residual Stress (ksi)
0	-96
0.002	-110
0.004	-104
0.006	-75
0.008	-35
0.01	0
0.012	10
0.016	12
0.02	12
0.03	12
0.04	12

The NASGRO Material Library data for the 4340 steel was used. The NASGRO SC17 surface crack model (see figure 26) was used to perform the simulations. The SC17 model is an invariant weight function model that includes a very wide range of crack shape aspect ratios ($0 < a/c < 8$).

The calculations were based on NASGRO Version 6.0. The NASGRO program was modified to perform a load-shedding test following the ASTM procedure. The load-shedding logic was implemented at the deepest tip of the SC17 solution, the *a*-tip. All the changes in load history were based on the behavior at the *a*-tip.

3.1.1.2 Kb-Bar FCG Simulation Under Designed Load (Case 3).

The requirements for Case 3 of the NASGRO Kb-Bar FCG analysis of a load-shedding experiment were the same as for Cases 1 and 2, except the loading history. In this case, a load-shedding history was used as a function of fatigue cycles, as shown in table 17. This loading history was taken from the actual Kb-Bar test program. The stress ratio during the load shedding was kept constant at $R = 0.05$. The crack size at the beginning of the load shedding was given as

a_0 = 0.0117 in. and c_0 = 0.0105 in., which was also an initial crack in the actual test. No residual stresses were included.

Table 17. Specified Load Shedding History for Kb-Bar Analysis

Elapsed Cycles (N)	P_{max} (lb)	P_{min} (lb)
0	4625	231
2,370	4351	218
5,526	4183	209
8,778	3978	199
12,466	3805	190
16,308	3638	182
20,070	3519	176
24,649	3333	167
28,577	3206	160
32,268	3080	154
36,941	2986	149
42,013	2857	143
47,563	2753	138
52,844	2650	133
58,908	2561	128
65,762	2463	123
72,514	2372	119
79,511	2292	115
86,987	2215	111
94,173	2146	107
102,495	2075	104

Elapsed Cycles (N)	P_{max} (lb)	P_{min} (lb)
112,676	1992	100
122,190	1932	97
131,717	1865	93
140,862	1815	91
150,763	1760	88
164,850	1695	85
177,987	1637	82
191,297	1595	80
207,999	1542	77
226,616	1497	75
246,537	1450	73
266,886	1403	70
290,150	1368	68
319,839	1321	66
351,875	1287	64
392,630	1247	62
452,732	1205	60
511,476	1173	59
599,611	1141	57
6,685,562	1114	56

P_{max}= Maximum load
P_{max}= Minimum load

After the load shedding was completed, constant-amplitude loading was resumed with P_{max} = 2278 lb (maximum stress of 33.9 ksi) and R = 0.05. The full stress history is shown in figure 27.

This analysis was conducted with the NASGRO strip-yield model since the load history was specified directly rather than being expressed in terms of an imposed SIF gradient. The specified load shedding was input to NASGRO in the form of a long block spectrum file. The given load and cycle values were interpolated to fill in eight additional values between each pair of points to make the load reduction a smooth and nearly continuous process.

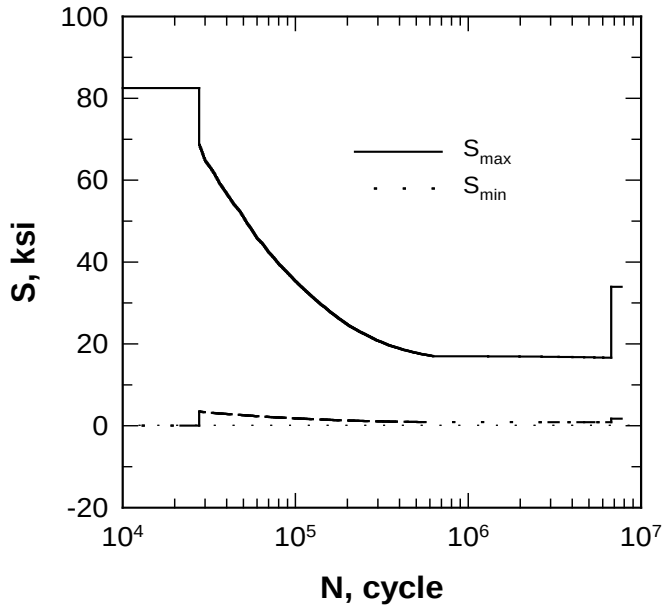

Figure 26. Stress History Applied in Load-Shedding Simulation (Case 3)

Since the stress history during the precracking was not known, the simulation used constant-amplitude loading with a maximum stress of 82.5 ksi. To obtain the specified crack size and shape at the beginning of the load shedding (a_0 = 0.0117 in. and c_0 = 0.0105 in.), it was very challenging to start with notch dimensions a_n = 0.005 in. and c_n = 0.005 in. because the crack shape aspect ratio for the stable analysis of a surface fatigue crack grown in uniform tension requires approximately a/c = 1.0, but the crack shape aspect ratio specified herein was a_0/c_0 = 1.114 in. Therefore, the initial crack size and shape and the number of precrack cycles were selected iteratively to give the proper conditions at the beginning of the load shedding. This difference should not be significant for the analysis of the load shedding; the key issue is simply for the crack at the beginning of the load shedding to have a stable plastic wake.

The NASGRO material properties for 4340 steel were used for Case 3. The NASGRO SC17 crack model was used as well.

3.1.1.3 An FCG Simulation of Actual Baseline and Shot-Peened Kb-Bar Tests (Cases 4 and 5).

In Cases 4 and 5, simulations of FCG in Kb-Bar specimens were performed to further evaluate the NASGRO CGA capability by using the actual Kb-Bar test parameters (i.e., test coupon dimensions, initial crack size, and loading history). The machining and shot-peening residual stresses were incorporated for each case, respectively: Case 4 for the baseline specimen with machining residual stress, and Case 5 for the shot-peened specimen with cold-worked residual stress. The variables of the coupon dimensions and crack shape were directly measured from the test specimens. Table 18 lists the geometric dimensions and the loading case designation for the two simulations.

Table 18. Initial Crack Sizes of Kb-Bar FCG Simulation (Cases 4 and 5)

Surface Condition	Thickness (inch)	Width (inch)	a_0 (inch)	c_0 (inch)	Initial Crack Shape Aspect Ratio (a_0/c_0)
Case 4—Baseline	0.1663	0.3991	0.0141	0.0135	1.0444
Case 5—Shot peened	0.1664	0.3985	0.0182	0.0203	0.8966

The remote cyclic force is equivalent to a constant-amplitude uniform stress of 90 ksi at the remote ends with a fixed stress ratio at R = 0.05. In addition to remote stress, static residual stress distributions were also applied. These distributions were measured with the baseline and shot-peened test coupons, and are given in table 19. Respectively, they are designated by baseline and shot-peened. Note that the shot-peened residual stress distribution has a much larger maximum compressive stress near the free surface and extends more deeply into the specimen thickness. The data points used in this analysis only extended as deep as x = 0.03 in., which constituted a thin layer of residual stress, not enough for interpolating the residual stress throughout the thickness. To circumvent that, one additional data pair was appended at the end, using the half-thickness as the last coordinate and using the last available residual stress; i.e., at x = 0.03 in. as its stress value.

Table 19. Residual Stress Distribution (Surface: X = 0)

Residual Stress Gradient					
Baseline			Shot-Peened		
x (in.)	x/t	σ_{res} (ksi)	x (in.)	x/t	σ_{res} (ksi)
0	0.00000	-33.9	0	0.00000	-102
0.002	0.00501	-1.7	0.0025	0.00627	-108.6
0.005	0.01253	-1.9	0.005	0.01255	3.2
0.01	0.02506	-1.4	0.01	0.02509	6.8
0.015	0.03758	-0.3	0.015	0.03764	7.3
0.03	0.07517	1.4	0.03	0.07528	5.8
0.084	0.50000	1.4	0.1995	0.50000	5.8

The 4340 steel M(T) baseline material da/dN test data were used for Cases 4 and 5 (baseline and shot-peened) Kb-Bar test simulation. The NASGRO equation was fit to these data using the NASMAT (crack growth data analysis) module in the NASGRO software to determine specific NASGRO equation parameters. The baseline data had been generated from M(T) coupons of nominal thickness 0.25 in.

Several NASMAT regressions were performed following a trial-and-error approach to optimize the fit for the entire range of stress ratios and FCG rates, with special attention to negative stress ratios (since these were particularly relevant to the specified conditions for the simulations) and the “fanning” behavior of the curves near the threshold region. The numerical values of the key

parameters from the best fit obtained are listed in table 20. Figure 27 shows a comparison of FCG curves derived from the fitted NASGRO equation with the M(T) FCG test data at the five specified stress ratios: R = -1, -0.5, 0.05, 0.5, and 0.8. This plot was generated using the NASGRO NASFLA (FCG simulation) module graphical user interface.

Table 20. Key Parameters Derived From NASGRO Equation Fit

S_{max}/σ_0	0.3
α	2.5
K_c	$110 ksi\sqrt{in}$
ΔK_1	$2.2 ksi\sqrt{in}$
C_{th}^{p}	1.25
C_{th}^{n}	0.1
p	0.25
q	0.25
C	0.787×10^{-9}
N	3.087

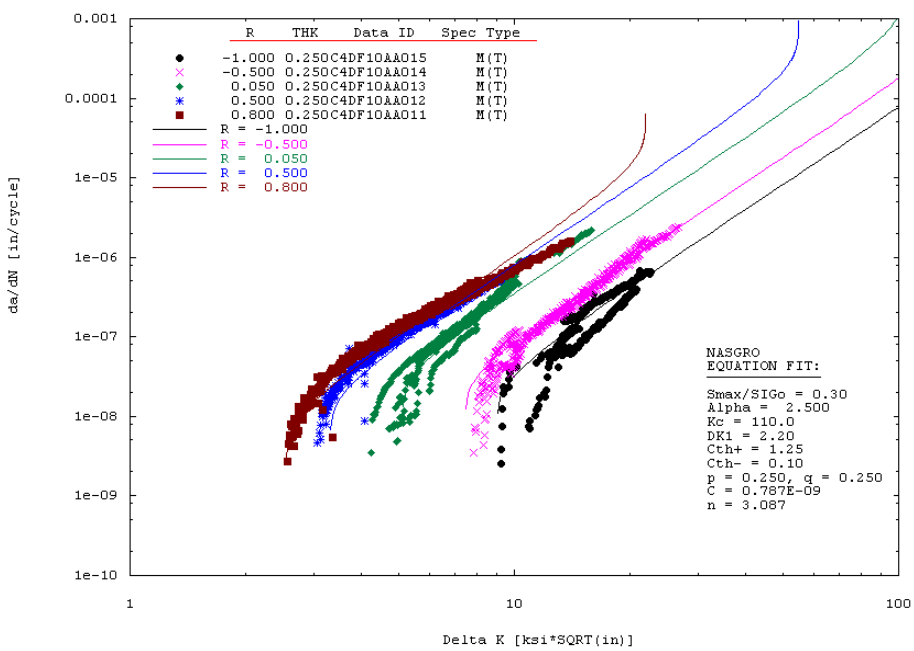

Figure 27. The NASGRO Equation Curve Fits for 4340 Steel M(T) FCG Data

3.1.2 The NASGRO Kb-Bar Simulation Results.

3.1.2.1 The NASGRO Strip-Yield Analysis Without Residual Stresses (Case 1).

The results from the NASGRO strip-yield model analyses of residual stress were obtained. For $R = 0.05$, the resulting crack growth rate (da/dN) is shown in figure 28 as a function of ΔK. Also shown in figure 28 is the da/dN for a simple constant-amplitude test in which the initial P_{max} value was 2480 lb. Figure 29 shows the two crack sizes (a and c) as a function of cycles for the load-shedding test.

One concern with the existing NASGRO strip-yield model was that the artificially high threshold ΔK values may be generated during load shedding, particularly at the high K-gradient $C = -30$ √inch as used in the Kb-Bar tests. The results, however, indicated that the load shedding did not introduce any significant artifacts into the crack closure or crack growth response during the simulated threshold test. The crack growth behavior, as characterized by da/dN versus ΔK, was essentially the same during the load-shedding simulation as it was during a constant-amplitude simulation. This was further verified by comparing the NASGRO strip-yield model results with the NASGRO noninteraction model, shown in figure 30. The differences were very slight and could be explained by the normal differences between the fundamental material model in the NASGRO strip-yield and noninteraction models.

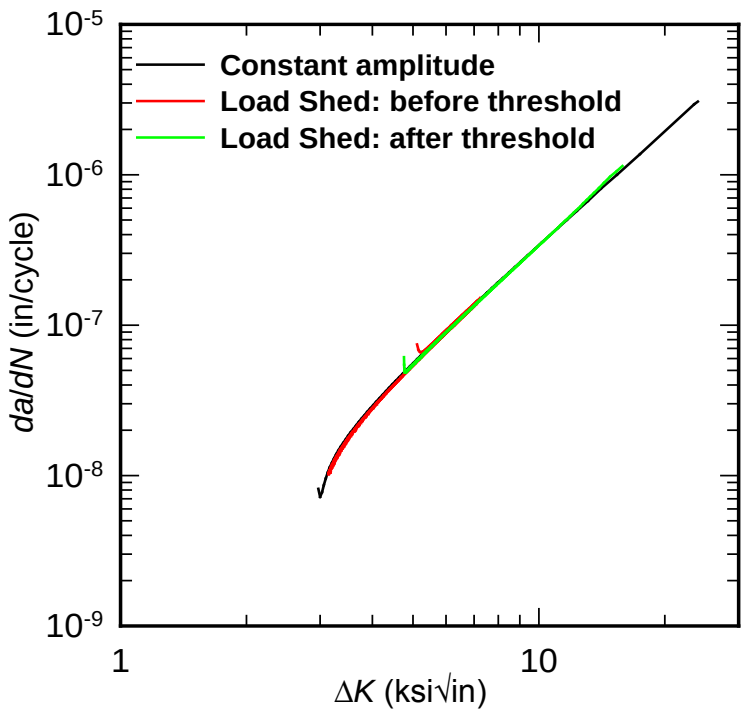

Figure 28. Crack Growth Rate History in Case 1: Kb-Bar Simulations as a Function of ΔK ($R = 0.05$)

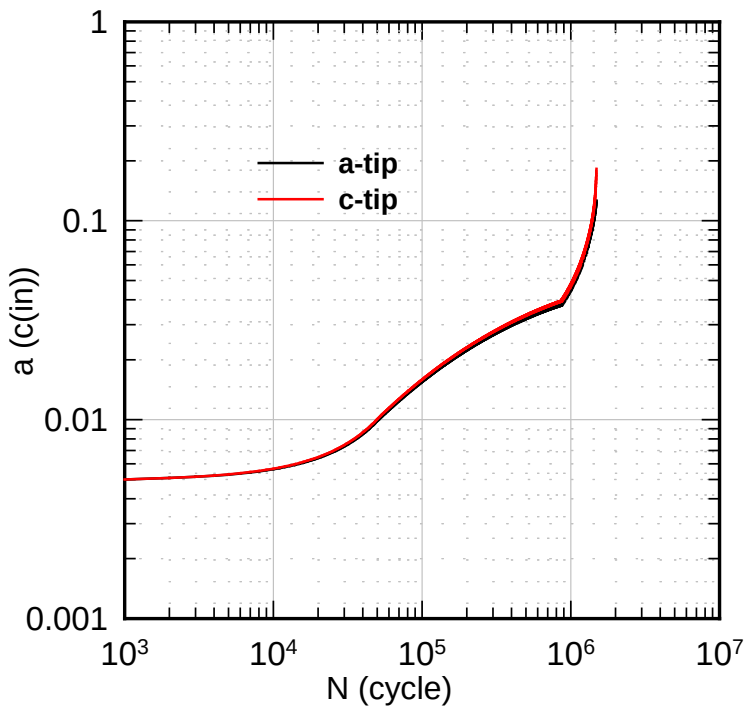

Figure 29. Calculated Crack Size History in Case 1: Kb-Bar Load-Shedding Simulation (R = 0.05)

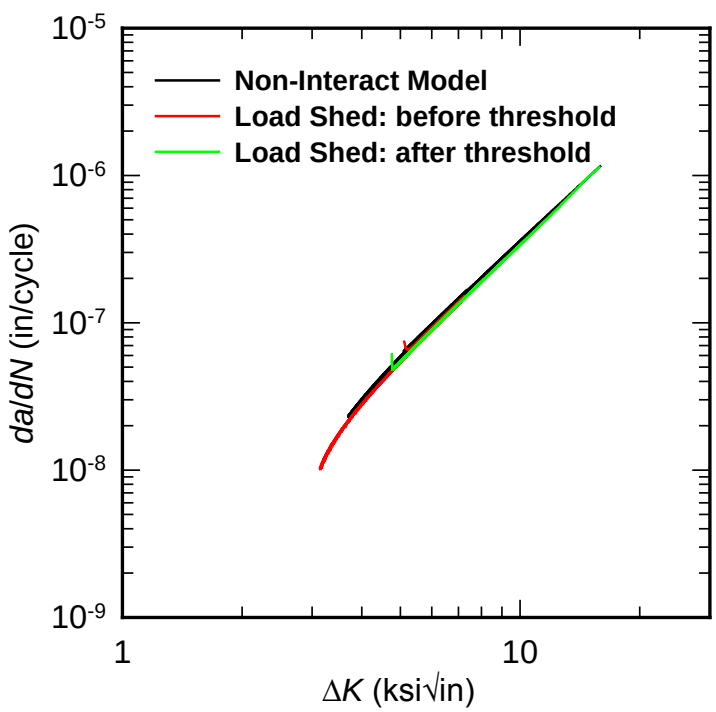

Figure 30. Crack Growth Rate History in Case 1: Kb-Bar Load-Shedding Simulations With Strip-Yield and Noninteraction Models (R = 0.05)

3.1.2.2 Kb-Bar CGA With Shot-Peening Residual Stress (Case 2).

The CGA with the shot-peening residual stress was run with a stress ratio R = 0.05, K-gradient C = -30 in^{-1}, and an initial load P_{max} of 7200 lb. The load interaction approach was used. At P_{max} = 3000 lb (constant amplitude, after the threshold growth), the crack began growing, but only grew for a short time because the crack shape aspect ratio grew outside the bounds of the SC17 solution (*a/c* became greater than 8). This occurred because the severe compressive residual stresses near the surface prevented the surface tips (the *c*-tips) from growing much at all. The deepest tip (the *a*-tip) continued to grow deeper into the specimen until the *a/c* ratio grew too large.

The resulting crack size versus load cycle is shown in figure 31. Note that the calculated SIFs (with the residual stress incorporated) were all calculated at the *a*-tip.

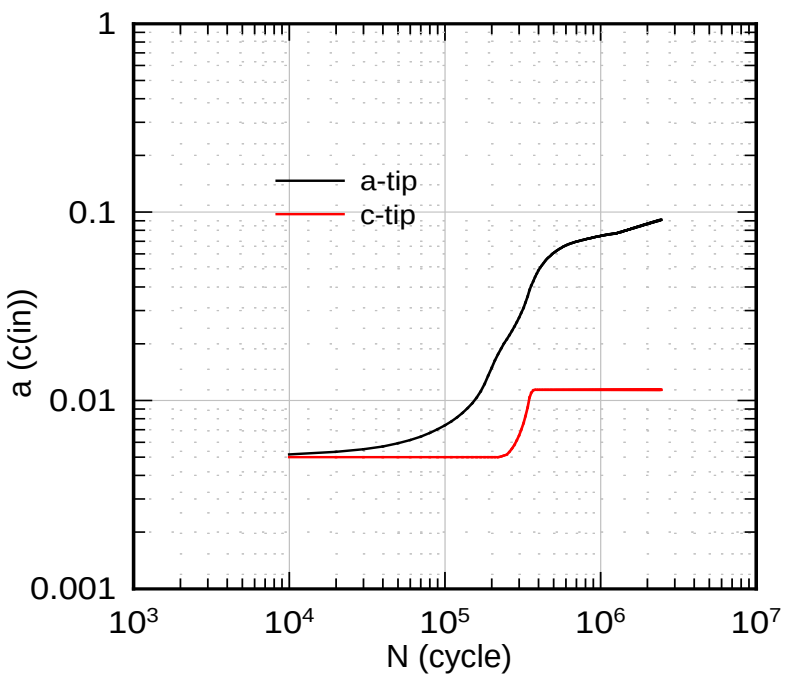

Figure 31. Calculated Crack Size History of Kb-Bar Simulation With Residual Stress (R = 0.05)

3.1.2.3 Strip-Yield Analysis With Actual Testing Load History (Case 3).

The Case 3 NASGRO Kb-Bar CGA was run to model the actual load-shedding history for a particular Kb-Bar specimen. This was done only for the baseline case and included the actual initial crack size following precracking. It was determined that the crack growth behavior with load shedding was very sensitive to simulation parameters, particularly the material crack growth rate (*da*/*dN*). For example, as shown in figure 32, reducing the crack growth rate by about 20% (i.e., shifting the *da*/*dN* curve down 20%) resulted in the originally unarrested crack (figure 32(a)) now arrested during the load-shedding portion of the simulated test (figure 32(b)). This shift was done easily with the "environmental *da*/*dN* multiplicative factor" on the NASGRO Materials tab with a scaling factor on the calculated *da*/*dN* values. The *a*-N curves of the

original and modified NASGRO strip-yield model analyses are compared to the *a*-N curve (figure 33(c)), of which the particular test specimens were modeled for both simulations.

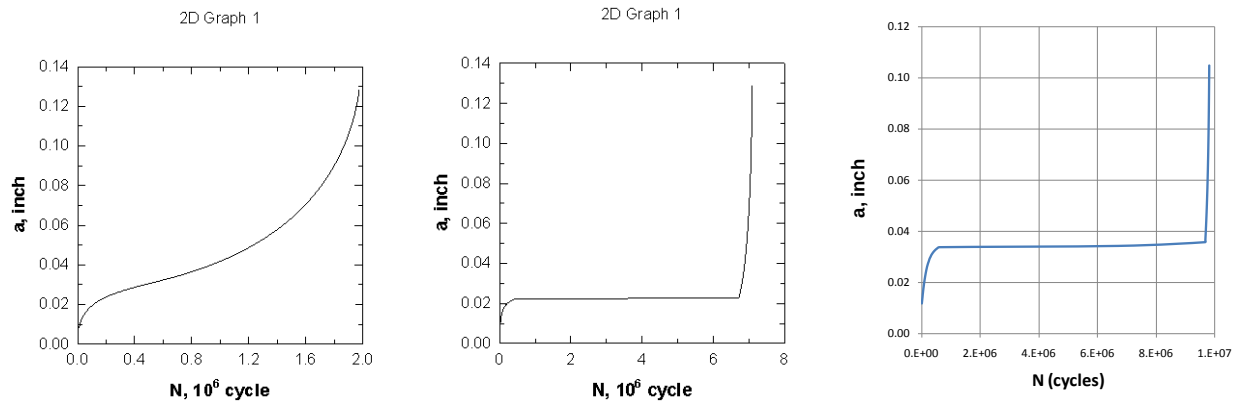

(a) (b) (c)

Figure 32. The *a*-N Curves for Baseline 4340 Steel Kb-Bar Specimen With Load Shedding (a) NASGRO Simulation With Default Material Properties, (b) NASGRO Simulation With 20% Reduced Crack Growth Rate, and (c) Testing *a*-N Curve

3.1.2.4 Baseline and Shot-Peened Kb-Bar Simulations of Actual Tests (Cases 4 and 5).

The NASGRO CGA capability at the coupon level was further evaluated with simulations of actual test parameters. The two test cases were Kb-Bar tests with the as-machined and shot-peened specimens (R = 0.05 for both). The residual stress induced during machining for the baseline Kb-Bar and the residual stress for the shot-peened Kb-Bar were considered. In each case, the measured residual stress profile was applied, respectively. It was exhibited that simulations of shot-peened specimens produced about twice the crack growth life of the baseline specimens: 42,214 cycles for the shot-peened versus 22,821 cycles for the baseline specimen.

The effect of the surface residual stress is most evident for shot-peened specimen simulations, and can also be seen in the baseline specimens. Figures 33 and 34 show the crack growth behavior is fundamentally altered by the residual stress at the *c*-tips on the surface of the shot-peened specimen. In figure 33, the thin lines are material *da*/*dN* properties at various stress ratios.

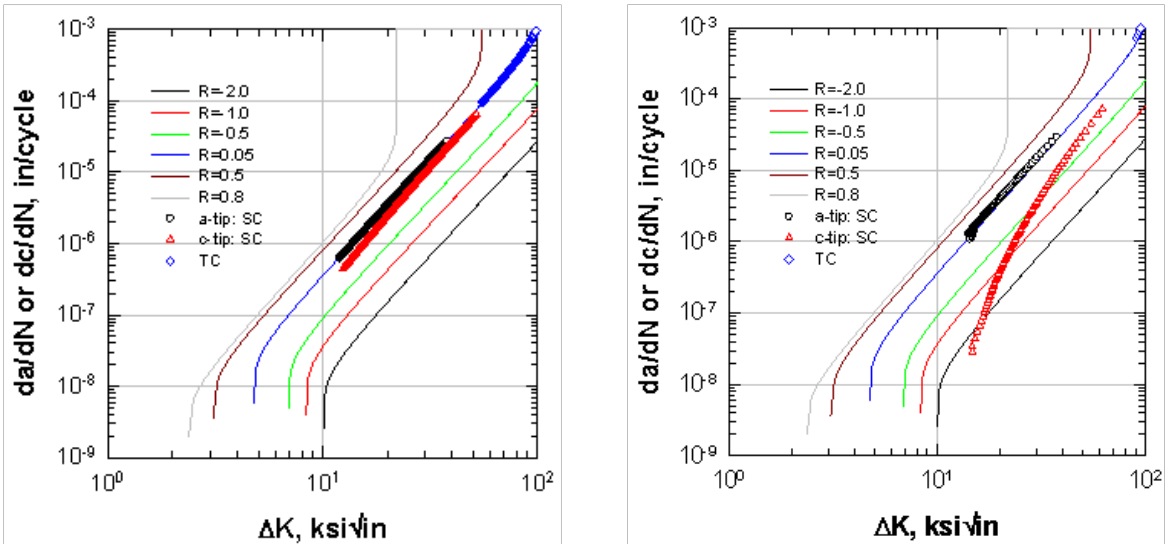

(a) (b)

Figure 33. Variation of *da*/*dN* (*dc*/*dN*) vs Δ*K* During FCG Simulation of (a) Baseline and (b) Shot-Peened Kb-Bar (4340 Steel)

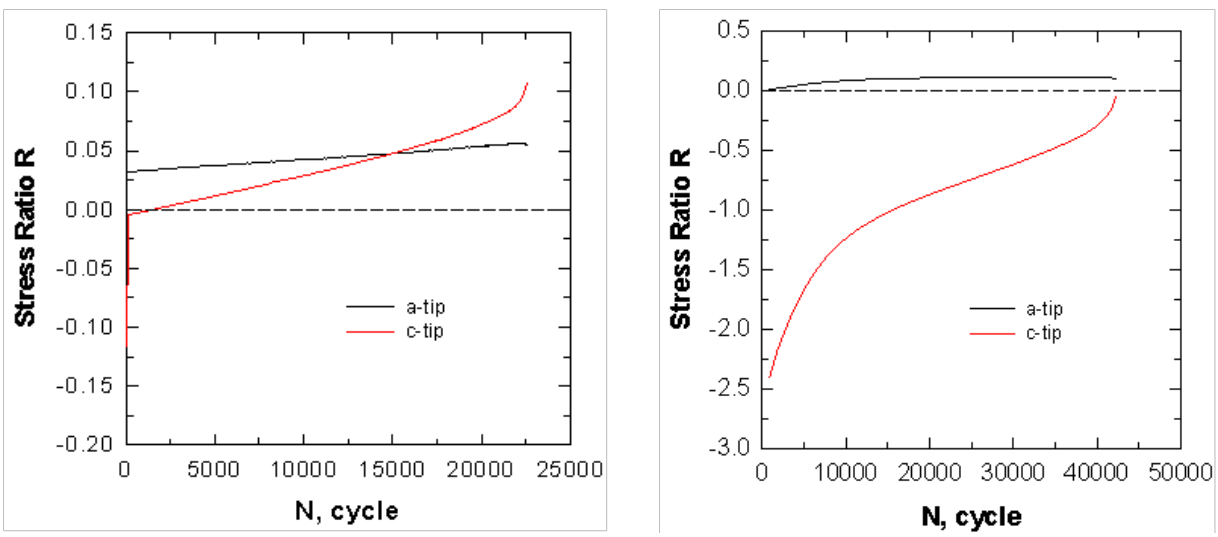

(a) (b)

Figure 34. Variation of Stress Ratio (*R*) as a Function of Cycles for (a) Baseline and (b) Shot-Peened Kb-Bar

3.1.2.5 Comparison of NASGRO Simulation and Experimental Data.

Figure 35 shows comparison of Case 1 baseline simulations with the test data. Although, in this case, the default NASGRO material FCG data were used for the analysis, the simulated FCG *da*/*dN* curves favorably agree with the baseline (unpeened) Kb-Bar test *da*/*dN* versus Δ*K* data. Comparisons of test data and NASGRO simulations are for *R* = 0.05 (figure 35(a)) and *R* = -1 (figure 35(b)).

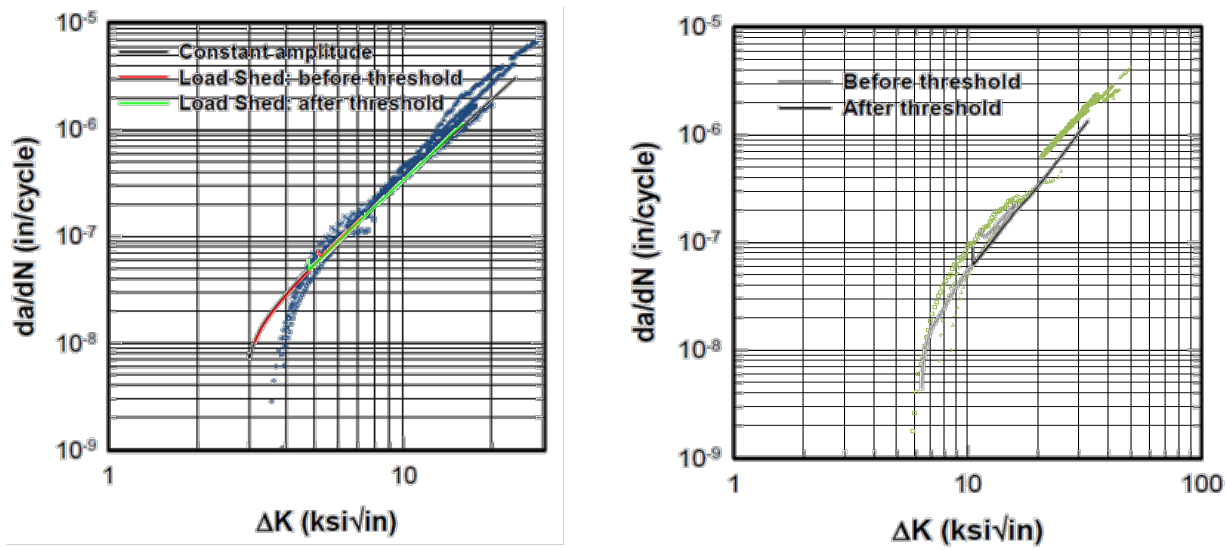

(a) (b)

Figure 35. The *da*/*dN* vs Δ*K* for Baseline Kb-Bar (a) *R* = 0.05 and (b) *R* = -1

A better gauge of the accuracy of the NASGRO simulations was accomplished by comparing crack length versus cycles (*a*-N and *c*-N). Figure 36 shows the *a*-N curve of the baseline simulation compared to the *a*-N curve of the corresponding actual test case with the baseline Kb-Bar simulation overlaid with the baseline Kb-Bar test data. Figure 37 shows the *a*-N curve of the shot-peened Kb-Bar simulation overlaid with the corresponding shot-peened Kb-Bar test data. Note that, in order to compare directly, only constant-amplitude load cases (Paris region) are presented in figures 36 and 37. In addition, all the simulations were "blind" analyses.

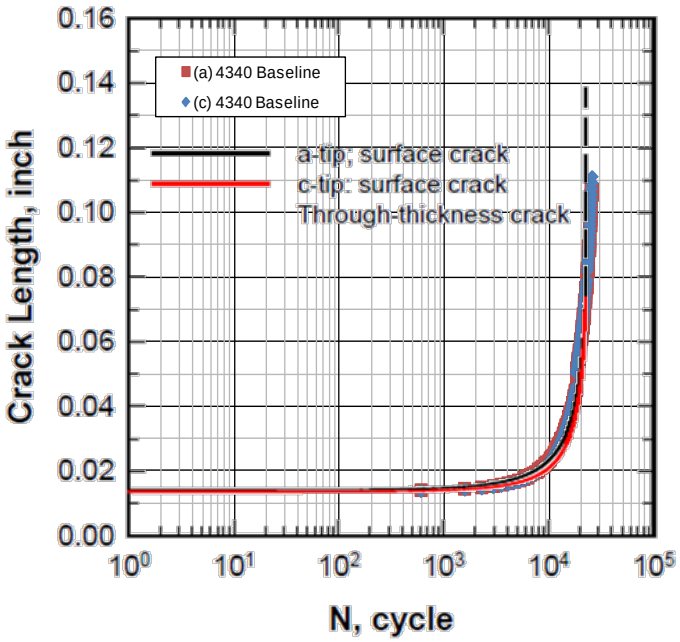

Figure 36. The *a*-N and *c*-N Comparison for Baseline Kb-Bar

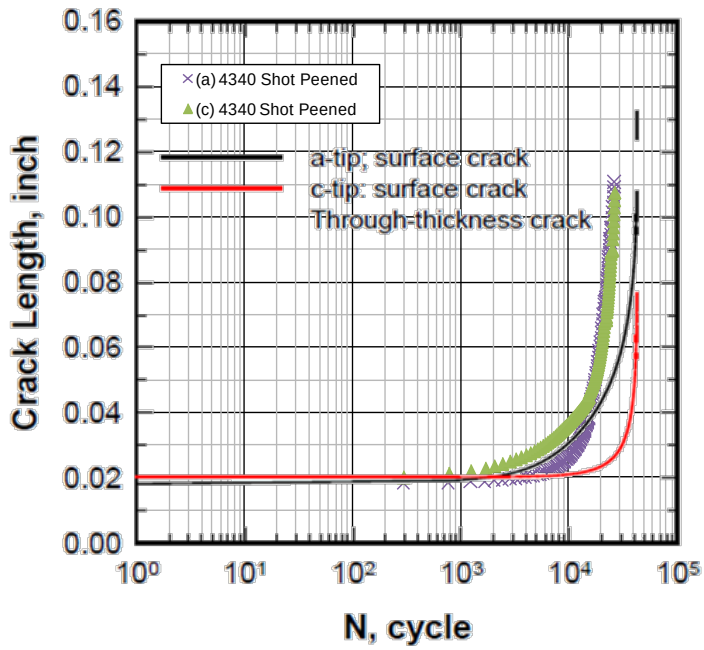

Figure 37. The *a*-N and *c*-N Comparison for Shot-Peened Kb-Bar

For the shot-peened specimen, the NASGRO simulation overestimated the life prediction when compared to the test data in two ways: (1) There was a difference in cycles to failure. The NASGRO simulation predicted approximately one and half times the cycles to failure relative to the test data (figure 37); and (2) there was a difference in the relative growth rates of the crack tips. The simulation predicted faster growth in the depth (*a*) direction and slower growth along the surface (*c*-direction). This was expected, given the compressive residual stress profile imposed on the surface. However, the Kb-Bar test specimen indicated the opposite effect. Unfortunately, only one Paris-region, shot-peened Kb-Bar specimen was tested successfully; therefore, it was not possible to draw any reliable conclusions from this comparison.

3.1.3 Fillet Radius FCG Analysis With NASGRO: SIF Solutions.

The purpose of Phase II was to evaluate NASGRO's current CGA capability to handle complex geometry and complex loading conditions that are representative of a rotor mast. The fillet radius was of special interest because it is a typical geometry of rotor masts and drive shafts. The stress concentration associated with its geometrical features is typically a driver for FCG in parts of this kind. The first step of FCG analysis is to determine the SIF solutions, followed by a CGA, which is described in section 3.1.4.

The geometric specification for the fillet radius element is governed by six parameters: L, W, D, D_1, d, and R, which are shown in figure 38. The surface crack at the exterior cylindrical surface of the hollow shaft is defined by the location of the crack center, its angle, surface length, and depth. The location of the crack center is defined in reference to the location where the fillet merges into the cylindrical exterior surface of the shaft. The circled regions in figure 38 show the exact location of the crack center. The crack angle, θ, is defined with respect to the cross-sectional plane perpendicular to the shaft axis, as shown in figure 39.

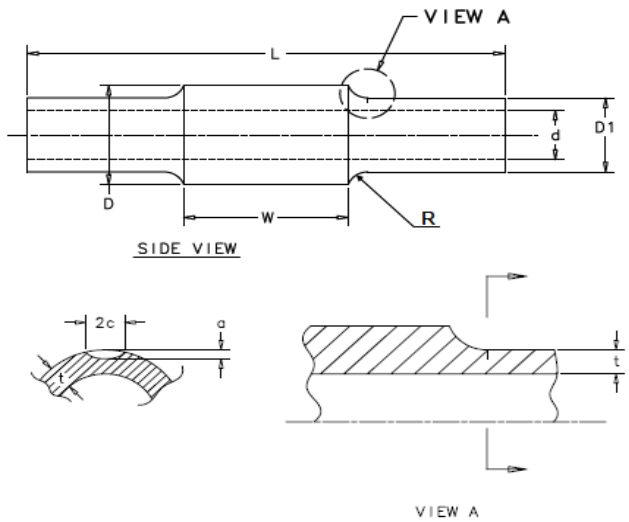

Figure 38. Fillet Radius Element Geometry for the NASGRO Analysis

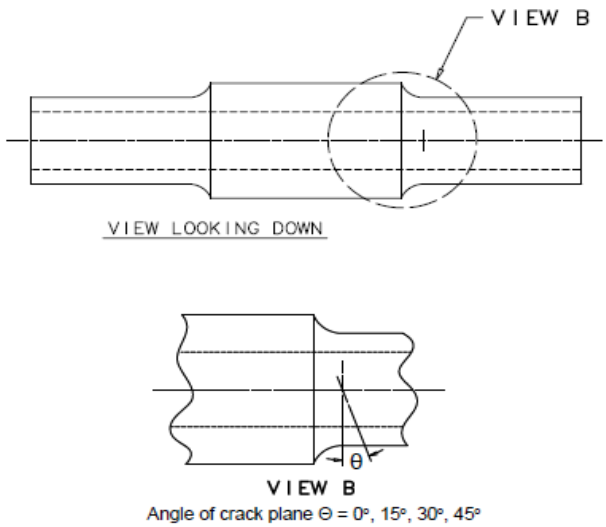

Figure 39. Crack Position of the Fillet Radius Element for the NASGRO Analysis

3.1.3.1 The SIF Solutions With Thrust, Bending, and Torsion.

The mode I, II, and III SIFs (K_I, K_{II}, and K_{III}) for six geometrical parameters of a surface crack at four different angular orientations in eight different fillet radius element geometry combinations were specified. Three reference load conditions were taken into account: axial thrust load or tensile load, bending, and torsion, respectively.

Specifically, the analysis matrix for SIF solutions is listed in table 21. The analysis cases of the fillet radius element geometries are listed in table 22. The surface crack size and shape cases are listed in table 23.

Table 21. Analysis Matrix for SIF Solutions of the Fillet Radius Element

Governing Geometrical Parameters: (L = 10 in.) *W*, *D*, *D*1, *d*, *R*	Number of Element Geometries	Crack Angle (θ)	Surface Crack Size/Shape	Measure of K_I, K_{II}, K_{III}
Run 1	ID 1 in table 24	0°, 15°, 30°, and 45°	All in table 23	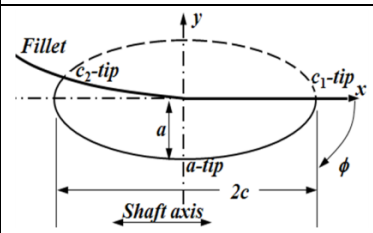 At *a*-tip, c_1-tip, and c_2-tip
Run 2	ID 2~ID 7 in table 24	0° and 45°	*a*/*c* = 0.5: *a* = 0.01, 0.05, and 0.2	

Table 22. Crack Geometry Variations

a (in.)	2*c* (in.)	*a*/*c*
0.01	0.04	0.5
0.01	0.02	1
0.05	0.2	0.5
0.05	0.1	1
0.2	0.4	1
0.2	0.2	2

Table 23. Alternative Fillet Element Geometry Variations

Configuration ID	*R* (in.)	*D* (in.)	*D*/*d*	D_t/d	*R*/*D*	*W*/*D*
1	0.1	1.25	1.812	1.646	0.08	1.6
2	0.1	1.25	2.718	1.646	0.08	1.6
3	0.1	1.25	2.265	1.646	0.08	1.6
4	0.1	1.25	2.718	2.469	0.08	1.6
5	0.1	1.25	1.812	1.235	0.08	1.6
6	0.15	1.25	1.812	1.646	0.12	1.6
7	0.067	1.25	1.812	1.646	0.053	1.6
8	0.1	1.25	1.812	1.646	0.08	1.067

The FADD-3D hybrid finite element (FE)/boundary element (BE) software was used by Southwest Research Institute® (SwRI®) to calculate SIFs for semielliptical planar surface cracks in a fillet radius element under axial loading, bending, or torsion, as shown in figure 40. SIFs were calculated as a function of elliptical angle designating the crack tip location along the crack perimeter for three fracture modes: modes I, II, and III. For practical reasons, SIF solutions at

two surface tips and the deepest tip were extracted through interpolation. The examples of SIFs for a = 0.05 in., 2c = 0.1 in., and a/c = 1 in. are shown in figures 41 through 43, in which the SIF is normalized by $\sqrt{\pi a}/\Psi$, where Ψ is the shape factor defined by $\sqrt{1+1.464(a/c)^{1.65}}$ for $a \le c$.

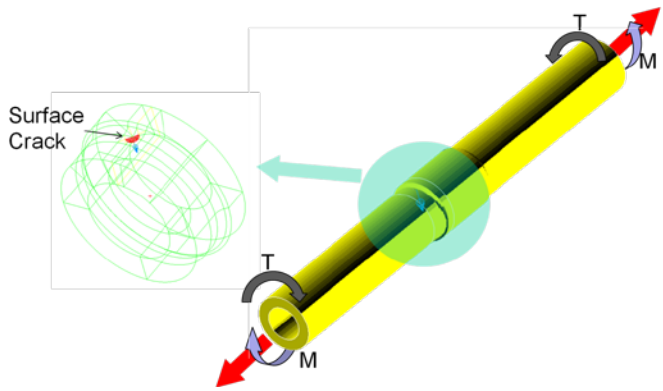

Figure 40. The FADD-3D Hybrid FE/BE Model of the Fillet Radius Element for SIF Solutions

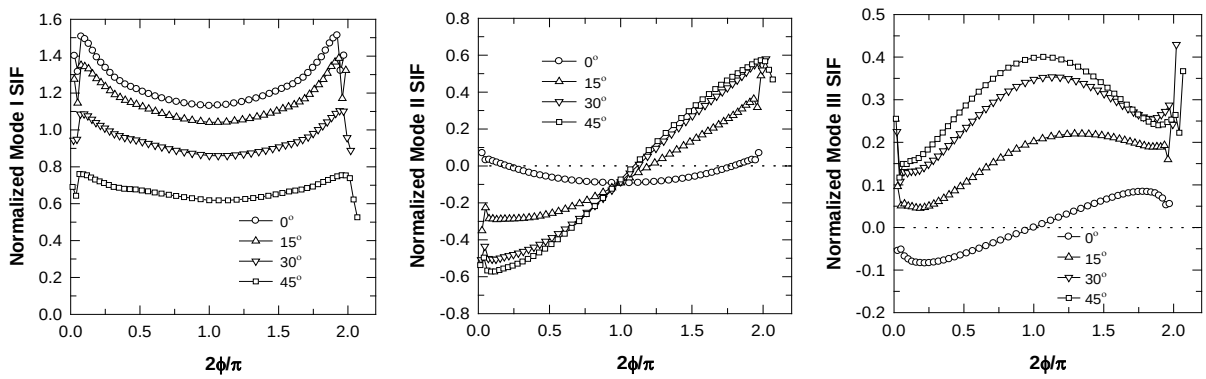

Figure 41. The SIF Solutions as a Function of Elliptical Angle Subjected to Remote Tension

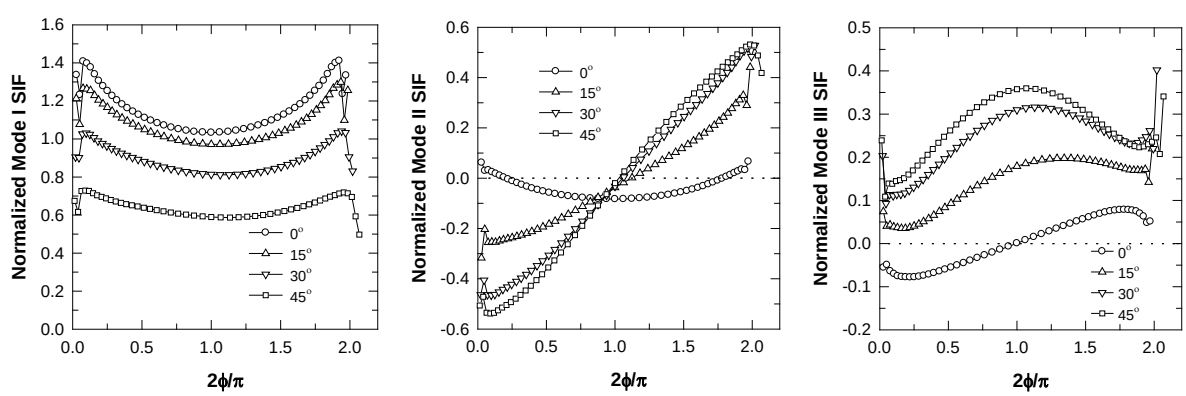

Figure 42. The SIF Solutions as a Function of Elliptical Angle Subjected to Remote Bending

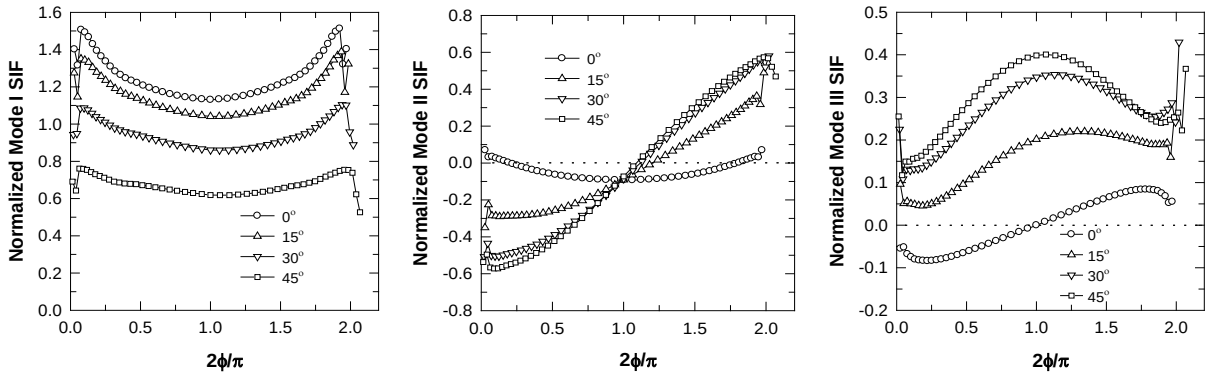

Figure 43. The SIF Solutions as a Function of Elliptical Angle Subjected to Remote Torsion

3.1.3.2 The SIF Solutions With Actual Test Loading Conditions.

In this analysis, the loading conditions of the actual tests were applied to directly compare the follow-on FCG analysis results to the test data. The geometries of the fillet radius element test specimen, shown in figure 44, were used to first calculate SIF solutions and then run NASGRO FCG simulations. The two loading conditions were (1) M = T loading case and (2) M = 2T loading case, where M stands for bending moment and T for torsion. Both the bending moment and torsion were induced by applying a single shear, V, as shown in figure 44. The actual test loading conditions are listed in table 24.

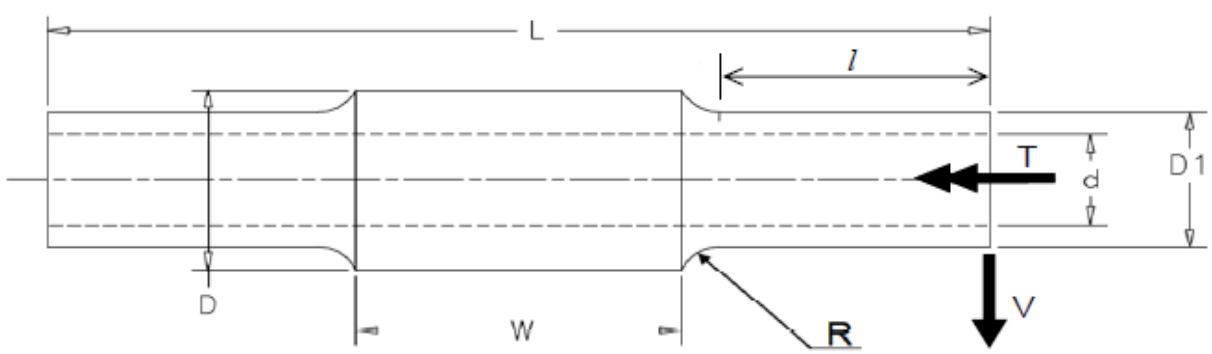

l = 4.95 in. (therefore, M = 4.958*V)
d = 0.69 in.
D = 1.25 in.
*D*1 = 1.136 in.
R = 0.10 in.
W = 1.33 in.

Figure 44. Actual Test Specimen Geometries of the Fillet Radius Element for SIF and NASGRO Simulation

Table 24. Actual Testing Loads for NASGRO Simulation of Baseline Fillet Element Specimen

4340	M = T**				M = 2T			
	V (lb)	T_{max} (in-lb)	σ_1 (ksi)	θ	V (lb)	T_{max} (in-lb)	σ_1 (ksi)	θ
Baseline	764	3787	55*	30°	844	2093	55*	15°

T_{max}= Maximum load
*Reference remote stress at notch location
**T = torsion, M = bending moment, produced by applying shear load, V, 4.958 inches from notch

For the given load combination of V, M, and T, a separate FEA determined that the maximum principal stress occurred in the fillet radius area in the direction of 30° from the shaft axis for the M = T load case, and 15° for M = 2T load case. Accordingly, a notch of θ = 30° was induced for the test specimen under an M = T loading condition, and a θ = 15° notch was induced for the test specimen under an M = 2T loading condition, where θ is the angle between the crack (or notch) plane and the cross-section plane of the element, as shown in figure 42. Therefore, the SIF solutions must be calculated for the two notch angles (15° for M = 2T and 30° for M = T) and various possible crack dimensions. The proposed K-solution matrix is shown in figure 45.

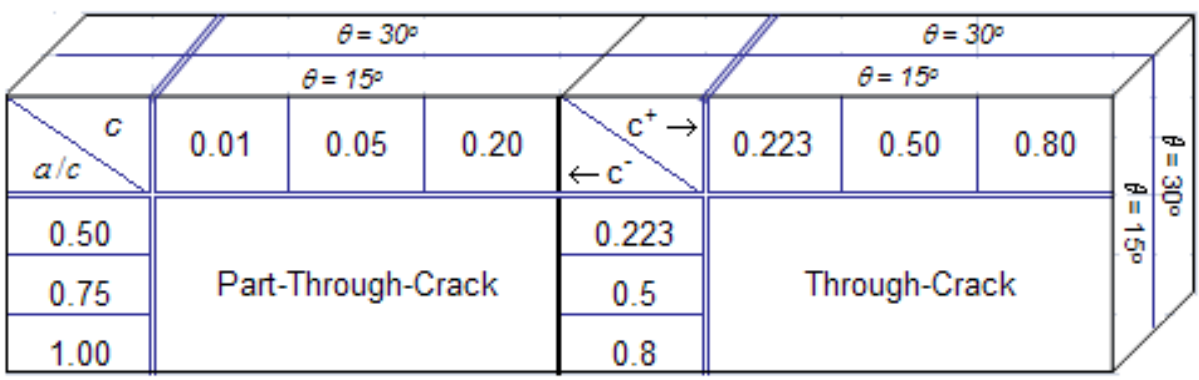

Figure 45. The SIF Solution Matrix for Actual Test Loading Conditions

For each geometry, K_I, K_{II}, and K_{III} solutions were required, and the transition from a surface/part-through crack to a through crack was assumed to occur at $a = c = 0.223$ in. θ is the angle formed by the normal to the notch plane and the shaft axis.

The SIF solutions were developed for the two stages of crack growth in the fillet radius area: surface (part-through) crack and through crack. The SIF solutions for a crack growing in the fillet radius element specimen were determined using a hybrid FE/BE model. The BE section is shown in figure 46.

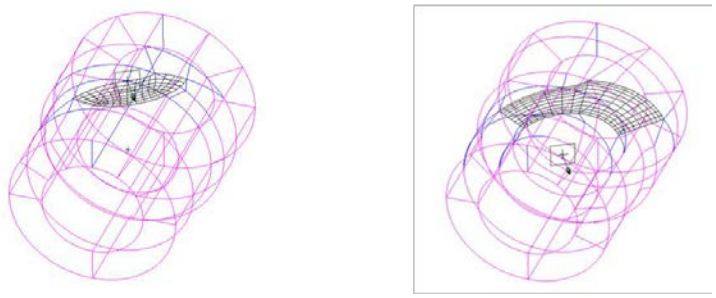

(a) (b)

Figure 46. Boundary Element Section of Hybrid Models for a 30° Crack in a Fillet Radius Element (a) Irregular Surface Crack and (b) Irregular Through-Thickness Crack

An example plot is shown in figure 47. It describes the normalized SIF variations along the crack tip perimeter of all three fracture modes under the actual mixed-mode test loads. In this case, the crack plane angle is 30°, and the geometric ratios are a/t = 0.04484 and a/c = 0.5, where t is the thickness of cylinder D_1. The remote ends were subjected to the shear force only. The normalization factor

$$\sqrt{\pi a}\Big/\Phi$$

in the ordinate axis consists of the crack depth a and the shape factor defined by

$$\Phi = \sqrt{1+1.464(a/c)^{1.65}}$$

with a/c always less than 1. Note the normalized elliptical angle can vary from 0 to slightly larger than 2.0 because the c_2-tip in this case is in the fillet region.

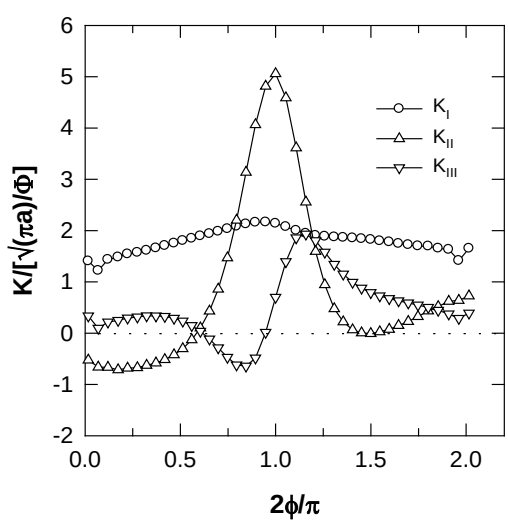

Figure 47. Normalized SIF Variations Along the Crack Front of Surface Crack (θ = 30°, a/t = 0.04484, and a/c = 0.5 under remote shear)

For through-thickness cracks, two separate sets of SIFs were identified corresponding to the SIF variations along the crack tip perimeters of the c_1 and c_2 tips. They were extracted and generated as a function of normalized distance measured from the most inner point (on the bore). The averages of SIF values spanning across the crack tip front were selected to represent the SIFs at the tip. For example, figure 48 shows the SIF variations across the straight crack tip perimeter at c_2 tip. The remote ends were subjected to reference shear force. The crack plane angle was 15°. The arc angles were β_1 = 21.734° and β_2 = -21.734°, respectively, leading to $c_1 = c_2$ = 0.223 in. The ordinate plots the absolute SIF values in reference to the applied shear force. No normalization was made. The averages of the three fracture mode SIFs were determined through numerical integration and used as the representative SIFs of all three fracture modes associated with this crack tip. In the plot, they are denoted by the long dashed lines.

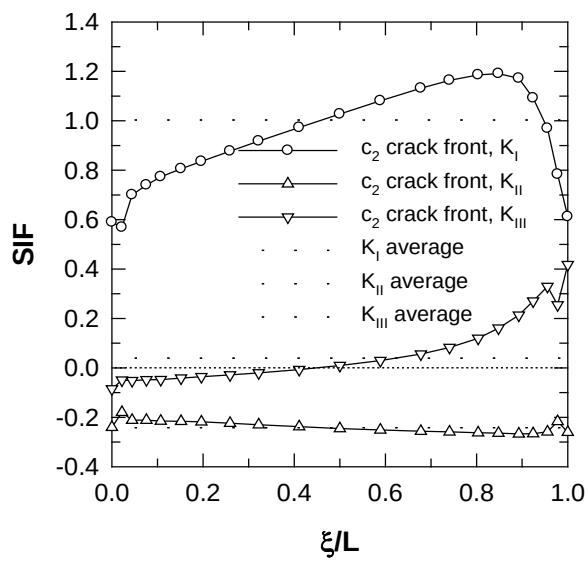

Figure 48. The SIF Variations Along the Crack Tip Perimeter of c_2-Tip of Through-Thickness Crack (θ = 15° and $c_1 = c_2$ = 0.223 in., under remote shear)

SIF solutions are tabulated in appendix B for the various expected loading cases, crack shape aspect ratios, and crack plane angles.

3.1.4 Fillet Radius FCG Analysis With NASGRO: CGA.

3.1.4.1 Loading Conditions and Assumptions for Fillet Radius Element FCG Analysis.

FCG simulations were performed for cracks in the fillet radius element under mixed-mode loading. The specific geometric features and dimensions for the fillet radius element are shown in figure 39. The side view in figure 44 also schematically shows the designated orientations of two load types applied at the remote ends: shear force V and torque T. Shear V produces bending moment M on the element. The magnitudes of the loads are defined in table 24. In reference to the location of the crack, the shear force is designated as positive when applied downward to open the crack, and the torque is designated as positive when its resultant axis points toward the shaft.

This specific load/geometry configuration results in a mixed-mode analysis. Since the current NASGRO production release does not support mixed-mode analysis, two assumptions and simplifications were made to minimize the effects of mixed-mode cracking, within the existing framework of NASGRO:

- The effects of mode II SIF (K_{II}) and mode III SIF (K_{III}) were ignored.
- All cracks were assumed to remain planar, continuing along their initial angular orientation.

The simulation was run under constant-amplitude loading (R = 0.05 in.). The initial notch dimensions were $a_0 = c_0$ = 0.015 in. As listed in table 24, the orientation of the notch was 30° from the cross section for the M = T load case and 15° for the M = 2T load case. Only mode I SIFs were considered for CGA in the given initial crack plane. Table 21, with the previously obtained SIFs (section 3.1.3), was integrated into NASGRO framework, and the K_I value that was needed during the FCG analysis was then interpolated from the look-up table. Two sets of material data were used for the simulations: (1) material data set (material ID C4DF13AB1) from the NASGRO database and (2) the M(T) test data.

During the NASGRO fillet radius element FCG simulation, the shape and dimensions of the crack remained within the boundaries of the solution space, or validity limits; or the NASGRO FCG simulations stopped with an error message if the crack growth exceeded the solution limits. The crack tip perimeter of all surface cracks remained governed by the same geometric definition for an ellipse. The crack transition was assumed to occur when the depth of the surface crack exceeded 0.2 in. or a/t = 0.897, where $t = (D_1\text{-}d)/2$ = 0.223 in. is the wall thickness of the smaller shaft section. The transitioned crack type was a through-thickness crack and, initially, was symmetrical. The initial surface length of the transitioned through-thickness crack was assumed equal to $2t(c/a)_{tr}$, where $(c/a)_{tr}$ denotes the crack shape aspect ratio at transition. For either a surface (part-through) crack or a through-thickness crack, only two degrees of freedom were simulated and traced independently.

3.1.4.2 The FCG Simulation of Fillet Radius Element

Two cases of NASGRO FCG simulations were run for the fillet radius element: one used the NASGRO material database for the 4340 steel and the other used the M(T) material properties for the same material. The calculated lifetimes based on the M(T) test data are roughly 20% shorter than those calculated using the NASGRO material data set library properties. Predicted fatigue lives for each case are shown in table 25. The two load cases (M = T and M = 2T, table 25) with the material constants obtained from the NASGRO material library for 4340 steel were applied for FCG simulations. The initial crack sizes were a = 0.015 in. and c = 0.015 in., resulting in an initial crack shape aspect ratio of a/c = 1.0 in. In both cases, the length of the c_1-tip was always slightly larger than the length of the c_2-tip. This could be a result of the larger wall thickness the c_2-tip encounters, resulting in smaller crack increments.

Table 25. Predicted Fatigue Life of Fillet Radius Element (Baseline)

Load Case	Predicted Fatigue Life	
	NASGRO Material Database	M(T) FCG Material Properties
M = T	412,009 cycles	346,713 cycles
M = 2T	382,911 cycles	311,379 cycles

Figure 49 shows the crack length versus fatigue cycles for both load cases, where BH01 is the surface crack and BH02 is the through-thickness crack. The crack lengths at the *a*- and *c*-tips before transition and the surface lengths at the c_1- and c_2-tips after transition are plotted. Note that when the crack depth *a* of the surface crack in the M = T load case reached 0.2 in., the crack shape aspect ratio was $(a/c)_{tr}$ = 0.777 with *c* = 0.258 in. By comparison, the crack depth in the M = 2T load case reached 0.2 in. when the surface crack length was 0.285 in., meaning that $(a/c)_{tr}$ = 0.701.

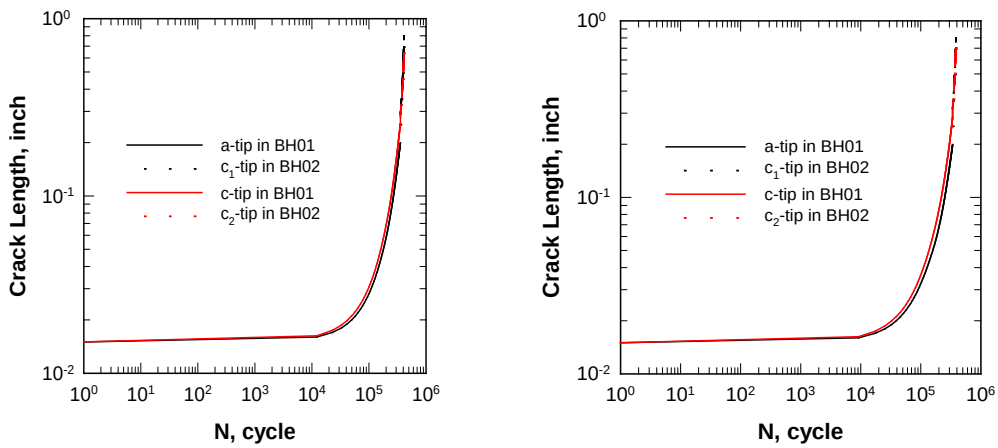

(a) (b)

Figure 49. Computed Crack Lengths as a Function of Fatigue Life Cycles Based on NASGRO Library Material Data (a) M = T Load Case and (b) M = 2T Load Case

Figure 50 shows the variations of crack length as a function of fatigue cycle for both load cases, based on the M(T) FCG test data. Right before the surface crack transitions, the crack depth *a* in the M = T load case reached 0.2 in. and the crack shape aspect ratio was $(a/c)_{tr}$ = 0.758 with *c* = 0.264 in. By comparison, the crack depth in the M = 2T load case reached 0.2 in. when the surface crack length was 0.285 in., resulting in $(a/c)_{tr}$ = 0.661.

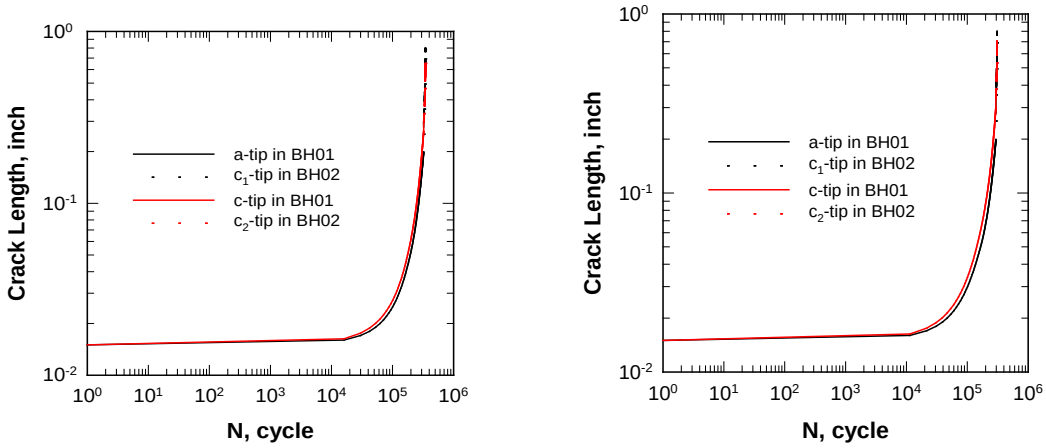

(a) (b)

Figure 50. Computed Crack Lengths as a Function of Fatigue Life Cycles Based on M(T) Test Data (a) M = T Load Case and (b) M = 2T Load Case

3.1.4.3 Comparisons Between NASGRO Analysis and FCG Test Results.

The NASGRO simulations were performed "blind" to the test results so a direct comparison could be made. Figure 51 shows the *a*-N curves for (a) M = T (BH01) and (b) M = 2T (BH02), in which the large dot curves are the test data and the solid and dash lines are the NASGRO analysis results. As figure 51 shows, the NASGRO simulations agree well with the test data.

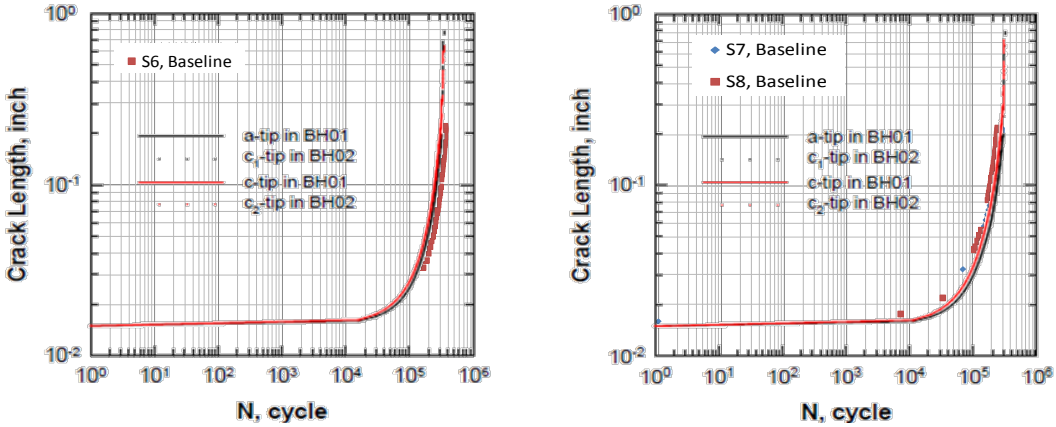

(a) (b)

Figure 51. Comparison of Test Data and NASGRO Simulation: *a*-N Curves for Baseline Fillet Radius Element With (a) M = T Load Case and (b) M = 2T Load Case

One of the difficulties in analyzing the fillet element test data was the definition of the tip-to-tip length on the surface (*c*-tip length). For this reason, the test data plotted in figure 51 are for the *a*-tips only.

Because of the agreement between the NASGRO FCG prediction and the FCG test data of the fillet radius elements, the following observations were made:

- The geometrical simplification of the analysis configuration for the FE/BE modeling was representative of the geometrical features and boundary conditions of the actual test specimens.

- The actual M(T) FCG test data could be integrated into the NASGRO as user-defined properties for accuracy of FCG simulations.

- The SIF solutions for the mixed-mode conditions, determined by the complex geometries and loading applications, could be developed in separate FE/BE platforms and integrated into the NASGRO framework for FCG analysis.

- The NASGRO FCG analysis used a two-dimensional (2D) assumption for a planar crack growth, which, to a large extent, simplified the complex 3D nonplanar crack growth problem with a reasonable fidelity of life prediction.

3.1.5 The Current NASGRO CGA Capability.

The current NASGRO CGA capability to perform an FCG analysis of rotor mast was evaluated. The analyses were demonstrated by FCG simulations of a rotor mast. 4340 steel, the typical rotor mast material, was used. The FCG analysis of a Kb-Bar configuration was performed to simulate the surface crack growth at a coupon level with a simple geometry and loading application. The analyses were run with baseline and shot-peening residual stress conditions. The FCG simulations were also performed at the element level with complex geometries and loading conditions that are representative of a rotor mast. NASGRO was evaluated on its capability to handle the complex geometries, and loading conditions led to the mixed-mode of stress intensity at the crack front. The analysis results were then compared to the test data at both the coupon and element levels.

At both the coupon and element levels, the simulations were performed with the material FCG properties from the NASGRO Material Library and from the M(T) FCG test data of the same batch materials for the Kb-Bar and element test specimens. The purpose of running with the two material sets was to evaluate the applicability of the NASGRO material library data to the rotorcraft drive system parts and to check the ability of integrating user-defined property data. The results based on the two material resources were comparable, indicating NASGRO's capability to handle user-defined material FCG properties.

NASGRO has an SIF library for the typical crack shapes under simple load. For more complex geometries and loads, SIF solutions can be developed in a separate FE/BE analysis platform. The obtained SIF table can be integrated into NASGRO for FCG analysis. For the residual stress case to be considered, the residual stress can be imposed into the FE/BE model to modify the SIF solutions.

The NASGRO simulation for the baseline Kb-Bar FCG was favorably comparable to the Kb-Bar baseline test data. The simulation for the shot-peened Kb-Bar FCG was comparable to the test

data at *a*-tip, but underestimated at *c*-tip. Shot peening induced a thin layer of cold-worked and residual stress gradient on the surface that, not only changed the material properties in this layer, but also the actual stress ratio during crack growth. The mechanism was not fully understood and, thus, the FCG models used for the analyses might not be accurate.

The current state-of-the-art technology for FCG analysis is limited to 2D planar cracks. The DT community has been making an effort to achieve 3D capability. Therefore, a 2D planar crack growth was assumed for the fillet radius element FCG analysis. The results showed that the NASGRO analysis successfully predicted the FCG of fillet element specimens to a high degree of accuracy, indicating that the planar assumption of FCG to simplify the 3D CGA is acceptable for sufficient fidelity in this specific analysis. Although there is insufficient data to support a conclusion, the observation gives a certain level of confidence to using 2D CGA for a fillet radius crack problem as a simplification of the 3D CGA. Furthermore, unlike the actual fillet radius element test specimen, the element configuration for the analysis focused only on the geometrical features that were supposed to be critical to the crack growth at the fillet radius area. The simplification was made to improve computational efficiency and to reduce the probability of inaccuracy in complex modeling. The consistency between the analysis results and test data of the fillet radius element confirms the feasibility of the geometrical simplification assumed for the NASGRO FCG analysis. The SIF solutions generated by SwRI for the complex geometries and mixed-mode loads were validated by the close agreement between the analysis results and the test data. The potential of the software to model such complex situations is evident.

3.2 EVALUATION OF ANSYS ON CGA CAPABILITY.

ANSYS is a general purpose FEA program that has certain capabilities of fracture mechanics analysis. Using a 2D or 3D FE model embedded with a crack or multiple cracks, ANSYS calculates the stress field around the crack tip or the crack front. The analysis results are then input into its postprocessor to calculate the SIFs (modes I, II, and III) or J-integral.

Quadratic elements with mid-side nodes are used to mesh the FE model. To more accurately simulate the singular phenomenon of stress around the crack, mid-side nodes adjacent to the crack tip or crack front must be relocated to the quarter position. This process can be accomplished by using the user-developed ANSYS macros for improved efficiency. Two ANSYS macros were created to facilitate the analysis: (1) a macro to automatically generate the FE model of a Kb-Bar with prescribed crack size for SIF solutions and (2) a macro to create stress-singular elements around the crack front of any 3D FE model.

ANSYS does not have built-in CGA capability. It does not have the function to perform CGA on a component with an embedded crack or surface crack, although it is able to model and solve for SIFs of modes I, II, and III. The user may use ANSYS Parametric Design Language to create macros to automate the solution procedure for SIFs and to perform CGA. Therefore, ANSYS completely relies on the user's knowledge of fracture mechanics and their skill in numerical analysis to accomplish CGA. Based on this, an evaluation of the capability of ANSYS to implement FCG analysis for rotor mast and drive system components was conducted.

The implemented schematic of the CGA is shown in figure 52. The SIF computations performed include the modeling and analysis of the Kb-Bar specimen, spline element, and fillet element.

The developed technical approach, preliminary results, and observations are described in sections 3.2.1 through 3.2.5. In particular, several ANSYS macro codes, similar to user-defined subroutines, were developed to perform CGA in conjunction with ANSYS SIF solutions.

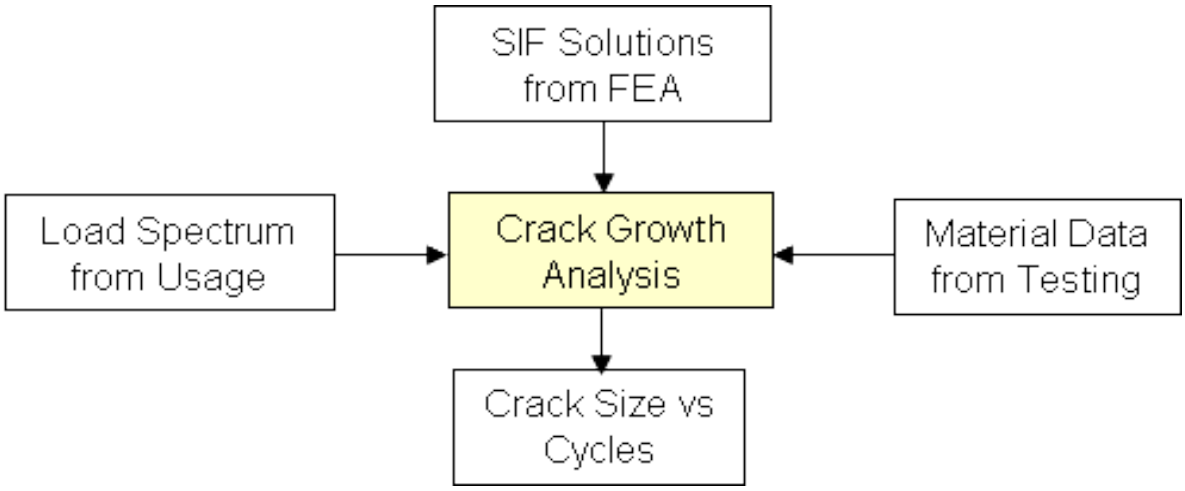

Figure 52. The CGA

3.2.1 The Kb-Bar SIF Solutions With ANSYS.

3.2.1.1 Automated Kb-Bar Modeling in ANSYS.

The Kb-Bar FCG tests were conducted to characterize FCG of surface cracks. FE fracture mechanics analysis was performed to simulate the Kb-Bar specimen tests and, thus, to verify the accuracy of the analysis results and to validate the analytical method. To generate SIF solutions for propagating cracks of various sizes and shapes, a computational routine was developed to automatically generate the FE model of a Kb-Bar with predefined crack size and crack shape aspect ratio. The execution loops of the SIF calculation can only be prompted for an SIF solution or embedded in the loop of a CGA. The flow chart for the Kb-Bar SIF solution is shown in appendix C.

Figure 53 shows a solid model of the Kb-Bar configuration and figure 54 shows half an FE model with the elliptical crack face exposed. This Kb-Bar model is fixed at one end while the other end is subjected to a 1000-psi uniform stress. Figure 55 shows the crack area stress fields of the Kb-Bar.

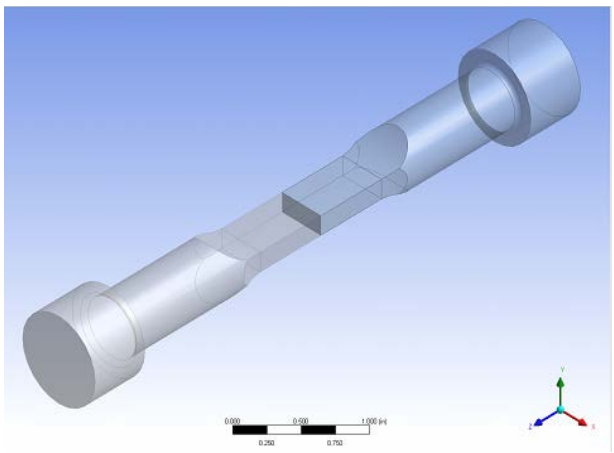

Figure 53. An FE Model of Kb-Bar Configuration

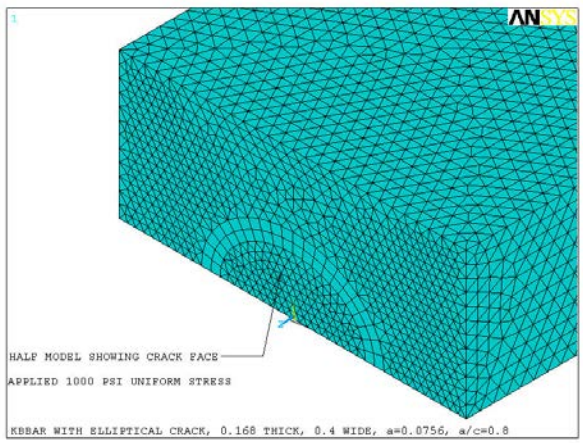

Figure 54. Half a Kb-Bar FE Model With the Elliptical Crack Surface

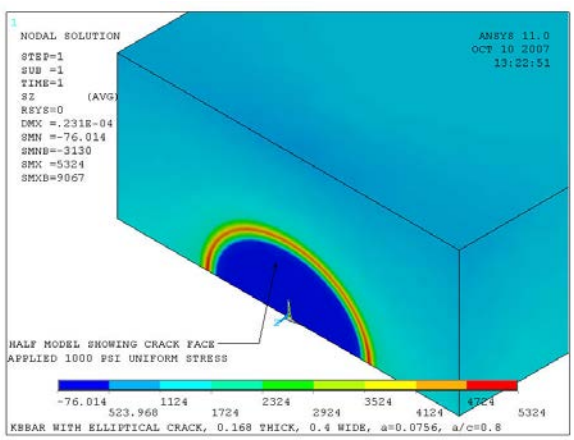

Figure 55. Stress Fields in Crack Area of a Kb-Bar Specimen

3.2.1.2 Determination of Geometrical Factor for SIF Solution.

SIFs are the driving forces at crack fronts for crack growth and are functions of applied load (stress), crack size, crack shape, and component geometry, as generally expressed:

$$K_I = \beta\sigma\sqrt{\pi a}$$

Since β is independent of applied load, it would be more beneficial to determine β for a specific Kb-Bar and crack shape for CGA. With a fixed *a*/*c* ratio, where *a* is the crack depth and *c* is the half crack width on the surface, the values of β versus *a*/*t* can be calculated by looping the aforementioned macro, where *t* is the apparent thickness of the cross section. This information is needed for the CGA algorithm to predict the crack propagation in an analysis model. Figure 56 shows the resulting β values versus *a*/*t* for the Kb-Bar with a semicircular crack, plotted against the values calculated using equation K1010 of CRKGRO in reference 33. The plot shown in figure 57 is for the semielliptical crack with an *a*/*c* ratio of 0.8. These plots show the β value of the FE solution at the crack depth agrees very well with the CRKGRO value up to about half the crack depth. However, the difference between these two values at the surface is roughly 10%, which might be caused by edge effects. The accuracy and validity of the solution need to be investigated further.

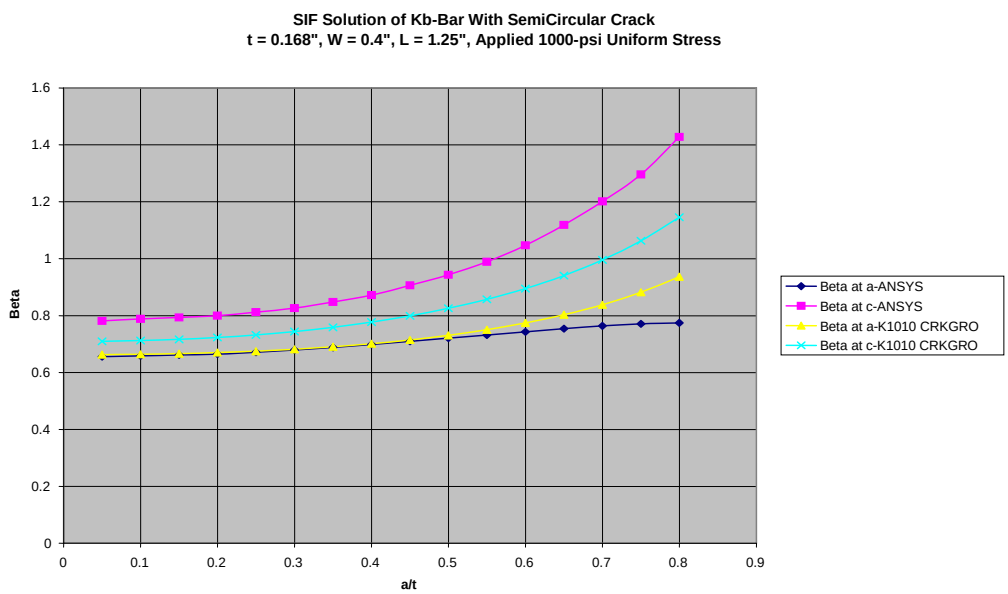

Figure 56. β vs *a*/*t* for the Kb-Bar With a Semicircular Crack

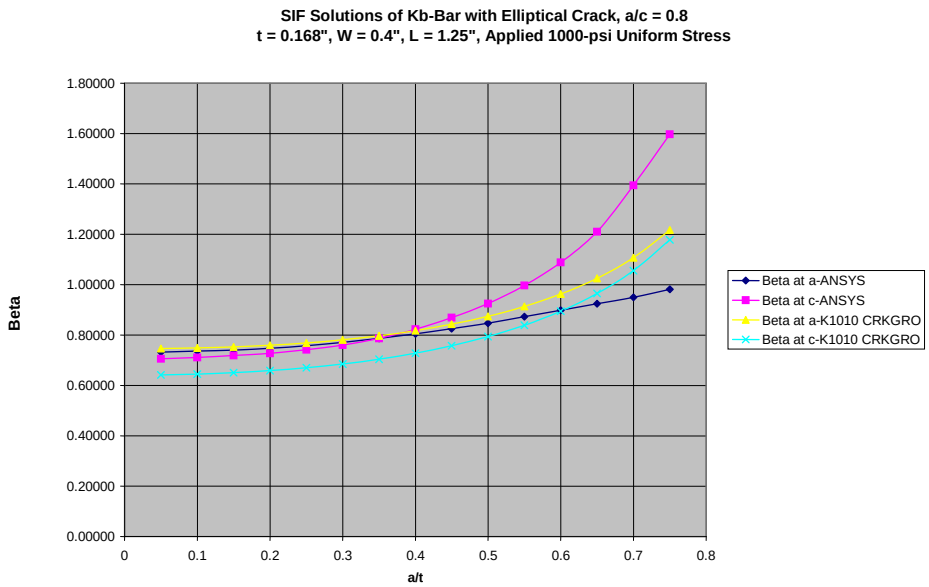

Figure 57. β vs *a*/*t* for Kb-Bar of a Semielliptical Crack With *a*/*c* = 0.8

The boundary and loading conditions used for the FE solution can influence the analysis results, especially when the crack size grows. The plots shown in figures 56 and 57 are the results of the FEA using a load-controlled boundary condition in which a uniform axial stress is applied at one end with the other end fixed. The FEA with a displacement-controlled boundary condition would better reflect the test condition. During the test, the specimen was held firmly to allow axial extension or compression only when a tensile load or compressive load is applied. The plot shown in figure 58 is the displacement-controlled SIF solution of a Kb-Bar with a semicircular crack. By comparing this plot with figure 56 for the same Kb-Bar, one can see that the difference between the load-controlled solution and displacement-controlled solution is not very pronounced at the crack depth, *a*, while the difference at the crack surface, *c*, is more visible. The load-controlled solution at the surface tends to have a higher SIF than the displacement-controlled solution. This is because the load-controlled boundary condition tends to have more action on opening up the crack face due to the secondary bending moment caused by stiffness distribution shifts.

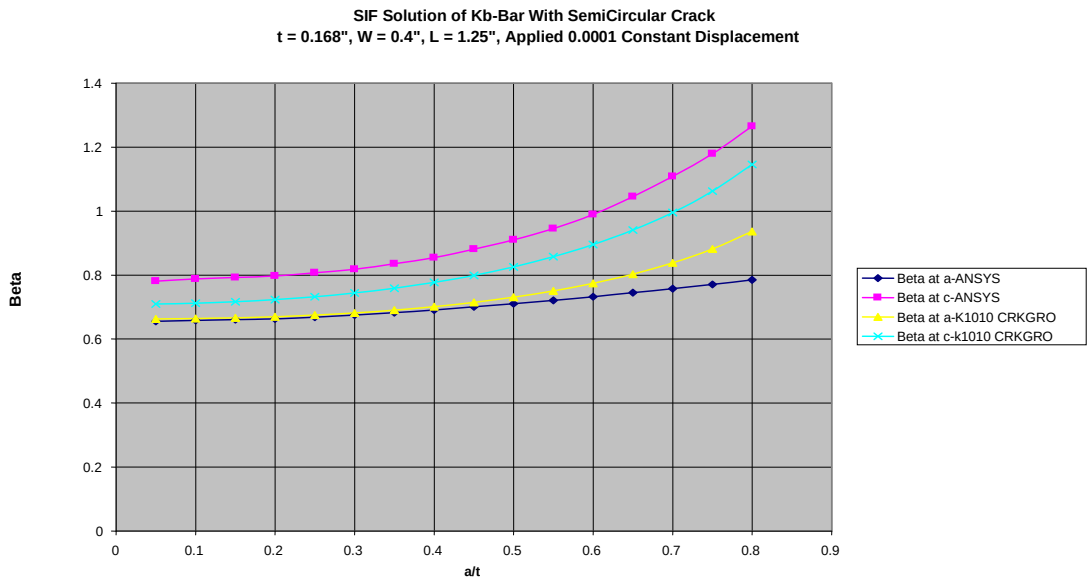

Figure 58. A Semicircular Crack Displacement-Controlled SIF Solution of a Kb-Bar

3.2.1.3 The ANSYS SIF Solutions of Kb-Bar With Residual Stress.

Other macros were developed to calculate the SIF solutions for Kb-Bar with residual stress imposed on the subsurface to evaluate ANSYS's capability to handle residual stress induced by the surface treatment. The macros were also intended to help understand how residual stress would affect crack growth.

It is well known that compressive residual stress in the subsurface of a mechanical component can retard the growth of a surface crack. The extent of crack growth retardation depends on the magnitude of the compressive stress near the surface and its distribution and depth under the surface. A profile of residual stress distribution was taken from a Kb-Bar sample using x-ray diffraction. This stress distribution was imposed to the subsurface element of the Kb-Bar FE model. Since the distribution was very shallow, it was necessary to model this region with very fine elements to capture the true distribution.

A nonlinear solution procedure was required in which contact elements are implemented on the crack faces to prevent them from crossing each other, which may otherwise be caused by compressive residual stress. Compared to a linear solution, the nonlinear solution increased solution time drastically and therefore may hinder future CGA using this technique. CGA required the evaluation of numerous crack sizes as well as iterative calculations for each crack increment. Solution time of this type of nonlinear analysis is governed by the stiffness assumed to the contact elements and the convergence criteria. Different settings of these two parameters were studied to optimize the solution accuracy and the computer turnaround time. Figure 59 shows the residual stress distribution used for the analysis.

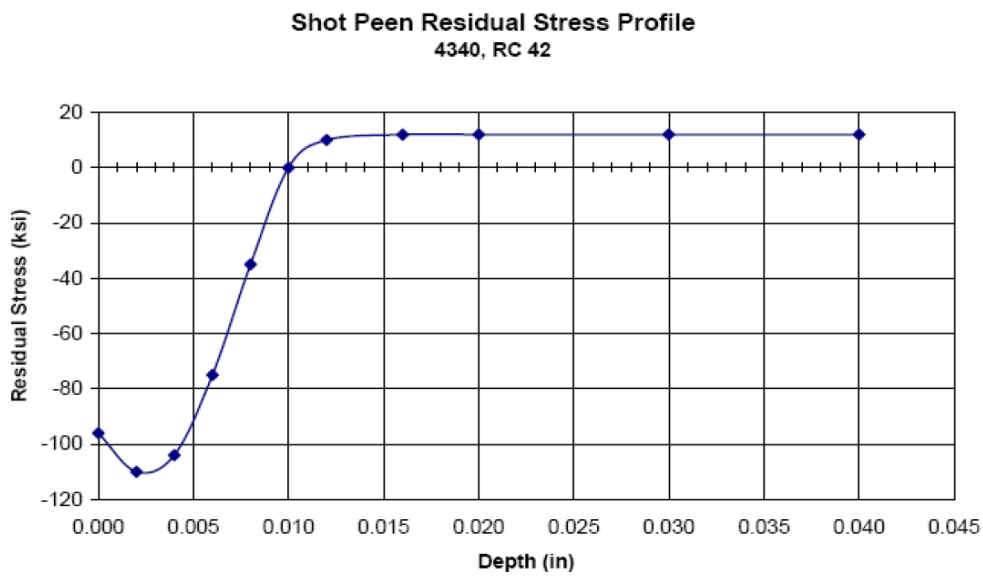

Figure 59. Residual Stress Distribution Used for Analysis

Figure 60 shows the K_I distribution along a semielliptical crack (a = 0.050 and c = 0.063) front embedded in a Kb-Bar with imposed residual stress only.

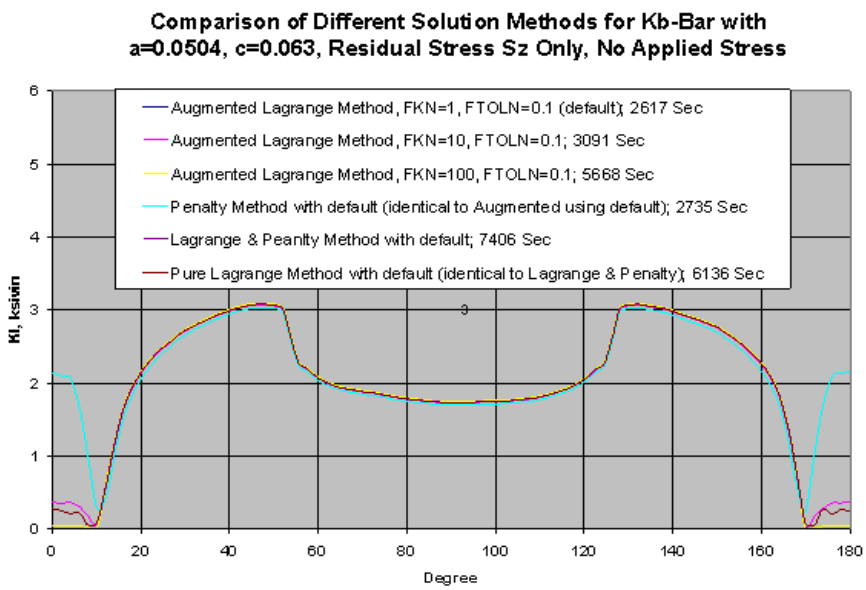

Figure 60. The K_I Distribution Along a Semielliptical Crack Front Embedded in a Kb-Bar With Imposed Residual Stress (a = 0.050 and c = 0.063)

Note that the residual stress turns from compression to tension at the depth of 0.010″ (figure 59). The correspondence in SIF, K_I, distribution is shown in figure 60 at approximately 10° (depth of 0.010″) of each end of the crack front are the kinking point of K_I distribution. Solution times of different contact element stiffness (FKN) are shown in the legend. Except in the compressive residual stress zone, all curves coincide in the tension zone disregarding the stiffness of contact

elements. While the solution with FKN = 100 (yellow curve) appears to be accurate, it took a considerable amount of time to solve. Nevertheless, the other solutions with lower contact element stiffness are questionable on the inflecting part of the curve near the surface. They should all be zero in the compressive layer as the yellow curve appears. With this understanding, however, the solution can still be used with lower stiffness for quicker computer turnaround time by simply assuming that the SIFs in the inflecting curve region are zero.

Figure 61 shows the SIF solutions of a Kb-Bar with the same crack shape and size as the study case presented in figure 60, but with applied stresses added.

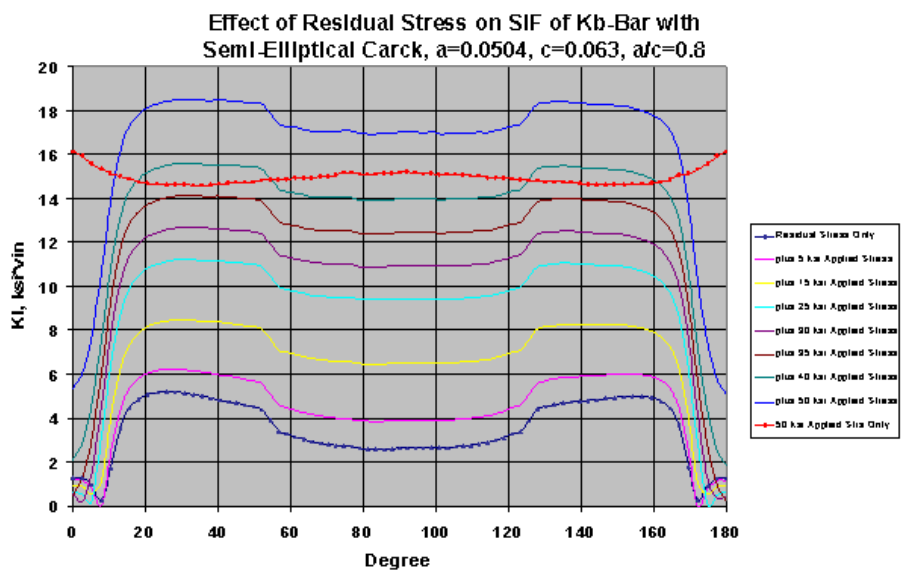

Figure 61. The SIF Solutions of a Kb-Bar With a Semielliptical Crack Under Applied Stresses (a = 0.050 and c = 0.063)

The red-dotted curve shows the SIFs of Kb-Bar with 50-ksi applied stress only. The blue-dotted curve is the SIF with residual stress only. The other curves (smooth lines) are for applied stress, ranging from 5 to 50 ksi with residual stress added. The dark-blue curve (50-ksi applied stress and residual stress) and the red-dotted curve (50-ksi without residual stress) can be used to illustrate the benefit of the residual stress.

3.2.2 The ANSYS FCG Analysis of Kb-Bar.

With the automated SIF solution of the Kb-Bar specimen established, a numerical procedure to conduct FCG analysis was further developed to predict crack propagation of Kb-Bar with normal load and load cycles applied. In this case study, the crack may be assumed to have an initial semicircular or semielliptical shape. The assumed initial shape, however, may not necessarily be maintained during the course of crack propagation because the a-tip and c-tip may grow at different rates, depending on the load applied and material properties. The required inputs for the analysis are material data and $da/dN \sim \Delta K$ data obtained from the M(T) tests. Figure 62 shows the flow chart of this CGA procedure.

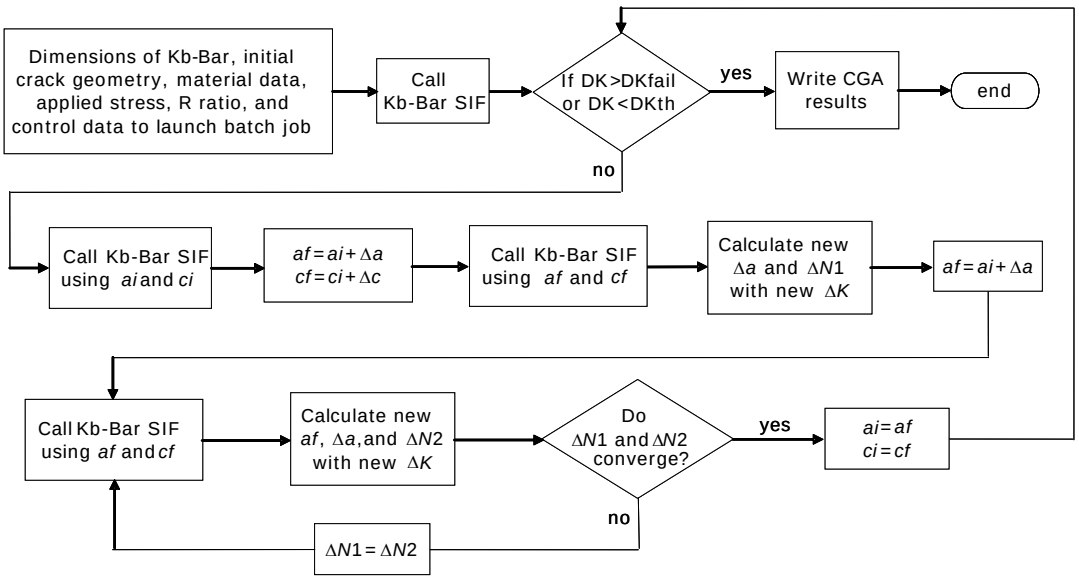

Figure 62. Flow Chart of Kb-Bar's CGA

The following is a typical command file to run an ANSYS batch job to perform CGA:

```
/BATCH
/NERR, 0, 99999999
L=1.25        ! Length of model for KbBar
W=0.4                ! Width
t=0.168              ! Thickness
pi=3.1415926536
!  Material data from M(T) coupon tests
!             R = 0.05
DKth=4.58         ! Threshold delta K, ksi*in^0.5
DKfail=11.47  ! DK into failure zone, CGA stops
cp=3.2409E-11 ! Constant C of Paris equation
mp=4.2369            ! Exponent m of Paris equation
mm=(2-mp)/2          ! Constant of crack growth integration
!
!  Applied stress
!
sigmax=34707  ! Applied max stress, psi
sigmax=sigmax/1000 ! Convert into ksi
RR=0.05              ! min/max stress ratio
delsig=(1-RR)*sigmax       ! delta sigma in ksi
!
!  Initial crack geomerty
!
ai=0.01              ! Initial crack depth, a, and a/c ratio, ro
ro=1.0        ! Initial a/c ratio
ci=ai/ro             ! Initial crack semi-width
dela=0.005           ! Crack growth this step
delc=dela
NCGA=20              ! Number of crack growth analysis steps
cvg=0.05             ! Convergence criterion
!
KbBarCGA             ! Call macro to perform CGA
!
FINISH
/EXIT,NOSAVE
```

With the implemented macros, the crack propagation of a semicircular surface crack with a crack depth of 0.010″ on a Kb-Bar was predicted. The maximum applied tensile stress was 34.707 ksi with a stress ratio of 0.05. The example results are shown in figures 63 and 64.

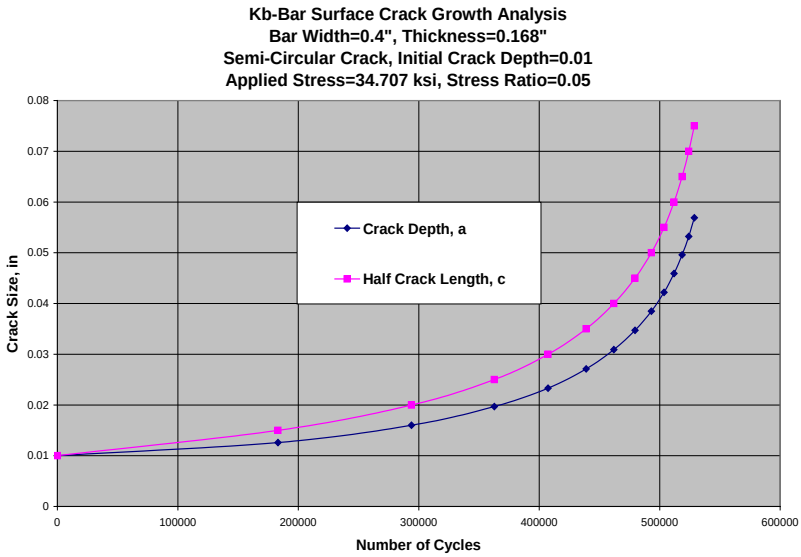

Figure 63. The *a*-N Curves of a Kb-Bar CGA Using ANSYS

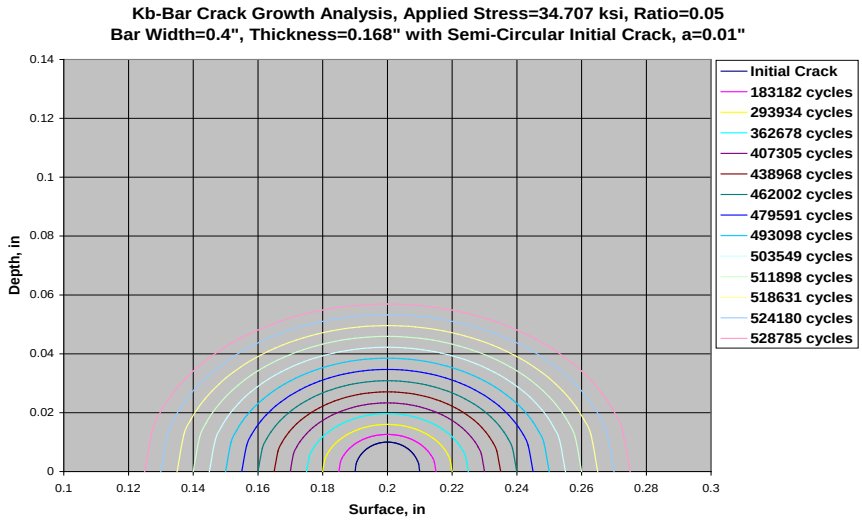

Figure 64. Crack Growing From Kb-Bar CGA Using ANSYS

Note that the approach used above is a numerical method. Unlike the commonly used CGA approach that already has SIF solution through a separate program and performs FCG analysis in a CGA platform, this method takes advantage of ANSYS stress analysis to comprise both SIF calculation and CGA for each extension of the crack. From this viewpoint, ANSYS indeed reveals good potential for practical application in RCDT design of rotorcraft drive system components.

The abovementioned analysis is linearly elastic without considering the plastic deformation left behind on the crack flanks as the crack propagates. Further investigation revealed that the effect of plasticity plays a very important role in the analysis of crack growth cycles for a Δa. In essence, the plastic deformation on the crack flanks makes the crack close earlier before reaching minimum load during the unloading step. This phenomenon, called crack closure effect, changes the actual stress ratio and, thus, effective ΔK. Therefore, the linearly elastic analysis would be much more conservative, especially at overloads and/or low stress ratio.

To account for the crack closure effect, the effective ΔK_{eff} was computed by incorporating Elber's equation [8].

FCG analyses were performed, and the results were compared with test data. Figures 65 through 67 show the ANSYS CGA results with the crack closure effect considered and comparison to the test data for a Kb-Bar with R = 0.05.

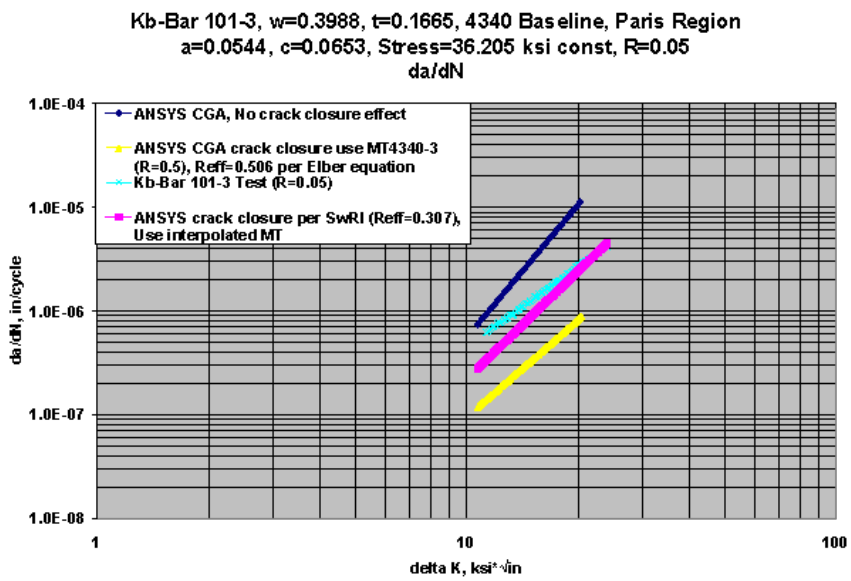

Figure 65. ANSYS Kb-Bar *da*/*dN* With the Crack Closure Effect Considered, Using Elber's Equation and SwRI *f*-Value, Compared to the Test Data for a Kb-Bar With R = 0.05

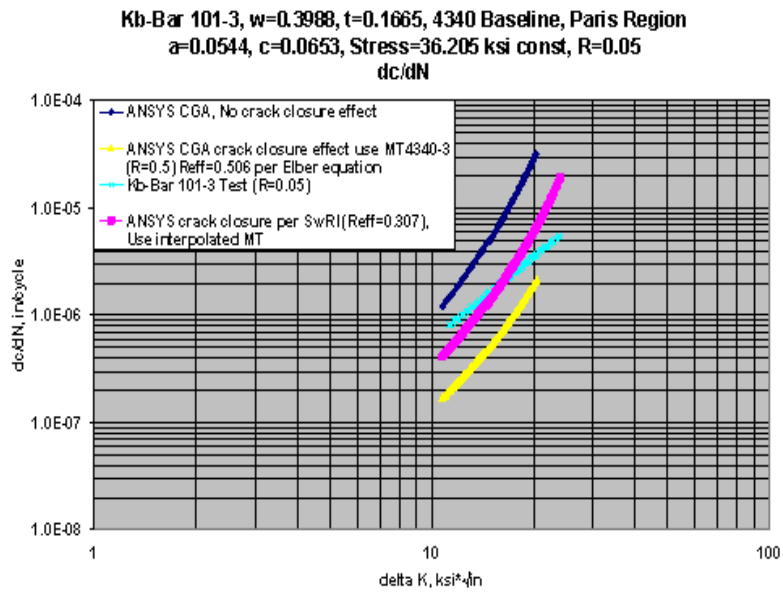

Figure 66. ANSYS Kb-Bar *dc*/*dN* With the Crack Closure Effect Considered, Using Elber's Equation and SwRI *f*-Value, Compared to the Test Data for a Kb-Bar With R = 0.05

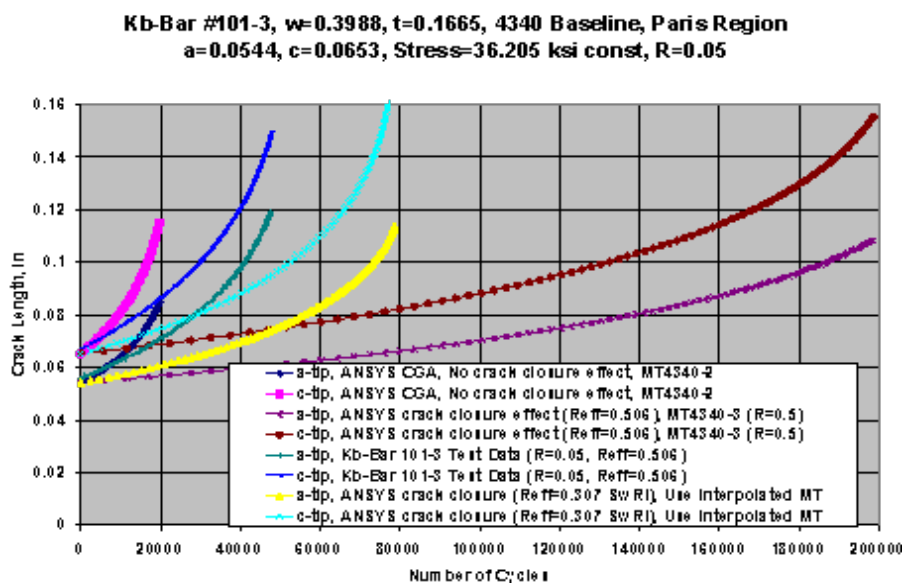

Figure 67. ANSYS Kb-Bar *a*-N Curves With the Crack Closure Effect Considered, Using Elber's Equation and SwRI *f*-Value, Compared to the Test Data for a Kb-Bar With R = 0.05

Figures 68 through 70 show the CGA results and comparison with test data for R = 0.8. It appears that the ANSYS FCG analyses using Elber's equation for crack closure effect correlate favorably to test data for higher stress ratios, say R = 0.8. This was expected since, at R = 0.8, the crack remains open even at the minimum load.

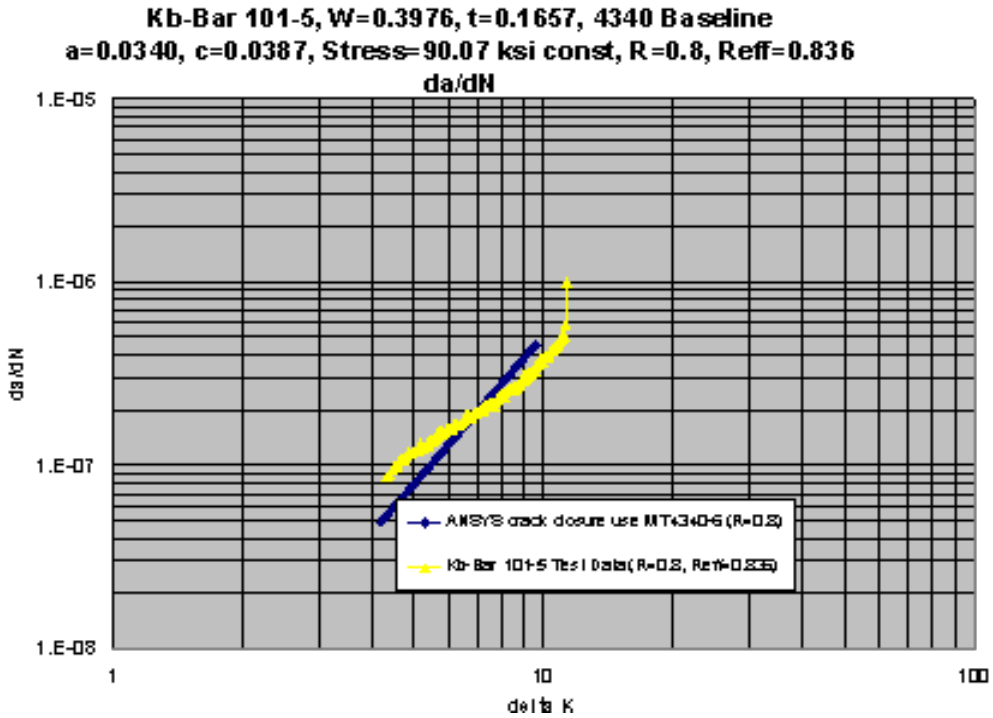

Figure 68. ANSYS Kb-Bar *da*/*dN* With the Crack Closure Effect Considered, Using Elber's Equation and SwRI *f*-Value, Compared to the Test Data for a Kb-Bar With R = 0.8

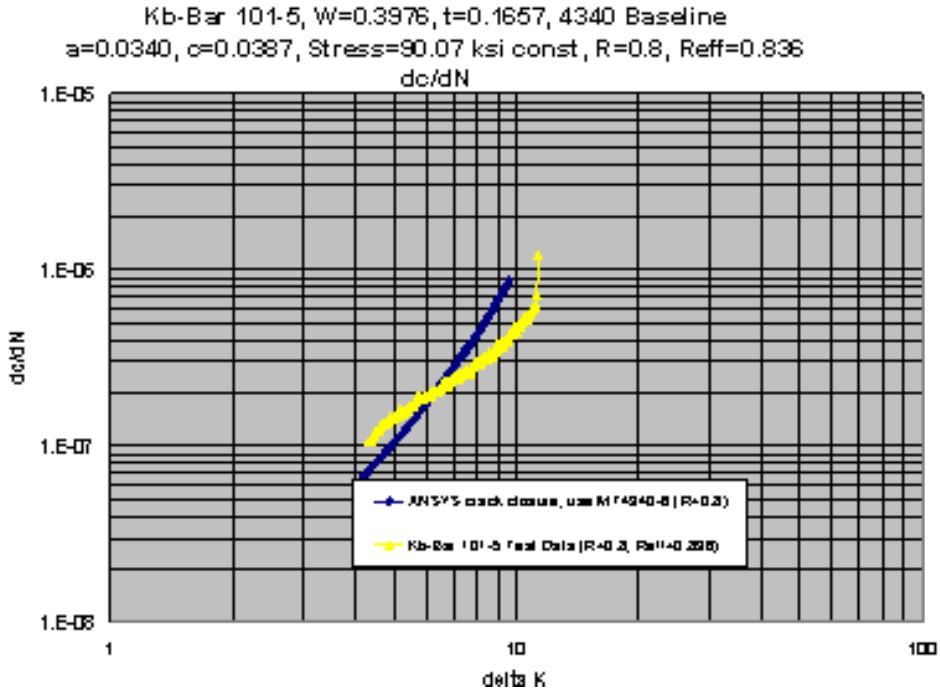

Figure 69. ANSYS Kb-Bar *dc*/*dN* With the Crack Closure Effect Considered, Using Elber's Equation and SwRI *f*-Value, Compared to the Test Data for a Kb-Bar With R = 0.8

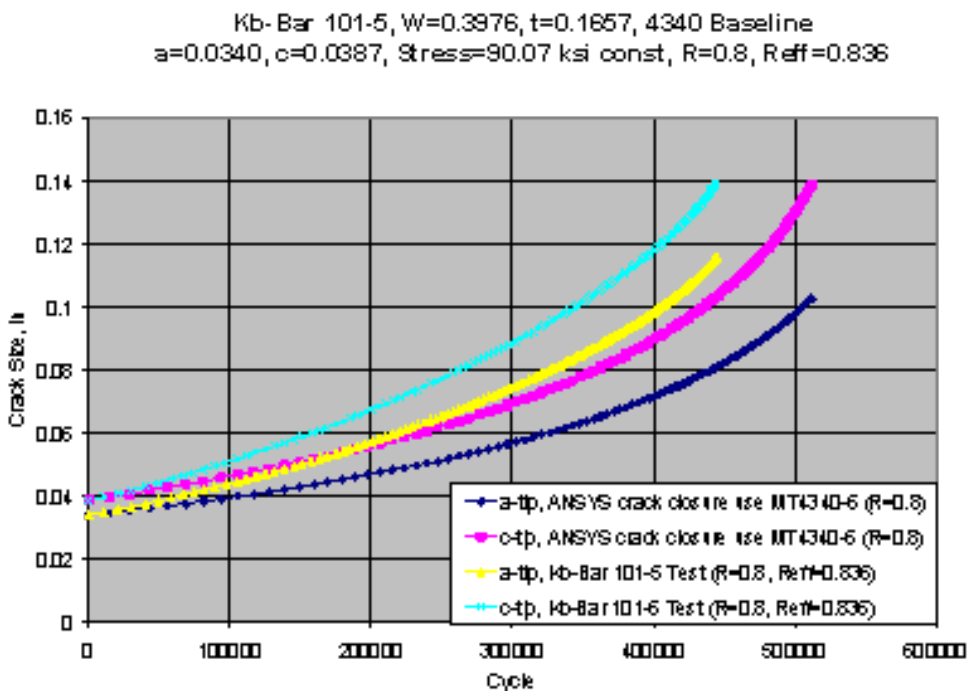

Figure 70. ANSYS Kb-Bar *a*-N Curves With the Crack Closure Effect Considered, Compared to the Test Data With R = 0.8

3.2.3 Modeling of Fillet Radius Subelement With ANSYS Workbench™.

The ANSYS CGA potential was further evaluated with the test element specimen configuration. FE modeling of the fillet radius element design was performed with ANSYS Workbench v12 analysis framework. Several designs of the fillet radius element were analyzed to determine the optimal compromises in geometry and test setup. Figure 71 shows the final design of the fillet radius element, excluding the modification for flats at the restraint end.

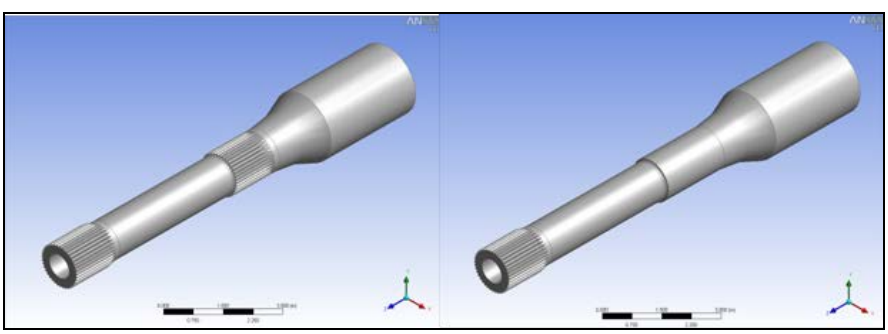

Figure 71. Solid Model Geometry of the Fillet Radius Element Shown With Spline in Crack Region (left) and Without (right)

The solid geometry model of the fillet radius element was created within the ANSYS DesignModeler™ using nominal dimensions. The spline was included at the location of applied loads and optionally at the crack region, depending on the test specimen.

The solid model geometry in the ANSYS DesignModeler was then transferred to ANSYS Mechanical™, and an FE mesh was created using, predominantly, 20-node hexahedron elements. The mesh in the fillet radius area was refined to have improved accuracy to define the maximum principal stress magnitude, position, and orientation, as shown in figure 72. The element size in the 0.1-in. fillet radius was 0.003 in. along the radius with 100 divisions along the shaft circumference.

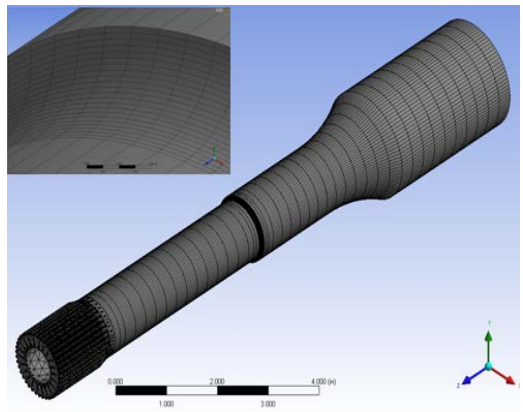

Figure 72. An FE Mesh of the Fillet Radius Element Without Spline in Crack Region (inset shows fillet radius)

The boundary conditions of the fillet radius element were defined within ANSYS Mechanical and include a fixed constraint applied at the large diameter end with torque and shear applied to center of the spline at the opposite end, figure 73. The material constants were for structural steel with linear isotropic elasticity properties of 29 Msi for Young's modulus and 0.3 for Poisson's ratio.

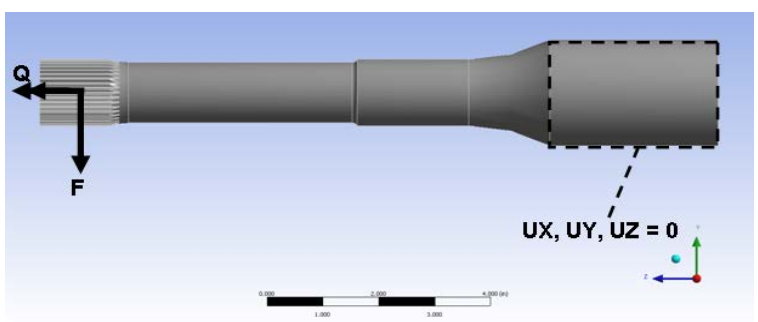

Figure 73. Boundary Conditions of the Fillet Radius Element

The maximum principal stress (S_1) occurred at the 0.1-in. fillet radius in both combined loading conditions: bending equal to torsion and bending equal to twice the torsion. The S_1 contours for both conditions are similar and are depicted in figures 74 and 75 for the bending is equal to torsion case.

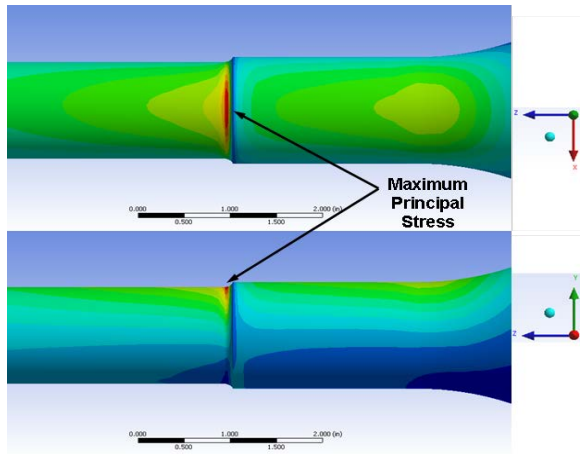

Figure 74. Fillet Radius Element Principal Stress (S_1) Contours for the Bending Equal to the Torsion Load Condition

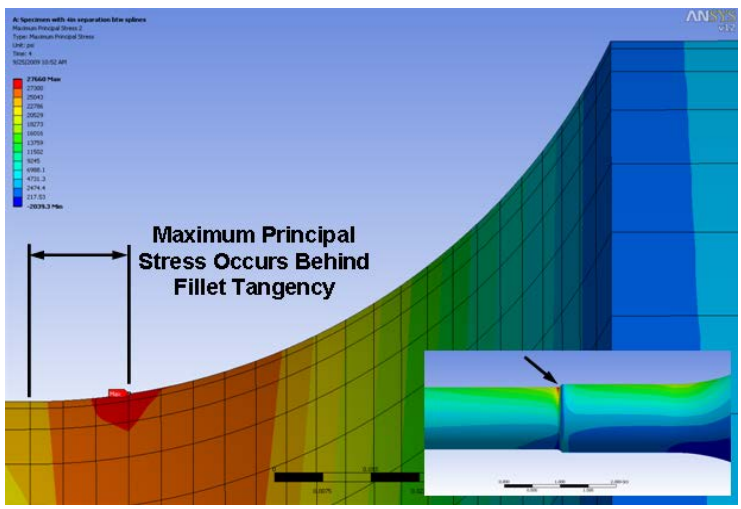

Figure 75. Fillet Radius Element Principal Stress (S_1) Contours at the Fillet Radius for the Bending Equal to Twice the Torsion Load Condition

The location and orientation of the maximum principal stress vector were extracted from the FE solution. The linear relationship between the applied load and resulting stress was used to determine the required test loads for generating the desired stress magnitude at the crack location. These results are summarized in sections 2.4.1 and 3.1.3.

3.2.4 ANSYS SIF Solutions for Crack at Fillet Radius Element Specimen.

The SIF solutions for a crack embedded in the fillet radius element were generated using ANSYS for both the baseline and shot-peened conditions. Crack geometry was created from slicing the existing solid model geometry, or global model, at the desired location and orientation, as shown in figure 76. The crack front was assumed to remain planar and elliptical with *a*, the radius along the depth, and *c*, the width at the surface.

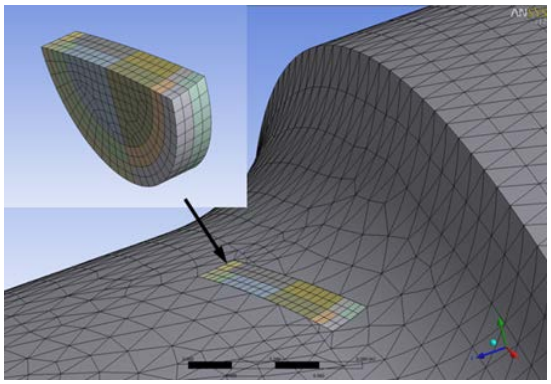

Figure 76. Typical FE Mesh for the Fillet Radius Surface Crack, Excluding Residual Stress Effects

The FE mesh of 20-node hexahedron elements along the crack front were modified to create singular elements with their mid-side nodes relocated to the quarter position. The nodes on the crack surface, but not along the crack front, were duplicated and then merged to the elements on one side of the crack, dividing the mesh into two coincident crack surfaces. Figure 77 shows the crack front SIF results with the crack plane orientated in 0°, 15°, 30°, and 45°.

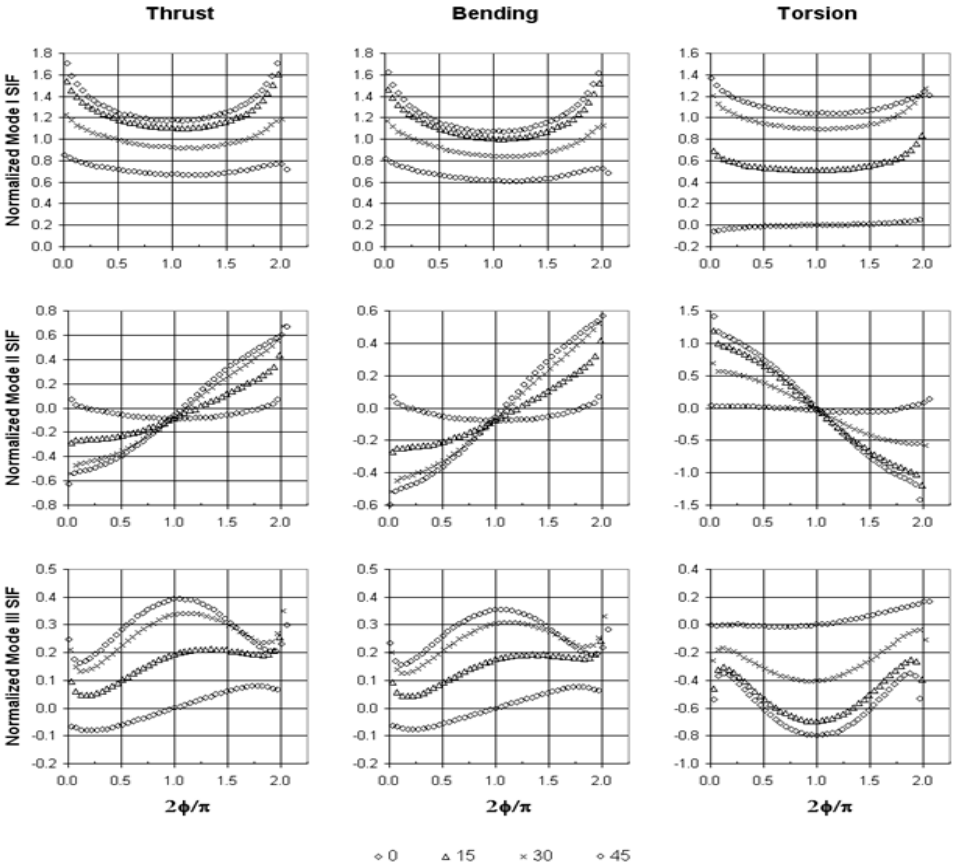

Figure 77. The SIF Solutions for the Fillet Radius Surface Crack Under Thrust, Bending, and Torsion (crack plane orientation: 0°, 15°, 30°, and 45°)

Another region was sliced from the global model to define shot-peening residual stress. Significant mesh refinement through the depth, as shown in figure 78, was necessary for this region surrounding the crack, but not for the remainder of the geometry, thus reducing the penalty on the solution time.

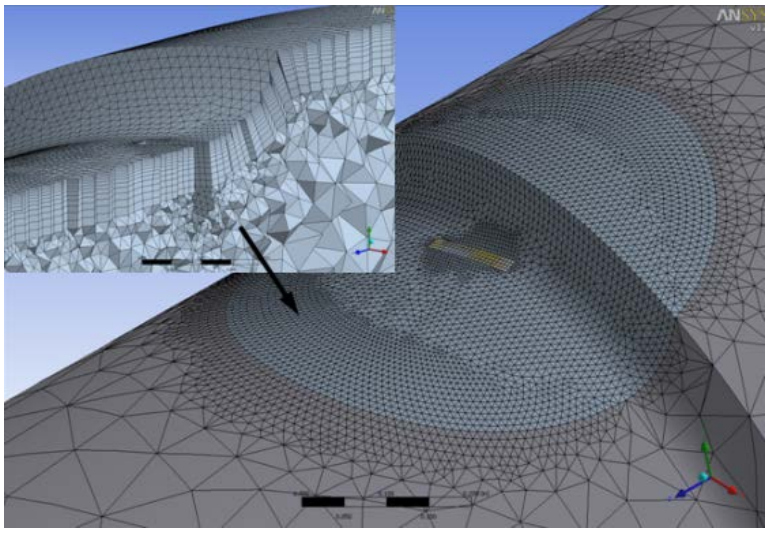

Figure 78. Local Refinement of the FE Mesh for the Fillet Radius Surface Crack, Including Residual Stress Effects

Linear elastic material properties were assigned to the entire geometry. Nonlinear contact on the crack face was neglected for the models without residual stress since the applied loads act to open the crack. However, nonlinear contact was necessary for the models with residual stress to capture the effect of compression on the crack faces, which significantly increased solution time. Residual stress was applied to the model using the INISTATE command to define the initial state of stress in each element as a function of depth. The relationship between the residual stress and depth was derived from polynomial curve fits of the data in figure 60 for a typical shot-peening residual stress profile of 4340 steel up to a depth of 0.040 in. The residual stresses were included only in the region near the crack due to the required mesh density. The SIF results shown in figures 79 through 82 are for the fillet radius surface crack with $a = c = 0.050$ in. at the 1.136-in.-diameter section of the 2.000 in. length, with residual stress included. Four crack plane orientations were considered: 0°, 15°, 30°, and 45°, each having three loads applied individually at four residual stress levels: 0, 5, -20, 35, and 50 ksi.

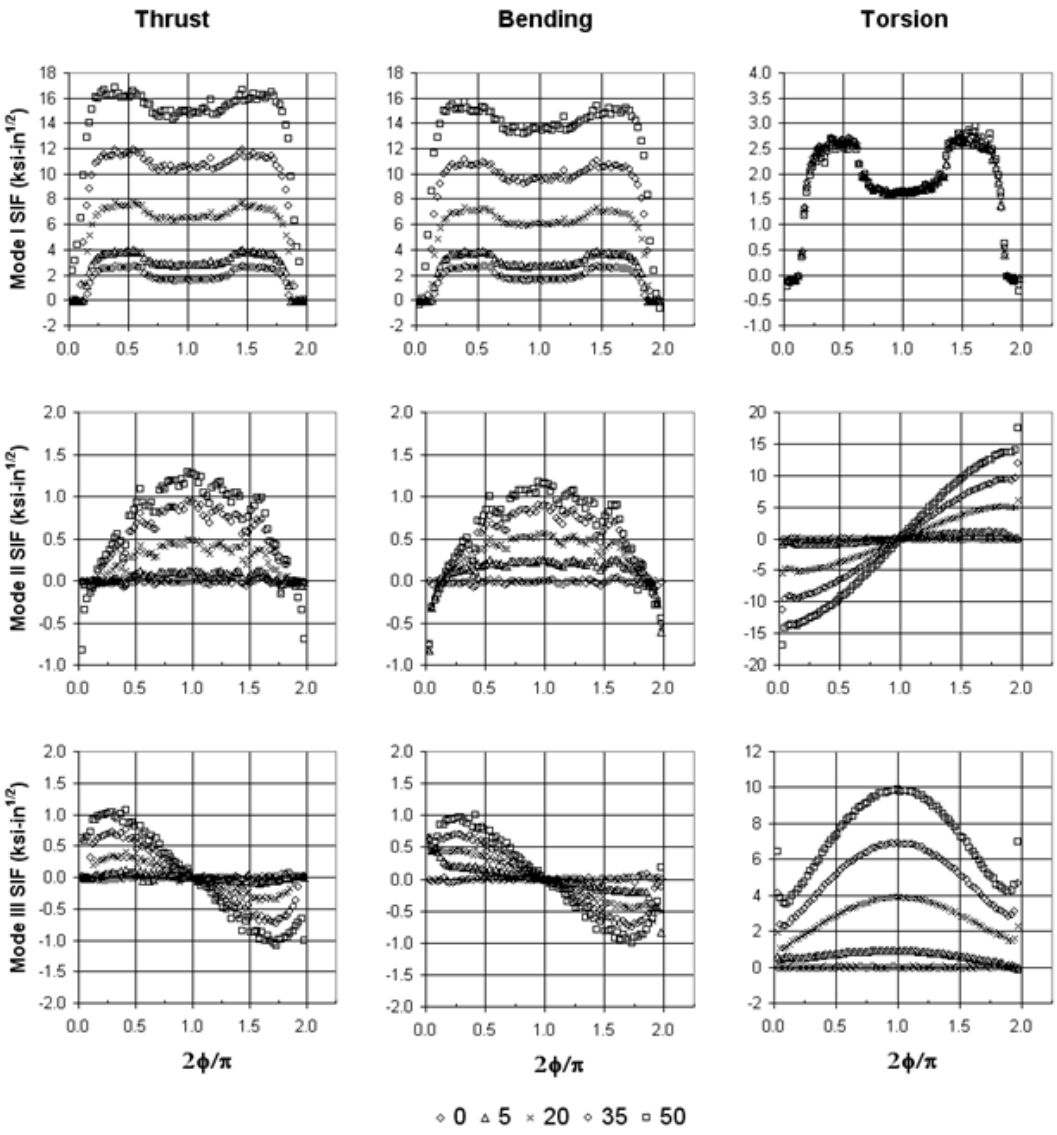

Figure 79. The SIF Solutions for the Fillet Radius Surface Crack Oriented at 0° Under 0-, 5-, 20-, 35-, and 50-ksi Thrust, Bending, and Torsion, Including Residual Stress

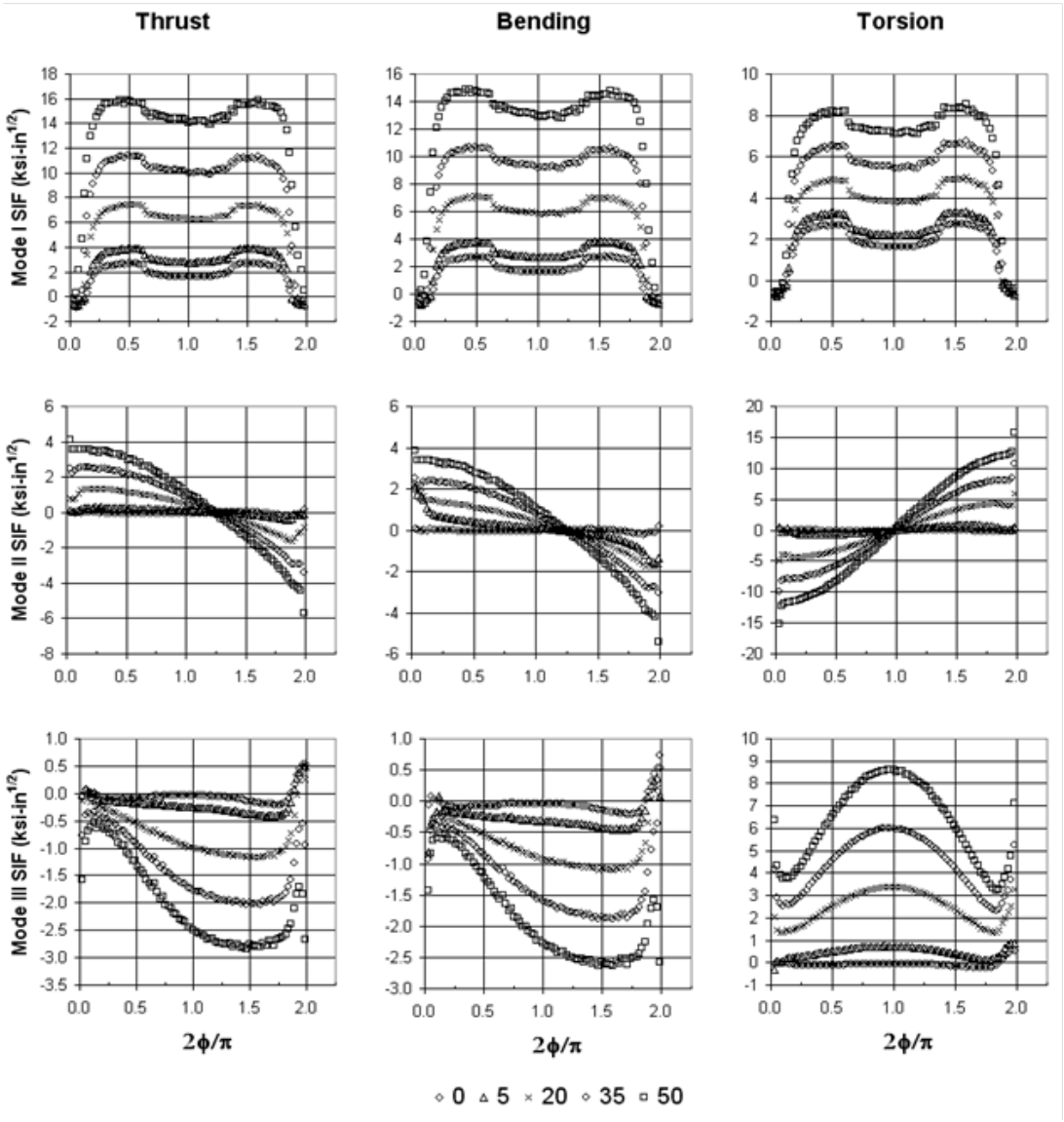

Figure 80. The SIF Solutions for the Fillet Radius Surface Crack Oriented at 15° Under 0-, 5-, 20-, 35-, and 50-ksi Thrust, Bending, and Torsion, Including Residual Stress

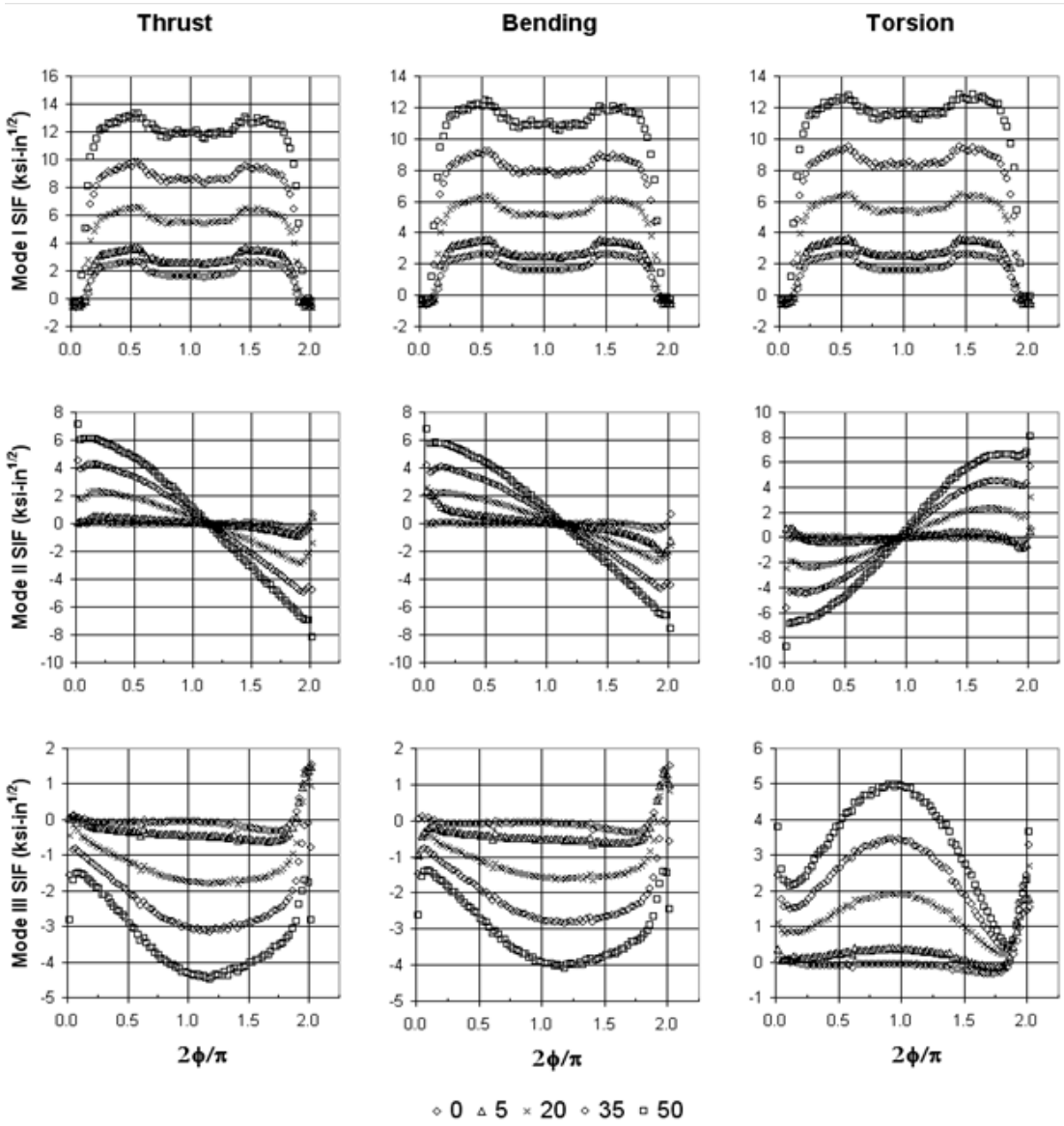

Figure 81. The SIF Solutions for the Fillet Radius Surface Crack Oriented at 30° Under 0-, 5-, 20-, 35-, and 50-ksi Thrust, Bending, and Torsion, Including Residual Stress

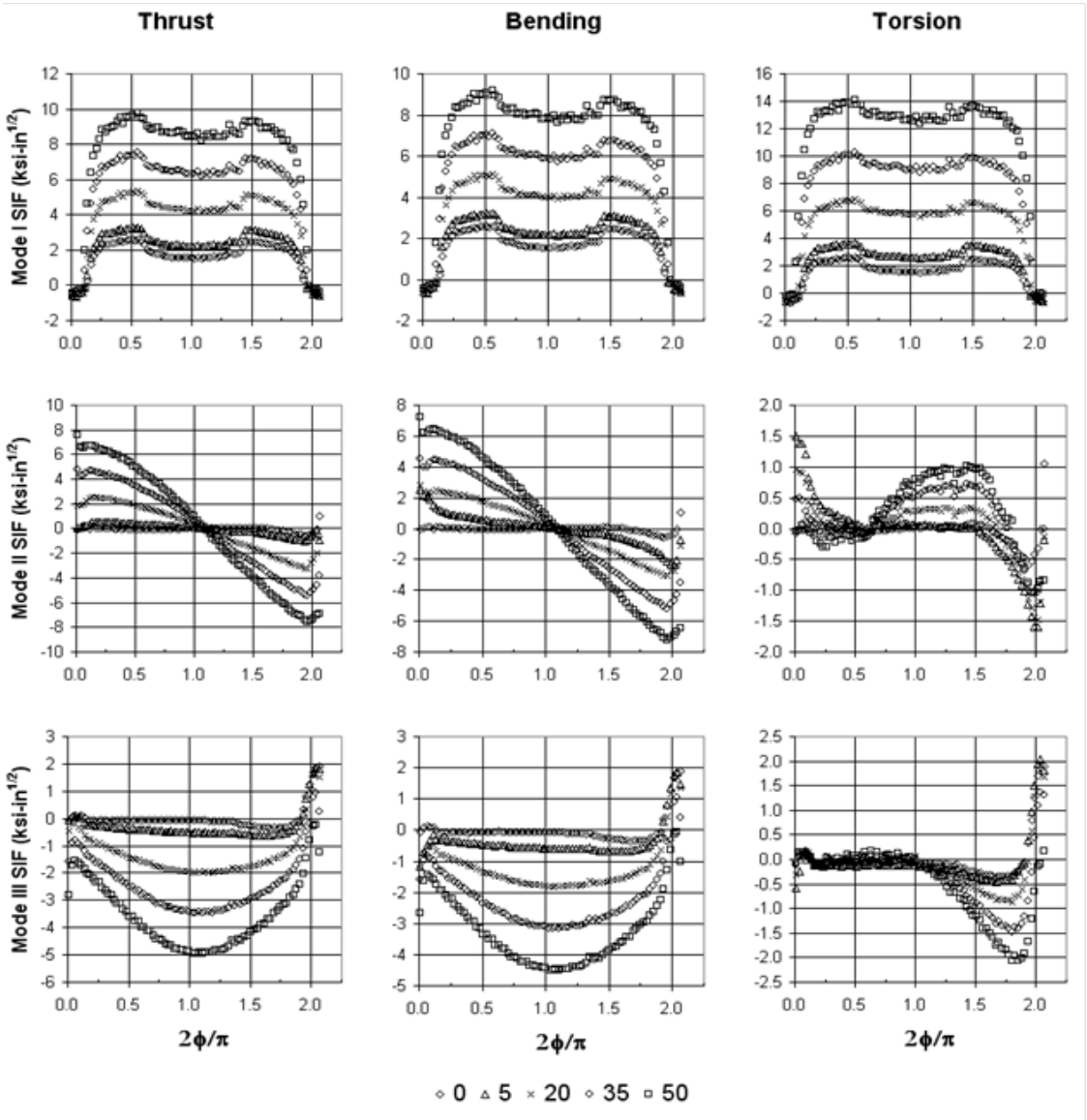

Figure 82. The SIF Solutions for the Fillet Radius Surface Crack Oriented at 45° Under 0-, 5-, 20-, 35-, and 50-ksi Thrust, Bending, and Torsion, Including Residual Stress

3.2.5 ANSYS FCG Analysis for Fillet Radius Element Specimen.

The methodology for analyzing crack growth in the fillet radius element using ANSYS was developed and demonstrated for the baseline condition without residual stress. Although parametrically defined within ANSYS Workbench, the FE model used to calculate SIF solutions could not be completely automated for FCG analysis as it was performed with the Kb-Bar ANSYS FCG analysis. During the course of crack extension, the update of the crack shape required some amount of user intervention to create the desired FE mesh, i.e., adding or removing virtual topology to the geometry and confirming the selection of crack surface and crack front nodes for preprocessing. One example is when crack sizes intersect new surfaces of

the element specimen, such as crossing over the fillet tangency or the edge adjoining the larger diameter section.

Figure 83 shows a study case of evaluating ANSYS FCG analysis's potential. For this study, the fillet element design with a 4.000-in.-long and 1.136-in.-diameter section was analyzed. The crack tips on the surface were defined as $^{+}$c and $^{-}$c; and the crack depth was defined as *a*.

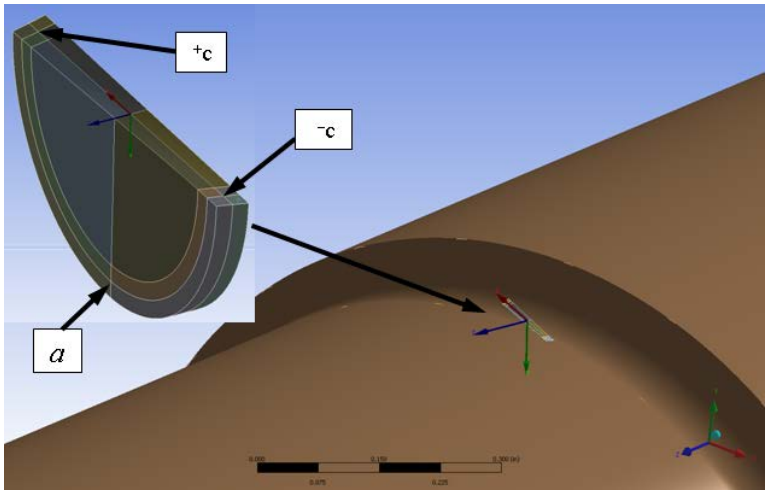

Figure 83. Definition of Crack Local Coordinate System

The study revealed that to perform a CGA of the fillet radius element specimen or any 3D geometry using ANSYS Workbench, the user could either manually generate the SIF solution at each iteration of crack growth or accumulate SIF solutions for several combinations of crack depth and shape to develop a response surface (RS). During the CGA, SIF solutions can be interpolated from the RS rather than repeating the entire FE solution. The RS methodology was demonstrated in the example shown in figure 84.

Once all the SIF solutions were generated, the FCG analysis could be independent of ANSYS. MATLAB® was then used to evaluate the crack growth iterations. The mode I SIF RSs at locations ^{+}c, *a*, and ^{-}c were calculated for two combinations of loads: (1) bending equal to torsion and (2) bending equal to twice torsion. Each surface depth varied from 0.015 to 0.220 in. and the *a*/*c* ratio varied from 0.5 to 1.2 in. The crack was assumed to remain planar, at a fixed location and at a constant orientation, i.e., aligned with the maximum principal stress vector of a flawless specimen. The crack orientations for both combinations of load are given in figure 16. The M(T) Paris region *da*/*dN* data were used for the FCG analysis, shown in figure 85. The applied stress was 55 ksi with a stress ratio of 0.05 for this example.

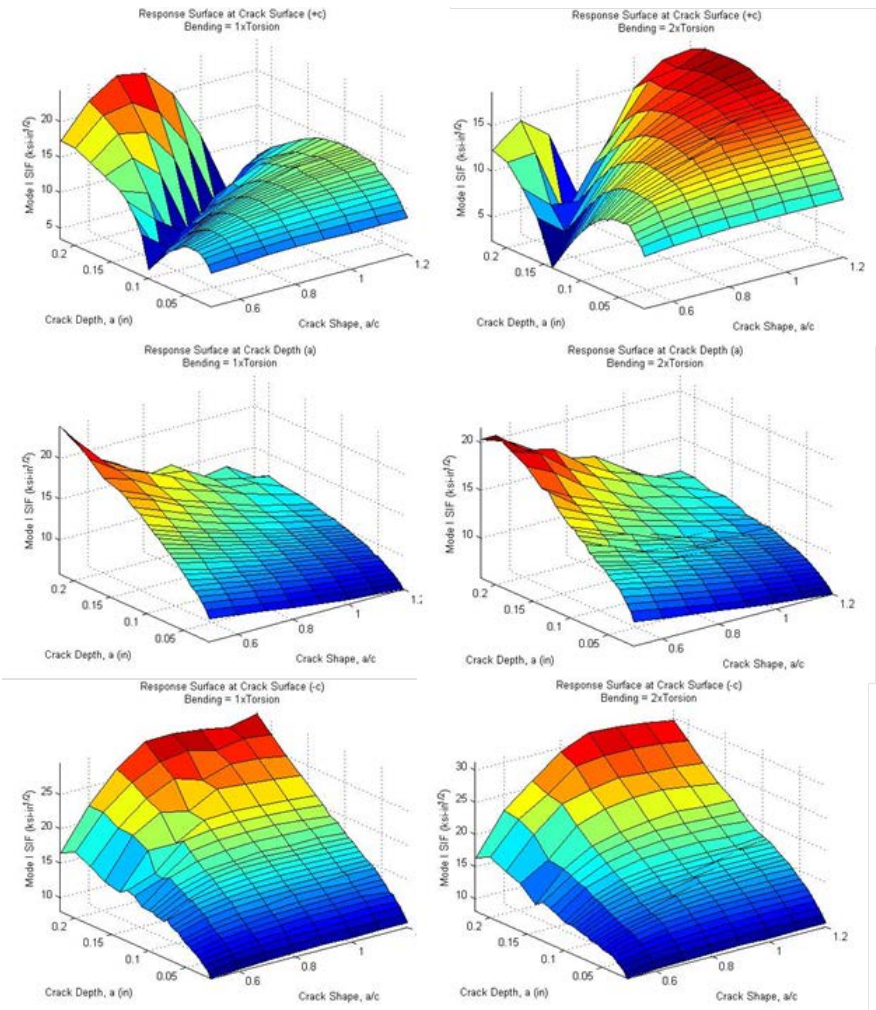

Figure 84. The K_I RSs for Fillet Radius Surface Crack

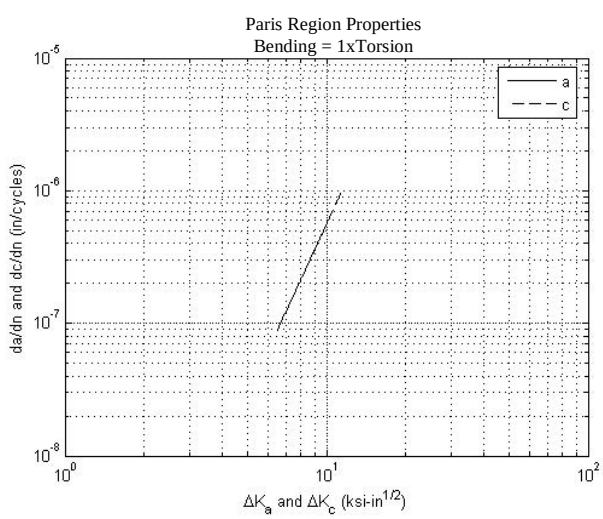

Figure 85. Paris Region Properties Used in the CGA
(same for both loading conditions)

Simulated crack growth as a function of cycles, shown in figure 86, may be compared with the fillet element data in figures 19 through 22.

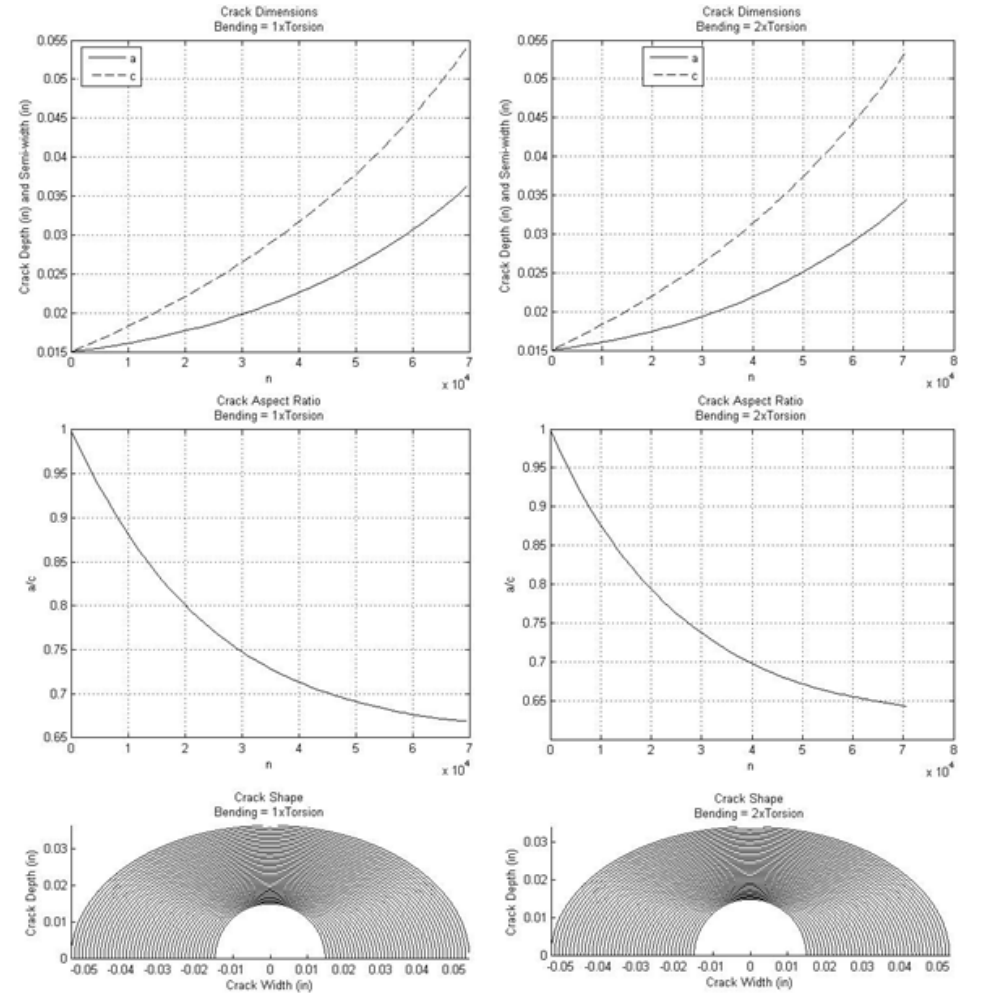

Figure 86. The CGA of the Fillet Radius Surface Crack With Two Loading Conditions and an Initial Flaw Size of $a = c = 0.015''$

The ANSYS crack growth simulation of the element test was promising, yielding conservative results. The conservatism could be lowered by refining the crack growth algorithm and extending the *da*/*dN* material data to the full range, rather than assuming Paris region only.

4. EVALUATION OF LIFE ENHANCEMENT METHODS ON ROTOR MAST.

The rotor mast and other drive system components are typically subjected to various surface/heat treatments, such as induction hardening, carburizing, and shot peening, to enhance the performance and fatigue life. These surface treatments create compressive residual stress fields that interact with stresses caused by the external loads. It is expected that the introduction of the compressive residual stresses slows down or suppresses surface cracking within the residual stress zone.

The effects of residual stress on the FCG life of shot-peened and carburized rotor masts were investigated in accordance with the test program. The analytical tool's capability to handle FCG with treatments was evaluated. The Kb-Bar surface crack configuration was tested and analyzed with the baseline, shot-peening, and carburizing conditions. The shot-peened fillet radius element specimens of a surface crack were tested to investigate the FCG behavior in comparison with the baseline element specimens.

Kb-Bar testing was one of the two coupon-level tests of the program. Kb-Bar testing is usually used to characterize FCG behavior of a surface crack. A surface crack grows in the plane and the direction perpendicular to the maximum opening stress at the crack front. The addition of the compressive residual stress in the surface layer changes the scenario of crack growth in terms of aspect ratio a/c.

4.1 RESIDUAL STRESS OF AS-MACHINED BASELINE Kb-Bar.

For the baseline Kb-Bar specimens, it was commonly assumed that the coupon was residual stress free since its surfaces were free from surface treatments. However, unexpected residual stress was found in the baseline coupons that may be attributed to the sensitivity of 4340 and 9310 steels to the machining and handling process.

Unlike commonly handled aluminum and titanium Kb-Bar specimens or 4340 and 9310 "large" steel parts (relative to the Kb-Bar geometry), 4340 and 9310 steel Kb-Bar specimens were sensitive to the machining process. The procedure and handling specifications that were applied to aluminum, titanium, and other alloys did not apply well to these two materials. For the first of the carburized coupons, coupon distortion was observed, which required a lot of effort to develop a mitigating action. Sensitivity of 4340 and 9310 steels to the machining process also indicated a finer cut was needed for each machining pass.

Mitigating action was taken by applying a stress relief process. An attempt was made to remove the residual stress completely for the baseline coupons. An iterating approach was used to evaluate the stress relief procedure. Four iterations were taken, each involving annealing at elevated temperatures for 2 hours. Table 26 lists the residual stress level reduced from as-machined (RS-0) to the status after each process of stress relief (RS-x, where x = 1, 2, 3, and 4). With further stress relief processing, the residual stress might be reduced to a lower level. However, limited by resources, the RS-4 procedure was accepted as a final residual stress relief process with the least residual stress remaining.

Table 26. Average Stress Relief Results for Each Process

Residual Stress Relief Procedure	Residual Stress at RS-0 (ksi)	Residual Stress at RS-x (ksi)
RS-1 (500°-750°F, 2h)	-69.23	-55.69
RS-2 (800°-850°F, 2h)		-32.72
RS-3 (850° ±10°F, 2h)		-26.79
RS-4 (RS-3 + polish)		-10.54

4.2 RESIDUAL STRESS PROFILES.

Residual stresses have been measured as a depth profile and on the surface for the baseline, shot-peening, and carburizing surface conditions. The magnitude of residual stress on the surface of the Kb-Bar test coupons was specifically established for this program.

4.2.1 In-Depth Residual Stress Profiles.

Five Kb-Bar specimens were examined for determining the longitudinal subsurface residual stress distributions. The examined Kb-Bars, identified in table 27, all had nominal dimensions of 0.4-in. gage width and 0.2-in. gage thickness. X-ray diffraction residual stress measurements were taken at the surface and at nominal depths of 2.0, 5.0, 10.0, 15.0, and 30.0 x 10^{-3} in. Measurements were taken in the longitudinal direction in the gage region where the notch was to be induced.

Table 27. Test Matrix for Residual Stress In-Depth

Sample ID	Sample Name	Sample Material
1	Baseline	4340 steel
2	Shot peen	4340 steel
3	Baseline	9310 steel
4	Shot peen	9310 steel
5	Carburized	9310 steel

The residual stress profile (in-depth) is shown in table 28 and figure 87. For the examined depth, the highest compression was measured at the surface of the 9310 steel carburized specimen and was -113.1 ksi. The highest tension was +7.3 ksi, measured 0.015 inch below the surface of the 4340 steel shot-peened specimen.

Table 28. Residual Stress In-Depth of Kb-Bar Test Specimens

Depth (in.)	4340 Steel		9310 Steel		
	Baseline	Shot-Peened	Baseline	Shot-Peened	Carburized
0.000	-33.9	-102	-44.5	-92.8	-113.1
0.002	-1.7	-108.6	-5.4	-93.1	-29.4
0.005	-1.9	3.2	-1.3	-22.2	-29.3
0.010	-1.4	6.8	-1.5	3.8	-32.2
0.015	-0.3	7.3	-4.4	6.3	-21.5
0.030	1.4	5.8	1.4	6.9	4.0

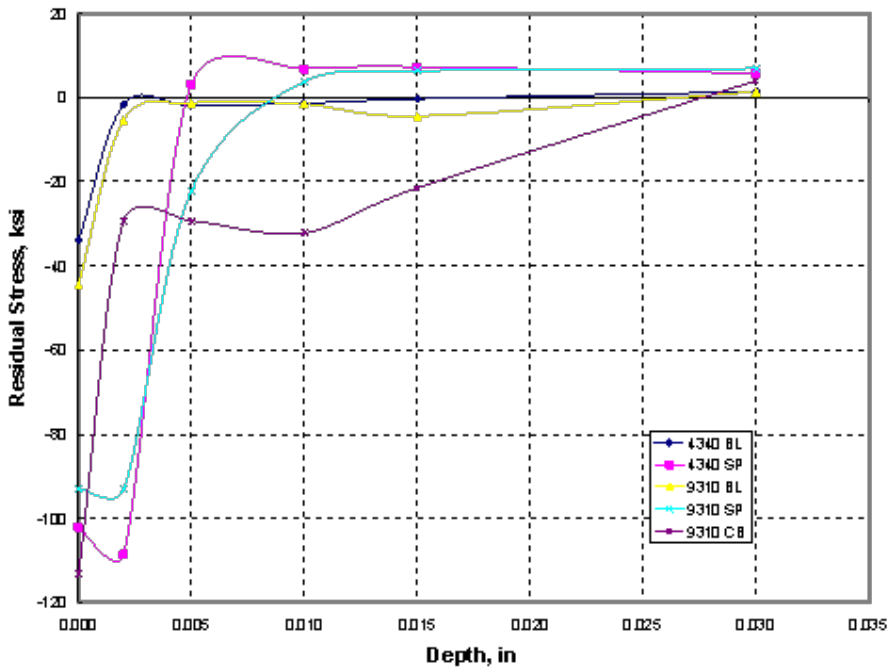

Figure 87. Profiles of Residual Stress In-Depth for 4340 Steel and 9310 Steel Kb-Bars

The details of the x-ray diffraction residual stress examination of the residual stress are shown in appendix D.

4.2.2 Residual Stress on Surfaces.

With the observation of residual stress in the baseline Kb-Bar specimens, the argument arose that a baseline Kb-Bar specimen may not actually be residual stress free. Historically, however, this fact had never been noticed and taken into account in the fracture mechanics test community. With this finding being considered, many test results showed random scatter that can be explained now.

Based on the abovementioned observations and hypothesis on the causes and possibilities of the existence of residual stress, it was necessary to determine and document surface residual stress to

compare the results of specimens with different surface conditions and to be able to correctly interpret the test results. Table 29 is a complete record of the surface residual stress of the Kb-Bar specimens. The residual stress was examined before the specimens were tested.

Table 29. The Kb-Bar Specimen Residual Stress Profile

Category	Material	ID	RS-0	RS-4	Notes
Baseline (900°F final tempering)	4340 steel	101-1	+67.8/+55.1	-13.95/-7.13	Polish
		101-11	-68.0/-79.4	-46.45/-52.82	
		101-2	-41.8/-54.9	-22.01/-23.15	
		101-3	-66.7/-62.1	-32.19/-33.01	
		101-4	-42.3/-48.3	-26.70/-24.56	
		101-5	-52.4/-58.2	-24.87/-29.99	
		101-6	-78.3/-74.3	-34.31/-32.08	
		101-8	-69.5/-85.1	-33.96/-39.41	
		101-9	-61.1/-64.7	-31.09/-34.24	
	9310 steel	111-1	-60.4/-60.5	-31.18/-26.99	
		111-2	--	-25.70/-35.21	
Carburized*	9310 steel	113-1	-22.9/-31.4	No stress relief	Stock removal
		113-2	-75.78/-76.65		
		119-1	-16.98/-9.63		No stock removal
		119-2	-16.33/-21.17		
Shot-peened	4340 steel	105-1	-88.77/-86.24		No polish
		105-2	-85.55/-87.68		
		105-3	-80.10/-85.52		
		105-4	-87.96/-83.43		
		105-5	-74.55/-73.57		
		105-6	-77.19/-77.49		
		105-7	-84.52/-83.87		
		105-8	-81.75/-86.98		
		105-9	-75.93/-75.51		
	9310 steel	115-1	-95.75/-92.31		
		115-2	-93.35/-92.55		

*The data shown are residual stresses measured at "side A/side B." Side A = first side to be measured; side B = second side to be measured.

4.3 EFFECT OF RESIDUAL STRESS ON Kb-Bar FCG.

4.3.1 The FCG Behavior of Baseline Kb-Bar With As-Machined Residual Stress.

The FCG behavior of the baseline Kb-Bar was examined in terms of *a*/*c* ratio. As has been observed, the machining process actually induced a thin layer (0.002 in.) of compressive residual stress on the surface that was -34 ksi for 4340 steel and -45 ksi for 9310 steel (table 28 and figure 87). In spite of this surface condition, the test results show the crack grew faster in the *c* direction (the tips on the surface) than in the *a* direction (the tip in-depth), disregarding the stress ratio, as shown in figure 88. Figure 89 presents this behavior observed from the baseline test data in terms of crack growth (depth, *a*) versus *a*/*c* ratio. All the baseline Kb-Bar test data show that the *a*/*c* ratio slightly decreases with increasing crack depth, *a*, up to a certain crack size, then remains nearly constant. This means that the crack grew faster on the surface than in-depth during the entire growing time. In other words, the existence of a very small layer of the as-machined residual stress on the surface did not affect the crack growth pattern.

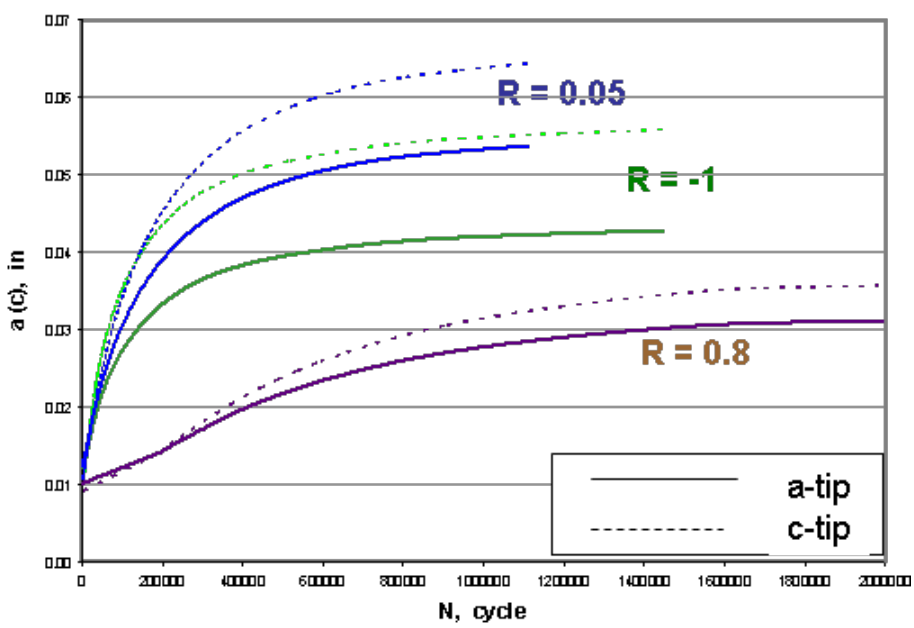

Figure 88. The *a*-N and *c*-N Curves of Baseline Kb-Bar Tests During Load Shedding (4340 Steel)

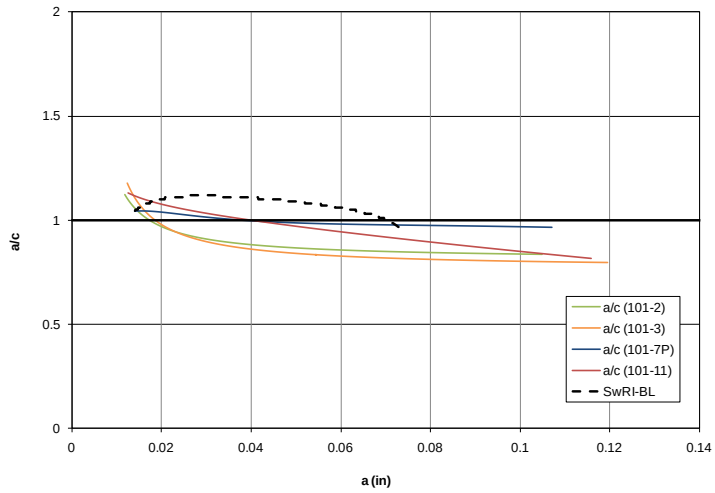

Figure 89. Crack Front Aspect Ratio Comparison of Simulation to Test—Baseline

This same behavior was indicated by the ANSYS CGA for the baseline Kb-Bar condition, shown in figure 67, where the crack grows faster on surface than in-depth with increasing load cycles, and the crack grows from the initial semicircular shape into a semielliptical shape. That is, the crack *a/c* ratio decreases along with crack growth.

Figure 90 shows this crack growth scenario for the baseline Kb-Bar with as-machined residual stress, based on measured *a* and *c* dimensions. Figure 91 is a typical example of an actual baseline Kb-Bar fracture surface. In this case, using only measured crack dimensions, one can predict the actual crack front shape with reasonable accuracy.

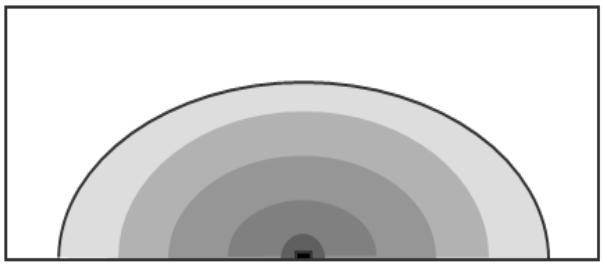

Figure 90. Crack Growth Scenario of Baseline Kb-Bar With As-Machined Residual Stress

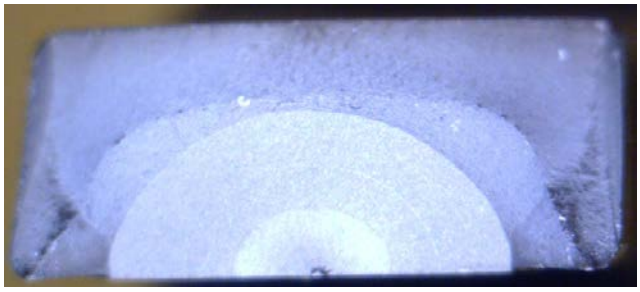

Figure 91. Crack Front Profile of Baseline Kb-Bar With As-Machined Residual Stress

4.3.2 The FCG Behavior of Shot-Peened Kb-Bar.

In contrast to the crack growth behavior of the as-machined baseline Kb-Bar, the shot-peened Kb-Bar crack grew faster in-depth (*a*-tip) than on the surface (*c*-tips), as shown in the *a*-N and *c*-N curves in figure 92 (4340 steel, data generated during K-controlled load shedding). Examination of *a*/*c* ratio versus crack size (*a*), in figure 93, shows that the crack grew faster in depth (*a*-tip) than on the surface (*c*-tip) in the early stage of crack propagation; then the crack growth on the surface (*c*-tip) started competing with the growth in-depth (*a*-tip) and eventually grew faster on the surface. Figure 94 shows a crack growth scenario of the shot-peened Kb-Bar tests, based only on measured crack dimensions. It shows that the residual stress of shot peening tends to resist crack growth along the surface for a small surface crack. In reality, measured surface crack dimensions do not capture the subsurface expansion of the crack front, as shown in figure 95. The baseline case is often described as a semielliptical crack front; the shot-peened case may be described as an inward-shifted ellipse.

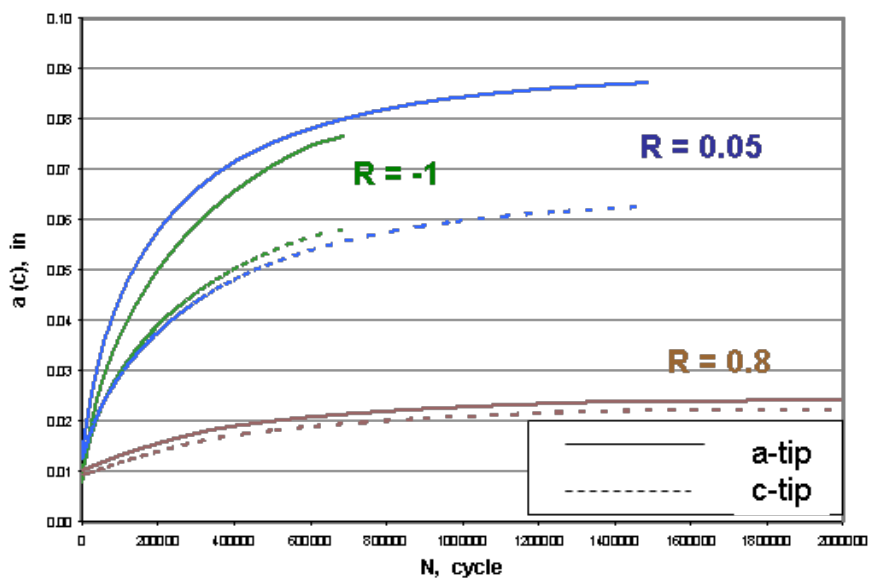

Figure 92. The *a*-N and *c*-N Curves of Shot-Peened Kb-Bar Tests During Load Shedding (4340 Steel)

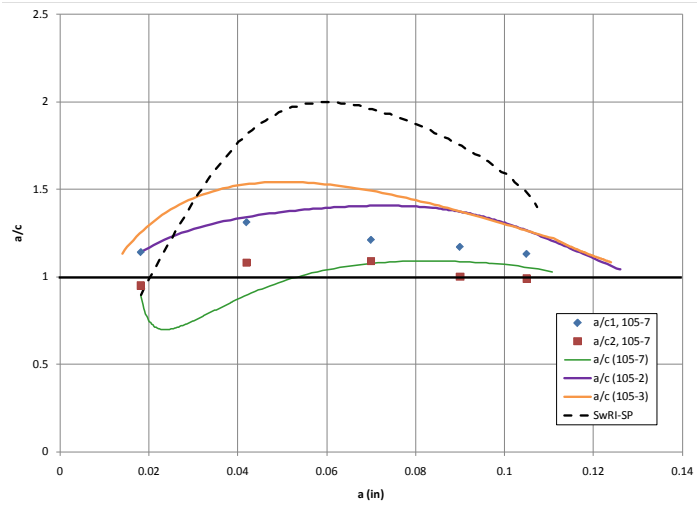

Figure 93. Crack Front Aspect Ratio Comparison of Simulation to Testing—Shot-Peened Kb-Bar Tests

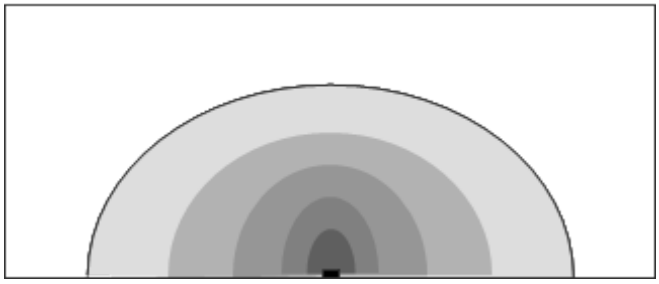

Figure 94. Crack Growth Scenario in the Shot-Peened Kb-Bar Tests

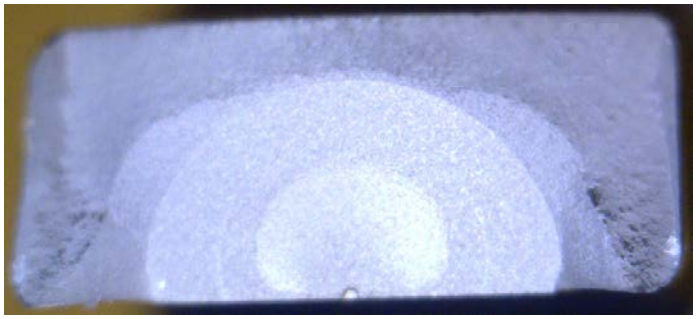

Figure 95. Typical Shot-Peened Kb-Bar Specimen

Specimen 105-7 behaved differently from the typical shot-peened specimens (see figure 93), and posttest examination of this specimen indicated some asymmetry in the growth pattern, possibly due to the proximity of the soldered PD wire (figure 96). Figure 96 also shows that the crack grew slightly faster in the c_2 direction than in the c_1 direction; thus, figure 93 also includes crack shape aspect ratio curves for a/c_1 and a/c_2 separately.

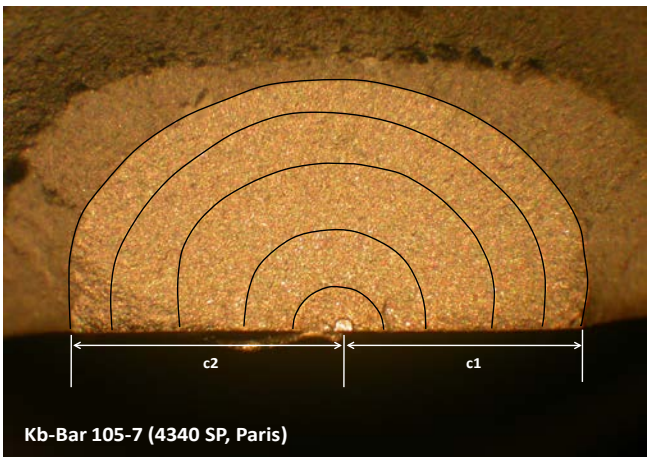

Figure 96. Shot-Peened Kb-Bar Specimen 105-7, Showing Marker Bands

4.3.3 The FCG Behavior of Carburized Kb-Bar.

Only the Paris region data were measured for the 9310 steel carburized Kb-Bar tests. The carburized Kb-Bar specimens revealed very unusual FCG behavior, in which all attempts to grow the crack in the threshold region were unsuccessful, with either no growth or unstable growth. The available test data were not sufficient to determine the effect of surface carburizing on the FCG behavior of a surface crack. Of the two 9310 steel carburized Kb-Bar tests, only one test provided valid data for the data process. On the other hand, the obtained preliminary data revealed interesting FCG behavior of a carburized Kb-Bar. Based on measured depth (*a*) and surface (*c*) dimensions, the predicted crack growth scenario is shown in figure 97. The real crack front, however, is different, at least where the crack approaches the edges of the specimen. A bell-shaped crack front near the edges was observed, as illustrated in figure 98. Contrary to the crack growth scenario of the shot-peened Kb-Bar tests, in the carburized Kb-Bar test the crack grew much faster at the *c*-tips (surface) than in the *a* direction (depth). This FCG behavior might be related to the hard case produced by carburization, which transformed the surface layer of material to be more brittle. It was suspected that, to some extent, the material crack growth resistance might be reduced in the carburized surface layer while the hardening of this surface layer was achieved [34].

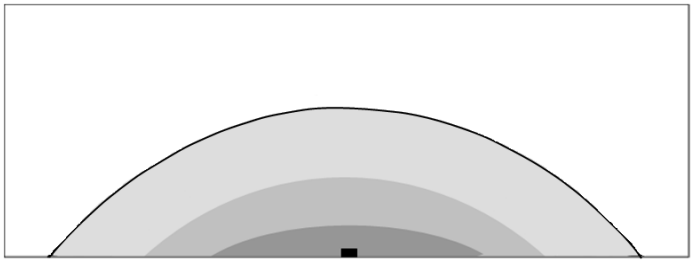

Figure 97. Predicted Crack Surface of a Carburized 9310 Steel Kb-Bar Specimen

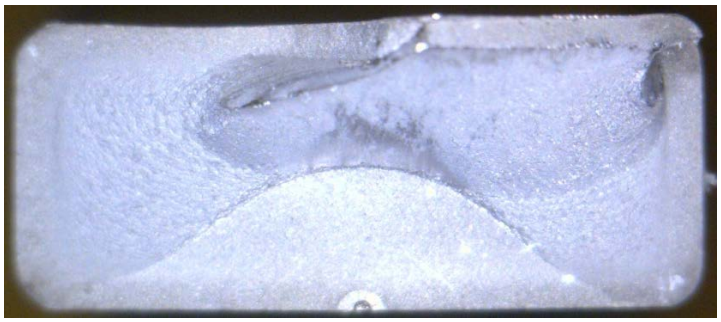

Figure 98. Actual Crack Surface of a Carburized 9310 Steel Kb-Bar Specimen

4.3.4 Comparison of Kb-Bar Test Results Between Baseline and Shot-Peened Specimens.

When comparing crack growth data of the baseline and shot-peened Kb-Bar specimens (4340 steel), as shown in figure 99, caution needs to be exercised due to the non-elliptical shape of the crack front for the shot-peened specimens that are not taken into account in the ΔK calculations. As a first approximation, standard SIF calculations were performed for these specimens to compare them with baseline results. Figure 99 does not show any major shifts in the *da*/*dN* data, except a larger scatter that could be attributed to residual stresses present to various degrees, non-elliptical crack fronts, and some increase in ΔK threshold. A more comprehensive data analysis tool is needed to evaluate surface treatment effects, such as a total number of cycles under the same loading for all three types of specimens.

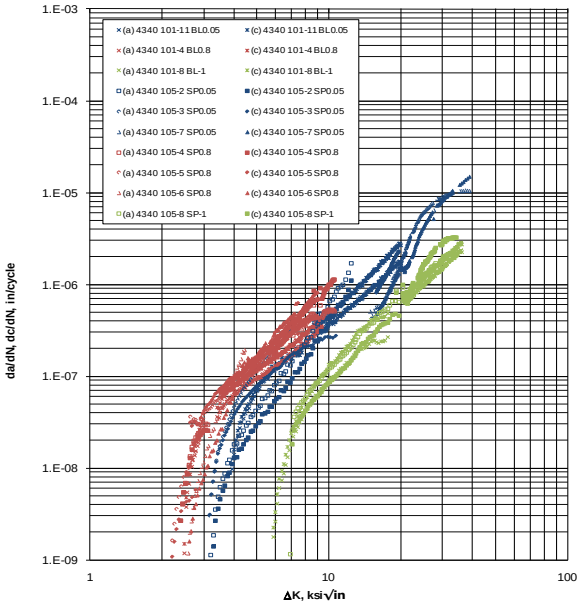

Figure 99. Baseline and Shot-Peened Kb-Bar FCG Curves: R = -1, 0.05, and 0.8 (4340 Steel)

4.3.5 The Kb-Bar CGA Results of Shot-Peened vs Baseline.

The NASGRO simulations, using actual Kb-Bar test conditions (section 3.1.1.3), showed the profound effect of surface residual stress on the growth along the surface (*c*-tips). Figure 33 is a good illustration of how the fundamental crack growth properties of the material are changed due to surface residual stresses. The simulations were run at $R = 0.05$, but the resulting da/dN versus ΔK curves deviate from the basic material data for that stress ratio (the curves of red circles). The mechanism behind this behavior is the variation in R, as shown in figure 34. With the addition of the residual stress layer in the shot-peened specimen, the simulation showed that the stress ratio is actually changed in the surface layer and, thus, the SIF along the *c*-tip was severely impacted. This is consistent with the test results.

The NASGRO simulation of the shot-peened Kb-Bar specimen was somewhat unconservative relative to actual test data, as shown in figure 37. There is some evidence that the crack growth in this test specimen was anomalous, reflected in the shot-peened specimen aspect ratio plot in figure 93, compared to the aspect ratio plot of the baseline specimen in figure 90. The black dashed line in figure 93 is the aspect ratio obtained from the NASGRO simulation. Although the magnitude of the change in aspect ratio is large for the NASGRO prediction, the trend of the change is similar to the test data.

The benefits of surface compressive residual stress were also discussed in the ANSYS SIF results, section 3.2. For Kb-Bar specimens, figure 61 shows that residual stress greatly reduced the SIFs from 16.2 ksi$\sqrt{\text{in.}}$ to 5.5 ksi$\sqrt{\text{in.}}$ near the surface. This would greatly reduce the crack growth rate in the surface layer. However, the SIFs near the crack depth are slightly higher due to the effect of tensile residual stress in this region. Obviously, the residual stress retards the crack growth at the surface but does not at the crack depth.

4.4 EFFECT OF RESIDUAL STRESS ON FILLET ELEMENT FCG.

The effect of residual stress was further evaluated with the shot-peened fillet radius element tests versus the baseline element tests. The FCG behavior seems similar for the specimens of two conditions, with and without shot peening, under M = T loading, as shown in figures 18 and 19. A close inspection of the crack aspect ratio (figures 22 and 23), however, revealed that the crack grew faster on the surface (2*c* measurement) than in the depth (*a* measurement) for unpeened specimen S6 until it reached a certain crack depth and then grew proportionally in depth and on the surface. Nevertheless, for shot-peened specimen P2, the crack grew faster into the depth than on the surface at the beginning (for a small crack) until it reached a certain crack depth, and then grew faster on the surface. This again indicates that shot peening helps to slow down the small crack growing on the surface, whereas the overall effect of shot peening for the M = T loading case appears to be minimal. Additional data would be required before a conclusion can be drawn.

For the M = 2T loading case (figures 20 and 21), both shot-peened specimens (P3 and P4) failed earlier than their unpeened counterparts, with data plotted to show crack growth from a common crack size. An explanation for this may be related to the effect of shot peening on crack front aspect ratio, figures 22 and 23. Kb-Bar data clearly indicated an increase in a/c for cracks in the

shot-peened coupons versus the unpeened coupons. A crack growing faster in the depth direction would transition to a through crack (i.e., break through the tube wall) faster and, therefore, reach a critical crack length faster. This effect is shown in figure 21 for the surface (2*c*) dimension.

It should be emphasized that these results do not necessarily lead to the conclusion that such parts should not be shot-peened, as the shot-peened layer may significantly increase the crack initiation time. However, the results do highlight the need to include the effect of shot peening in any fatigue and DT analysis since omission of these effects may be unconservative.

5. SUMMARY.

This 4-year research program focused on applying rotorcraft damage tolerance (RCDT) technologies to rotorcraft drive system components, which focused on the rotor mast. The building-block fatigue crack growth (FCG) test method that was previously developed under the National Rotorcraft Technology Center/Federal Aviation Administration (FAA)/Rotorcraft Industry Technology Association program was leveraged to develop a damage tolerance (DT) certification test procedure for the rotor mast. The current capability of crack growth analysis (CGA) methods for rotorcraft drive system components, exemplified by a rotor mast, was evaluated with NASGRO, a CGA tool that was developed under a joint effort of the FAA, National Aeronautics and Space Administration, and the Southwest Research Institute® (SwRI®). A commonly used finite element analysis (FEA) tool, ANSYS®, was also evaluated for the potential of FCG analysis. The effect of shot peening on the crack growth behavior of a rotor mast was also evaluated. Shot peening is commonly used in drive system components to improve fatigue life. Carburization is another surface treatment method that is used for drive system parts to enhance the wearing resistance, and thus improve the fatigue life. The effect of carburizing on the surface crack FCG behavior of the typical rotor mast material, 9310 steel, was also investigated. The effect of residual stress induced during machining on the FCG behavior of a surface crack was evaluated as well.

The test program for the DT certification of a rotor mast included coupon, mini-element, and element tests. Although the full-scale tests were not conducted due to funding limitations, it should be included in the integrated building-block test procedure. Each test takes its own role in the characterization, validation, and verification of the capability of DT certification, while each provides data and guidance for the next test. All the test details provide useful and relevant FCG data for critical helicopter parts such as rotor masts and shafts. The material threshold data were obtained by using the middle tension test method, which is mostly representative of the through-typical cracks occurring in shafts of tubular geometry. The surface flaw FCG (Kb-Bar) specimen is well suited to demonstrate the effect of various surface conditions on the growth of a part through surface crack. Element specimens of a shaft configuration were specially designed with a fillet radius. These geometrical features are typical designs for specific functions of rotor masts and drive shafts when the outside diameter changes according to stress level and function, such as bearing installation. Oftentimes, however, these geometries are sensitive and critical to fatigue crack initiation and growth due to the stress concentration inherent in these geometries. The element test generated detailed information on the FCG pattern with the given loads, verified the DT critical design features, and provided guidance for the full-scale tests.

Additional work is required to fully understand the fillet element test results. There is no stress-intensity factor (SIF) closed-form solution available for the element specimen geometry. As a result, SIFs would need to be calculated for incremental crack sizes using finite element (FE) methods. Therefore, crack growth rate data for a more complex geometry should be developed to enable direct comparison with the coupon data. Other critical factors influencing crack growth in shaft elements, including crack and section asymmetries and variable crack plane orientation, must also be considered when interpreting the data.

The current CGA capability of NASGRO for the FCG analysis of rotorcraft drive system components was evaluated. The analyses were demonstrated by FCG simulations of a rotor mast. 4340 steel, a typical rotor mast material, was used. The FCG analysis of the Kb-Bar configuration was first performed to simulate the surface crack growth at the material level, with simple geometry and loading. The analyses were run with baseline and shot-peening residual stress conditions. The FCG simulations were then further performed at the element level with the complex geometries and loading conditions that are representative of a rotor mast. NASGRO was evaluated on its capability to handle the complex geometry and loading conditions, which led to the mixed-mode stress intensity at the crack front. The analysis results were then compared to the test data for both a planar surface crack under uniform stress field and a nonplanar crack under a variable stress field.

At both the coupon and element level, the simulations were performed with the material FCG properties from the NASGRO material library and from the M(T) FCG test data of the same material batch as the Kb-Bar and element test specimens. The purpose of running the simulation with the two material sets was to evaluate the applicability of the NASGRO material library data to the rotorcraft drive system parts, and to determine the ability of integrating user-defined property data. The results based on the two materials resources were comparable, indicating NASGRO's capability to handle user-defined material FCG properties.

NASGRO has an SIF Library for the typical crack shapes under simple load. For a crack of more complex geometry and complex loads, SIF solutions can be developed in a separate FE/boundary element (BE) analysis platform. The obtained SIF table can be integrated into NASGRO for FCG analysis. When residual stress is considered, the residual stress can be imposed on the FE/BE model to modify the SIF solutions.

The NASGRO simulation for the baseline Kb-Bar FCG compared favorably with the Kb-Bar baseline test data. The simulation for the shot-peened Kb-Bar FCG was comparable to the test data at *a*-tip but was underestimated at *c*-tips. Shot peening induced a thin layer of cold-worked and a residual stress gradient on the surface that not only changed the material properties in this layer but also the actual stress ratio during crack growth. The mechanism is not fully understood and, thus, the FCG models used for the analyses may not be completely representative of reality.

The current state-of-the-art technology for FCG analysis is limited to handling the two-dimensional (2D) planar crack. The DT community has been making efforts toward the three-dimensional (3D) capability. The lack of such a capability for a nonplanar crack also applies to the current NASGRO version. Therefore, a 2D planar crack growth was assumed for the fillet radius element FCG analysis. The results showed that the NASGRO analysis successfully

predicted the FCG of the fillet element specimens to a high degree of accuracy, indicating that the planar assumption of FCG to simplify the 3D CGA is acceptable for sufficient fidelity in this specific analysis. Although there is insufficient data to support a conclusion, this observation gives a certain level of confidence in using 2D CGA for a fillet radius crack problem as a simplification to the 3D case. Furthermore, unlike the actual fillet radius element specimen, the element configuration for the analysis focused only on the geometrical features that were supposed to be critical to the crack growth at the fillet radius area. The simplification was made to improve computational efficiency and to reduce the probability of inaccuracy in complex modeling. The consistency between the analysis results and fillet radius element test data confirms the feasibility of the geometrical simplification assumed for the NASGRO FCG analysis. The SIF solutions generated by SwRI for the complex geometries and loads for mixed-mode crack growth were validated by the close agreement of the analysis results to the test data. The potential of the software to model such complex situations is evident.

FCG analysis using ANSYS was conducted for a surface crack in the Kb-Bar and fillet radius element configurations, including SIF calculation and CGA. For crack growth, the analyses were only considered in the Paris region. No attempt was made for the threshold region.

A specialty FEA tool, ANSYS, demonstrated advantages in SIF computation due to its strength in modeling and stress analysis. It has a great capability for implementing a crack with complex geometries. In other words, by repeating crack insertion, the crack extension can be executed in a semimanual manner. The residual stress of the surface layer can be handled with ANSYS. The residual stress gradient was incorporated into the analysis model for SIF solutions. Contact elements on the crack surfaces were used to prevent them from crossing each other due to compressive stresses. Although this geometrically nonlinear analysis increases computer run time, ANSYS can readily impose the residual stress into the analysis.

On the other hand, ANSYS was not designed for CGA, although it is well suited for SIF solutions. To perform CGA, the user must program input macros. For simple geometries like Kb-Bar, the CGA can be automated for efficiency. For each step of crack growth in the automated CGA, the FE model is updated with a new crack size and a new crack shape. However, it is difficult to automate the analysis for complex components such as the fillet radius element because the modeling requires user inputs. Although ANSYS is not ideal for CGA, its capabilities may be expanded to cover this special area of analysis in the future.

The effect of residual stress on the FCG behavior of rotor masts has been evaluated by testing and by analysis. Kb-Bar tests were performed to evaluate the effect of residual stress on FCG behavior with an emphasis on rotor mast materials, i.e., 4340 steel and 9310 steel. The sources of the residual stress are the machining process, shot peening, and carburization, which are typical practices for the as-machined and surface-treated rotor masts. FCG analysis of the Kb-Bar was performed to evaluate the effect of residual stress caused by machining and shot peening on the same materials. The element-level tests were subsequently conducted with an emphasis on the typical design features of rotor mast geometry and representative loading applications. The effect of shot peening on the FCG of the rotor mast element was investigated by comparing the FCG test results of the shot-peened specimens to those of the baseline specimens.

For the investigated materials, it was observed that the as-machined Kb-Bar specimens were not surface stress free, as it was assumed in today's common practice when characterizing FCG properties. Addressing this fact is specifically important to the cases dealing with surface cracks. Both the Kb-Bar testing and analysis results showed that the effect of residual stress induced by machining, shot-peening, and carburizing processes may not be significant on the crack growth rate, but on the crack growth pattern. In particular, shot-peening residual stress forces a small crack to grow into the depth more than on the surface. This effect was further revealed by the FCG analysis. Knowing this pattern is important because the initial FCG pattern determines the accuracy of the prediction of the FCG behavior. The FCG for the carburized Kb-Bar specimens demonstrated an irregular behavior that needs further investigation.

The effect of shot peening on changing crack growth patterns was further exhibited in the element-level evaluation. The surface crack of the shot-peened element grew faster into the depth than on the surface, regardless of loading combinations and crack plane orientations, which is opposite of the crack pattern of the baseline elements. On the other hand, the *a*-N and 2*c*-N curves demonstrated that, for the same geometry and loading conditions, the shot-peened specimens may not necessarily have a longer life than the baseline specimens do. This is because the overall FCG behavior present in *a*-N (or 2*c*-N) curves is the result of multiple factors, including not only shot-peening residual stress, but also geometry and loading complexity. However, a conclusion cannot be drawn at this point due to the limited data. It is recommended that further investigation be carried out to determine the residual stress effects on the FCG behavior of rotor masts at various complex geometries and loads.

Further consideration is also needed to address the effect of the interaction of the stress gradient imposed from the rotor mast geometry and the gradient of shot-peening residual stress. As discussed in section 2, shot peening increased the number of crack growth cycles.

6. REFERENCES.

1. Anderson, T.L., *Fracture Mechanics, Fundamentals and Applications* (2nd edition), CRC Press, Boca Raton, Florida, 1994.

2. ASTM E 647-05, "Standard Method for Measurement of Fatigue Crack Growth."

3. Atluri, S.N., *AGILE-2D Draft User Manual*, University of California, Los Angeles, California, July 1999.

4. Bell Helicopter, Boeing, and Sikorsky, "Implementation of Rotorcraft Damage Tolerance: Technical Issues, Challenges, and Approaches," RITA Interim Technical Report, October 2003.

5. Chen, C.T., Han, Z., Le, D., Tan, P., and Cuevas, E., "Stress-Intensity Factor and Fatigue Crack Growth Analyses for Rotorcraft Using AGILE," *Proceedings of the 7th Joint DoD/FAA/NASA Conference on Aging Aircraft*, New Orleans, Louisiana, September 2003.

6. Cronkhite, J., Michael, J., and Dickson, W., "Helicopter Usage Monitoring and Damage Tolerance Investigation," *1998 USAF Aircraft Structural Integrity Program Conference*, San Antonio, Texas, December 1998.

7. Cronkhite, J., et al., "Research on Practical Damage Tolerance Methods for Rotorcraft Structures," *Proceedings of the 56th American Helicopter Society Annual Forum*, Virginia Beach, Virginia, May 2000.

8. Elber, W., "Fatigue Crack Closure Under Cyclic Tension," *Engineering Fracture Mechanics*, Vol. 2, 1970, pp. 37-45.

9. Erdogan F. and Sih, G.C., "On the Crack Extension in Plates Under Plane Loading and Transverse Shear," *Journal of Basic Engineering*, Vol. 85, 1963, pp. 519-527.

10. Everett, R.A., Jr. and Elber, W., "Damage Tolerance Issues as Related to Metallic Rotorcraft Dynamic Components," *Proceedings of the 54th American Helicopter Society Annual Forum*, Washington, DC, May 1998.

11. Krasnowski, B.R., "Application of Damage Tolerance to Increase Safety of Helicopters in Service," *Proceedings of the Advisory Group for Aerospace Research and Development (AGARD) Conference on Application of Damage Tolerance Principles for Improved Airworthiness of Rotorcraft*, Corfu, Greece, April 1999.

12. Krasnowski, B.R. and Eastin, R., "Strategies for Ensuring Rotorcraft Structural Integrity," *Proceedings of the Advisory Group for Aerospace Research and Development (AGARD) Conference on Application of Damage Tolerance Principles for Improved Airworthiness of Rotorcraft*, Corfu, Greece, April 1999.

13. Krasnowski, B.R., "Rotorcraft Fatigue and Damage Tolerance," *Proceedings of the 25th European Rotorcraft Forum*, Rome, Italy, September 14-16, 1999.

14. Krasnowski, B.R., "Reliability and Durability of Aircraft Structures Made of Fiber Reinforced Plastics," Chapter in *Performance of Plastics*, Carl Hanser Verlag, Munich, Germany, 2001.

15. Krasnowski, B.R., "Fatigue Strength and Damage Tolerance of Thin Sheet Riveted Lap/Splice Joints With Cold-Expanded Holes," *ICAF 24th Symposium*, Toulouse, France, 2001.

16. Le, D., "Research to Improve Rotorcraft Structural Integrity, Reliability, and Safety," Presentation at the *International Society of Science and Applied Technologies on Safety and Reliability Assessment*, Las Vegas, Nevada, August 1999.

17. Le, D., Harrison, C., and Kanninen, M., "Implementation of Damage Tolerance Concepts for Metallic Rotorcraft Structures and Drive Train Components," *Proceedings of the 5th Joint DoD/FAA/NASA Conference on Aging Aircraft*, Orlando, Florida, September 2001.

18. Le, D., "Development and Validation of a Robust Fracture Mechanics Methodology for Damage Tolerance of Rotorcraft," *Proceedings of the International Conference on Fatigue of Materials*, November 2001.

19. Le, D. and Kanninen, M., "The Development of a Methodology for Quantifying Fatigue Crack Growth in Residual Stress Fields for Application to Rotorcraft Design and Maintenance," *Proceedings of ASTM Symposium on the Residual Effects on Fatigue and Fracture Testing and Incorporation of Results Into Design*, Salt Lake City, Utah, May 2004.

20. Lessels, J.M. and Brodrick, R.F., "Shot-Peening as Protection of Surface-Damaged Propeller-Blade Materials," *International Conference on Fatigue of Materials*, Section 8, paper 1, London, England, 1956, pp. 3-13.

21. Mackay, T.L., et al., "Near-Threshold Fatigue Crack Propagation of Several High Strength Steels," *Engineering Fracture Mechanics*, Vol. 18, No. 2, 1983.

22. McClung, R.C., "Analysis of Fatigue Crack Closure During Simulated Threshold Testing," *Fatigue Crack Growth Thresholds, Endurance Limits, and Design, ASTM STP 1372*, 2000, pp. 209-226.

23. NASA Johnson Space Center and SwRI, *Reference Manual*, NASGRO v6.1, May 2010.

24. Newman, J.C., Jr. and Raju, I.S., "Stress-Intensity Factor Equations for Cracks in Three-Dimensional Finite Bodies," NASA Technical Memorandum 83200, 1981.

25. Newman, J.C., "Prediction of Fatigue Crack Growth Under Variable Amplitude and Spectrum Loading Using a Closure Model," *ASTM STP 761, American Society for Testing and Materials*, Philadelphia, Pennsylvania, 1982, pp. 255-277.

26. Newman, J.C., Jr., "A Nonlinear Fracture Mechanics Approach to the Growth of Small Cracks," *Behaviour of Short Cracks in Airframe Components*, AGARD-CP-328, 1982, pp. 6.1-6.26.

27. Paris, P.C. and Erdogan, F., "Critical Analysis of Crack Propagation," *Journal of Basic Engineering*, Vol. 85, 1960, pp. 528-534.

28. Sheldon, J.W., Bain, K.R., and Donald, J.K., "Investigation of the Effects of Shed-Rate, Initial Kmax, and Geometric Constraint on ΔKth in Ti-6Al-4V at Room Temperature," *International Journal of Fatigue*, Vol. 21, 1999, pp. 733-741.

29. Shiao, M., Le, D., et al., "Feasibility Study of a Reliability-Based Damage Tolerance Analysis Method for Rotorcraft Structures and Dynamic Components," *Proceedings of the 7th Joint DoD/FAA/NASA Conference on Aging Aircraft*, New Orleans, Louisiana, September 2003.

30. Tanaka, K. and Nakai, Y., "Propagation and Non-Propagation of Short Fatigue Cracks at a Sharp Notch," *Fatigue of Engineering Materials and Structures*, Vol. 6, 1983, pp. 315-327.

31. Wheeler, O.E., "Spectrum Loading and Crack Growth," *Journal of Basic Engineering*, Vol. 94, 1972, pp. 181-186.

32. Mankins, J.C., "Technology Readiness Levels," Advanced Concepts Office, Office of Space Access and Technology, NASA, April 6, 1995.

33. Chang, J.B., Szamossi, M., and Liu, K-W., "A User's Manual for a Detailed Level Fatigue Crack Growth Analysis Computer Code, the CRKGRO Program," Report AFWAL-TR-81-3093, November 1981.

34. ASM Handbook, ASM International, Materials Park, Ohio, Vol. 19, 1996, pp. 680-690.

APPENDIX A—FATIGUE CRACK GROWTH PROPERTIES OF 4340 STEEL AND 9310 STEEL

A.1 M(T) TESTS.

A.1.1 TEST CONDITIONS.

The tests were performed and the data were reported by Metcut Research Inc., a testing laboratory. The purpose was to develop the threshold and Paris regions of the fatigue crack growth (FCG) curve under steady-state, cyclic conditions for 4340 and 9310 steels. The *da*/*dN* tests were performed at laboratory temperature, following ASTM E 647-05 specifications, with an automated data acquisition system using the direct current (DC) electric potential drop (PD) method of crack measurement.

It was observed that, by nature, middle tension specimens are easily susceptible to uneven cracking per Sections 8.8.3, 8.3.4, and A2.4.1.1 of ASTM E 647-05, and several of these specimens violated these criteria. The 9310 steel specimens were particularly problematic with this unevenness. Some specimens experienced uneven cracking so severely that no valid data could be generated. It was suspected that residual stress might be a potential reason for the severe uneven cracking.

A.1.2 TEST DESCRIPTION.

Twenty-two M(T) FCG specimens were tested following the guidelines provided in ASTM E 647-05. The tests were performed in laboratory air with 20%-30% relative humidity. The nominal specimen sizes had a width of 2 inches, thickness of 0.25 inch, length of 8.00 inches, and initial notch length of 0.20 inch.

The specimens were tested in closed-loop, servo-controlled, hydraulic systems with load capacities of 20,000 lb. The specimens were clamped in MTS hydraulically operated wedge-grips, which were rigidly mounted to the hydraulic actuator and the machine load cell. Prior to the test, the wedge grips were aligned in accordance with ASTM E 1012 and ASTM E 606 practices using a strain gage specimen.

The crack length was measured by using the DC electric PD technique, as described in ASTM E 647-05, Sections A2.5.3 and A6. The method used Johnson's Equation to relate voltage measurements to crack length uses the secant method of data reduction as described in ASTM E 647-05, Section X1.1.

A.1.3 RESULTS—M(T) TEST DATA.

The test conditions and results for the 4340 steel M(T) tests are shown in table A-1. The test conditions and results for the 9310 steel M(T) tests are shown in table A-2.

Table A-1. Test Conditions and Results for 4340 Steel M(T) Tests

Specimen ID	Load Ratio (*R*) Minimum/Maximum	Test Notes	*K*-Gradient (1/inch)/ Maximum Load (lbf)	Δ*K* Threshold (ksi √inch)
4340-1	0.05	1	-2.0/2517	4.43
4340-2	0.05	2	-2.0/2572	4.58
4340-3	0.50		-2.0/3432	2.95
4340-4	0.50		-2.0/2973	2.82
4340-5	0.80		-2.0/9095	2.49
4340-6	0.80		-2.0/5966	2.43
4340-7	-0.50		-2.0/3127	7.67
4340-8	-0.50	3	-2.0/2841	7.93
4340-9	-1.0	1	-2.0/1836	5.09
4340-10	-1.0	1 and 2	-2.0/2597	9.72
4340-11	0.05	2	-2.0/2565	3.89

Notes:

1. Crack lengths were uneven (front versus back) per ASTM E 647-05 Section 8.3.4 >0.0625 inch.
2. Crack lengths were uneven (left versus right) per ASTM E 647-05 Section A2.4.1 >0.050 inch.
3. Crack lengths were uneven (front versus back) per ASTM E 647-05 Section 8.3.4 >0.0625 inch by the end of the threshold development, but became acceptably even during the Paris region segment.

Table A-2. Test Conditions and Results for 9310 Steel M(T) Tests

Specimen ID	Load Ratio (*R*) Minimum/Maximum	Test Notes	*K*-Gradient (1/inch)/ Maximum Load (lbf)	Δ*K* Threshold (ksi √inch)
9310-1	0.05	1	-2.0/---	N/A
9310-2	0.05	1 and 2	-2.0/3715	7.20
9310-3	0.50	1 and 2	-2.0/4048	3.89
9310-4	0.50	2	-2.0/3716	3.46
9310-5	0.80	2	-2.0/7334	2.63
9310-6	0.80		-2.0/7334	2.70
9310-7	-0.50	1	-2.01/---	N/A
9310-8	-0.50	1	-2.01/---	N/A
9310-9	-1.00	1	-2.01/---	N/A
9310-10	-1.00	1	-2.01/---	N/A
9310-11	0.05	1	-2.01/---	N/A

Notes:
1. Crack lengths were uneven (front versus back) per ASTM E 647-05 Section 8.3.4 >0.0625 inch.
2. Crack lengths were uneven (left versus right) per ASTM E 647-05 Section A2.4.1 >0.050 inch.

A.2 Kb-Bar TESTS.

A.2.1 CONDITIONS AND DATA GENERATION.

The tests were performed and reported by Metcut Research Inc. Twenty-six FCG experiments were performed on 4340 and 9310 steel, surface-flawed (Kb-Bar) specimens. The tests were performed in accordance with ASTM E 647-00 requirements. The specimen surface conditions were baseline, shot-peened, and carburized.

A.2.1.1 Test Program Description.

The program included crack *a*-tip growth rate (*da*/*dN*) tests at laboratory temperature, per ASTM E 647-00. The tests were performed in MTS servo-hydraulic test frames equipped with FTA Systems using the DC electric PD method of crack measurement.

The primary purpose of the Kb-Bar test was to develop characteristic FCG curves of *da*/*dN* versus stress-intensity range (ΔK) for all specimens, focusing on the threshold and Paris regions. All the tests were performed at 20 Hz using a sinusoidal wave shape.

All specimens assigned for threshold development were performed under a *K*-shedding mode in accordance with Section 8.6 of ASTM E 647-00 until near-threshold growth rates were developed. The ΔK threshold values were then computed from a linear fit of this data in accordance with Section 9.4 of ASTM E 647-00. All test data less than 3.95×10^{-8} inches per cycle growth rate were used for calculating the ΔK threshold.

After the threshold regions were characterized, the specimens were tested under a constant force mode to develop overlapping data into the Paris region.

A.2.1.2 Precracking.

The precracking for the majority of the specimens was performed manually, using optical microscopic measurement techniques to initiate a sharp fatigue crack from both ends of the electrical discharge machining (EDM) starter notches. The goal was to develop a sharpened fatigue crack to a surface length (2*c*) of roughly 0.020 inch. After the precracking preparations were completed, the specimens were removed from the machine and instrumented with PD sensing leads, which were necessary for crack measurement.

The shot-peened specimens had to be precracked under *K*-control automated mode because the crack could not be measured optically. The precracking for the baseline specimens and the carburized specimens, where optical techniques were viable, were performed at constant load amplitude at cross-sectional stress levels of 90-120 ksi. The shot-peened specimens were precracked in crack tip *K*-control so the test loads would decrease incrementally as the crack grew.

A.2.2 TEST DESCRIPTION.

Twenty-six surface-flawed Kb-Bar FCG specimens were tested following the guidelines provided in ASTM E 647-00 with three surface conditions: baseline, shot-peened, and carburized. The tests were performed in laboratory air with 30%-55% relative humidity. The specimen geometries were 0.170 inch wide, 0.400 inch thick, and 5.00 inch long, with an EDM notch of 0.005 inch deep by 0.010 inch long.

The specimens were tested in MTS closed-loop, servo-controlled hydraulic systems with load capacities of 20,000 lb. The test fixture for all frames was aligned prior to the test according to practices outlined in ASTM E 1012 and E 606. This alignment was performed to minimize bending moments, which could influence the crack growth rates. The fixture was adjusted so the maximum amount of bending was less than 5% of the averaged strain output as measured from the alignment specimen.

For correct and accurate computations of ΔK, the exact dimensions of the crack depth (a) and the surface crack length ($2c$) must be known. However, the exact crack depths cannot be measured until the specimen fails, and direct measurements of the crack shape must be made from periodic heat tint measurements or other surface-marking techniques. Most specimens for this program experienced near semicircular and/or penny-shaped crack growth behavior.

The K-solution used to calculate crack tip stress intensity was taken from National Aeronautics and Space Administration (NASA) Technical Memorandum 83200 [A-1]. The Roe-Coffin PD solution [A-2] was used to predict crack length in real time.

Since there is a lack of extensive literature on this type of specimen, brief definitions of some terms used in the report are given below.

- $2c$—Total crack length as measured through the width direction of the specimen during real-time tests, or as measured posttest from heat tint markings. Sometimes the maximum crack length is on the surface of the specimen, but often it is within the depth of the specimen.

- a—Total crack depth. This exact value cannot be measured during real-time tests. It must be measured from heat tint measurements or texture markings after specimen rupture.

- da/dN—The rate of change in crack depth (a) versus change in cycles (N).

- dc/dN—The rate of change in half surface crack length (c) versus change in cycles (N).

- Crack Shape Aspect Ratio (a/c)—The relationship between the maximum crack length ($2c$) and the crack depth (a) at any point in the test, measured through heat tints or extrapolated by means of mathematical models.

- Delta K (ΔK)—The magnitude of the crack tip stress-intensity range at the deepest point of the crack measured 90° from the front face of the specimen. The K-solution used for this test program was taken from NASA Technical Memorandum 83200.

- W—Specimen width as measured across the gage section, nominally 0.170 inch for this specimen design.

- T—Specimen thickness, nominally 0.400 inch for this specimen design.

A.2.3 TEST PROCEDURE.

A.2.3.1 Test Discussion.

The test specimens were precracked at laboratory temperature until a surface crack was initiated from both ends of the EDM notch, the length of the crack ($2c$) was about 0.020 inch long, and the crack depth was estimated to be 0.010 inch deep. The precracks were performed at 20 Hz.

After precrack, the specimens were reinstalled into the frame and were "buzzed" to mark the starting crack shape clearly. The high-cycle buzzing technique is a procedure by which the test conditions and parameters can be purposely altered to create a clear, visible marking on the cracked surface of the specimen. Most of the specimens revealed at least 3 to 4 markings that could be accurately measured posttest to correct the raw data.

A.2.3.2 Posttest Correction.

For most of the experiments, the crack shape closely modeled the ideal relationship of 2:1 for the ratio of $2c/a$, very close to ideal semicircular crack growth behavior, but precise posttest measurements of the buzz fatigue markings allowed for very precise analyses. The tables in section A.2.4 list the crack depth versus length relationship for all visible buzz markings, as well as the individual test conditions.

A.2.4 RESULTS—Kb Bar TEST DATA.

A.2.4.1 4340 Steel.

Tables A-3 and A-4 show the test conditions and results for the 4340 steel Kb-Bar tests under baseline and shot-peening conditions.

Table A-3. Test Results of 4340 Steel Baseline Kb-Bar Tests

Test Number	Specimen Number	Load Ratio (*R*) Minimum/Maximum	*K*-Gradient (1/inch) Threshold	Maximum Load (lbf) Paris	Δ*K* Threshold (ksi√inch)	Total Test Hours
1-246	101-11	0.05	-30.0	2173	3.94	83.3
2-246	101-2	0.05	-30.0	2278	3.91	105.1
3-246	101-3	0.05	-30.0	2404	3.55	26.4
4-246	101-4	0.80	-30.0	4680	2.54	57.0
5-246	101-5	0.80	-30.0	5934	2.51	29.1
6-246	101-6	0.80	-30.0	5857	2.59	53.3
7-246	101-8	-1.00	-30.0	2329	5.99	25.3
8-246	101-9	-1.00	-30.0	2436	7.61	58.4
1-246-01-02	101-7	0.05	N/A	5973	N/A	3.0
3-246-01-02	101-10	-1.00	-30.0	2687	8.34	46.1

Table A-4. Test Results of 4340 Steel Shot-Peened Kb-Bar Tests

Test Number	Specimen Number	Load Ratio (*R*) Minimum/Maximum	*K*-Gradient (1/inch) Threshold	Maximum Load (lbf.) Paris	Δ*K* Threshold (ksi√inch)	Total Test Hours
13-246*	105-1	0.05	N/A	5966	N/A	N/A
15-246	105-2	0.05	-30.0	2580	3.41	33.4
17-246	105-3	0.05	-30.0	2782	3.11	36.8
18-246	105-4	0.80	-30.0	5700	2.44	74.3
19-246	105-5	0.80	-30.0	5827	2.35	36.8
20-246	105-6	0.80	-30.0	5748	2.77	90.9
16-246	105-7	0.05	N/A	5968	N/A	6.8
22-246	105-8	-1.00	-30.0	2178	6.93	50.8
23-246	105-9	-1.00	-30.0	N/A	1.61	46.71

* Specimen failed during precrack operation because operator could not visually see the surface crack. Subsequent specimens were precracked under *K*-control automation.

A.2.4.2 9310 Steel.

Tables A-5 through A-7 show the test conditions and results for the 9310 steel Kb-Bar tests under baseline, carburizing, and shot-peening conditions.

Table A-5. 9310 Steel Baseline Kb-Bar Test Results

Test Number	Specimen Number	Load Ratio (*R*) Minimum/Maximum	*K*-Gradient (1/inch) Threshold	Maximum Load (lbf) Paris	Δ*K* Threshold (ksi√inch)	Total Test Hours
9-246	111-1	0.05	-30.0	2486	4.11	32.7
10-246	111-2	0.05	-30.0	2165	3.97	45.6
2-246-01-02	111-3	0.05	---	5946	N/A	3.40

Table A-6. 9310 Steel Carburized Kb-Bar Test Results

Test Number	Specimen Number	Load Ratio (*R*) Minimum/Maximum	*K*-Gradient (1/inch) Threshold	Maximum Load (lbf) Paris	Δ*K* Threshold (ksi√inch)	Total Test Hours
11-246	119-1	0.05	N/A	6007	N/A	5.6
12-246	119-2	0.05	-15.0	2950	N/A*	71.4

* Strange inexplicable crack growth behavior was observed. The buzz marking efforts were not successful. The crack propagated in the depth direction (a) to the back side; therefore, the absolute crack shape could not be determined. Data for this test should be regarded as informational only.

Table A-7. 9310 Steel Shot-Peened Kb-Bar Test Results

Test Number	Specimen Number	Load Ratio (*R*) Minimum/Maximum	K-Gradient (1/inch) Threshold	Maximum Load (lbf) Paris	ΔK Threshold (ksi√inch)
14-246	115-1	0.05	-30.0	2204	3.74
21-246	115-2	0.05	N/A	7882	N/A

A.3 REFERENCES.

A-1. Newman, J.C. and Raju, I.S., "Stress Intensity Factor Equations for Cracks in Three-Dimensional Finite Bodies," August 1981.

A-2. Gangloff, R.P., "Electric Potential Monitoring of Crack Formation and Subcritical Growth From Small Defects," *Fatigue of Engineering Materials and Structures*, Vol. 4, Issue 1, 1981, pp. 15-33.

APPENDIX B—STRESS-INTENSITY FACTOR SOLUTION FOR FILLET RADIUS ELEMENT

The computed reference stress-intensity factor (SIF) solutions are listed in this appendix. The analysis was conducted at Southwest Research Institute® (SwRI®), and reported by SwRI.

For surface cracks, the values presented are normalized SIF results $\widetilde{K}_i$ with respect to a normalization factor defined by

$$\sqrt{\pi a}/\Phi$$

where

$$\widetilde{K}_i = {K_i} \Big/ \left(\sqrt{\pi a}/\Phi\right)$$

with the subscript *i* denoting the fracture modes varying from I, II, and III. Note that the normalized SIF results are implicitly in terms of reference loads.

Tables B-1 and B-2 tabulate the normalized reference SIF solutions for surface cracks with a crack plane angle of 15°. Table B-1 shows the crack subjected to reference shear force, and table B-2 shows the crack subjected to reference torque. For the crack plane angle equal to 30°, tables B-3 and B-4 list similar sets of reference SIF solutions for the surface crack subjected to reference shear force and torque, respectively.

Unlike the results for surface cracks, the SIF results for through-thickness cracks shown in this report are absolute. Nonetheless, they are also implicitly in terms of the reference loads. The numerical results are presented at two crack tips and were determined through averaging across the crack tip perimeters. Tables B-5 and B-6 tabulate the reference SIF solutions for through-thickness cracks with a crack plane angle of 15° for two reference loads, and tables B-7 and B-8 show similar results for the crack plane angle equal to 30°.

Table B-1. Normalized SIF Values at Three Crack Tips for a Slanted Surface Crack With a Crack Plane Angle of 15° Subjected to Reference Shear Force

		c_1-tip (ksi)			a-tip (ksi)			c_2-tip (ksi)		
a/t	a/c	$\widetilde{K}_{\mathrm{I}}$	$\widetilde{K}_{\mathrm{II}}$	$\widetilde{K}_{\mathrm{III}}$	$\widetilde{K}_{\mathrm{I}}$	$\widetilde{K}_{\mathrm{II}}$	$\widetilde{K}_{\mathrm{III}}$	$\widetilde{K}_{\mathrm{I}}$	$\widetilde{K}_{\mathrm{II}}$	$\widetilde{K}_{\mathrm{III}}$
0.04484	0.5	1.7508	-0.3774	0.1020	2.3441	3.5763	0.3961	1.9000	0.3114	0.2361
	0.75	2.1381	-0.3930	-0.0125	2.4342	3.4444	0.4324	2.2683	0.2379	0.1822
	1.0	2.4219	-0.2989	0.0550	2.4205	2.6284	0.4377	2.6059	0.1235	0.0801
0.22422	0.5	1.5566	-0.3268	0.1612	1.8573	0.7859	0.3353	1.6365	0.3047	0.3828
	0.75	1.9387	-0.4010	0.0748	1.8205	0.6334	0.3308	2.0288	0.4328	0.3380
	1.0	2.2375	-0.4156	0.0550	1.7874	0.4030	0.3185	2.3332	0.4878	0.2928
0.89686	0.5	1.6765	-0.2336	0.2541	1.6254	0.2912	0.2405	1.6117	2.4432	-1.6911
	0.75	2.0160	0.3855	0.1765	1.4596	-0.2385	0.2397	1.6126	-0.4424	0.4495
	1.0	2.2561	-0.4392	0.1124	1.3283	0.2004	0.2216	2.0444	0.5336	0.3627

Table B-2. Normalized SIF Values at Three Crack Tips for a Slanted Surface Crack With a Crack Plane Angle of 15° Subjected to Reference Torque

		c_1-tip (ksi)			a-tip (ksi)			c_2-tip (ksi)		
a/t	a/c	$\widetilde{K}_{\mathrm{I}}$	$\widetilde{K}_{\mathrm{II}}$	$\widetilde{K}_{\mathrm{III}}$	$\widetilde{K}_{\mathrm{I}}$	$\widetilde{K}_{\mathrm{II}}$	$\widetilde{K}_{\mathrm{III}}$	$\widetilde{K}_{\mathrm{I}}$	$\widetilde{K}_{\mathrm{II}}$	$\widetilde{K}_{\mathrm{III}}$
0.04484	0.5	0.0376	0.0566	-0.0245	0.0518	0.0871	-0.0729	0.0409	-0.0619	-0.0229
	0.75	0.0530	0.0597	-0.0213	0.0582	0.1572	-0.0722	0.0566	-0.0720	-0.0185
	1.0	0.0682	0.0583	-0.0194	0.0591	0.1719	-0.0700	0.0750	-0.0779	-0.0269
0.22422	0.5	0.0362	0.0547	-0.0295	0.0459	0.0344	-0.0642	0.0416	-0.0607	-0.0223
	0.75	0.0442	0.0710	-0.0229	0.0443	0.0287	-0.0612	0.0510	-0.0753	-0.0172
	1.0	0.0530	0.0798	-0.0212	0.0446	0.0354	-0.0586	0.0588	-0.0839	-0.0197
0.89686	0.5	0.0454	0.0598	-0.0369	0.0420	0.0043	-0.0604	0.1680	0.0162	-0.0460
	0.75	0.0524	-0.0779	-0.0220	0.0387	-0.0046	-0.0541	0.0524	0.0623	-0.0064
	1.0	0.0567	0.0882	-0.0140	0.0353	0.0040	-0.0485	0.0616	-0.0770	-0.0041

Table B-3. Normalized SIF Values at Three Crack Tips for a Slanted Surface Crack With a Crack Plane Angle of 30° Subjected To Reference Shear Force

		c_1-tip (ksi)			a-tip (ksi)			c_2-tip (ksi)		
a/t	a/c	$\widetilde{K}_{\mathrm{I}}$	$\widetilde{K}_{\mathrm{II}}$	$\widetilde{K}_{\mathrm{III}}$	$\widetilde{K}_{\mathrm{I}}$	$\widetilde{K}_{\mathrm{II}}$	$\widetilde{K}_{\mathrm{III}}$	$\widetilde{K}_{\mathrm{I}}$	$\widetilde{K}_{\mathrm{II}}$	$\widetilde{K}_{\mathrm{III}}$
0.04484	0.5	1.4334	-0.6655	0.2167	2.1375	5.0593	0.6988	1.6320	0.6195	0.3741
	0.75	1.7649	-0.7619	0.2184	1.9795	1.5852	0.7253	1.9241	0.7738	0.3282
	1.0	2.0039	-0.8375	0.0763	1.8104	4.2108	0.6807	2.1004	0.3332	0.3264
0.22422	0.5	1.2516	-0.5577	0.3036	1.6120	1.3459	0.5625	1.1319	0.6003	0.4056
	0.75	1.5786	-0.7190	0.1988	1.5546	0.9698	0.5757	1.5766	0.7296	0.4636
	1.0	1.8444	-0.8076	0.1820	1.5078	0.7641	0.5632	1.8792	0.8079	0.4450
0.89686	0.5	1.3016	-0.4109	0.4541	1.4126	0.3698	0.4102	0.8785	0.4301	0.3802
	0.75	1.5884	-0.6653	0.3417	1.2380	0.2067	0.3959	0.9229	0.7759	0.2171
	1.0	1.8001	-0.7793	0.2549	1.1152	0.1836	0.3863	0.9144	1.2322	-1.2659

Table B-4. Normalized SIF Values at Three Crack Tips for a Slanted Surface Crack With a Crack Plane Angle of 30° Subjected to Reference Torque

		c_1-tip (ksi)			a-tip (ksi)			c_2-tip (ksi)		
a/t	a/c	$\widetilde{K}_{\mathrm{I}}$	$\widetilde{K}_{\mathrm{II}}$	$\widetilde{K}_{\mathrm{III}}$	$\widetilde{K}_{\mathrm{I}}$	$\widetilde{K}_{\mathrm{II}}$	$\widetilde{K}_{\mathrm{III}}$	$\widetilde{K}_{\mathrm{I}}$	$\widetilde{K}_{\mathrm{II}}$	$\widetilde{K}_{\mathrm{III}}$
0.04484	0.5	0.0624	0.0288	-0.0112	0.0869	0.1368	-0.0468	0.0677	-0.0360	-0.0065
	0.75	0.0812	0.0348	-0.0111	0.0874	0.0962	-0.0387	0.0851	-0.0409	-0.0096
	1.0	0.0761	0.0057	-0.0045	0.0846	0.1135	-0.0549	0.0749	-0.0214	0.0019
0.22422	0.5	0.0604	0.0314	-0.0137	0.0760	0.0301	-0.0397	0.0583	-0.0344	0.0065
	0.75	0.0743	0.0381	-0.0109	0.0750	0.0330	-0.0368	0.0765	-0.0423	0.0012
	1.0	0.0857	0.0418	-0.0104	0.0734	0.0299	-0.0348	0.0876	-0.0468	-0.0026
0.89686	0.5	0.0775	0.0388	-0.0144	0.0789	0.0081	-0.0379	0.0678	-0.0277	-0.0011
	0.75	0.0911	0.0463	-0.0064	0.0681	0.0040	-0.0321	0.0840	-0.0097	0.0006
	1.0	0.0998	0.0500	-0.0034	0.0616	0.0110	-0.0287	0.1332	0.0207	-0.0384

Table B-5. The SIF Values at Two Crack Tips for a Slanted Through-Thickness Crack With a Crack Plane Angle of 15° Subjected to Reference Shear Force

β_1	β_2	c_1 (in.)	c_2 (in.)	c_1-tip (ksi$\sqrt{\text{in.}}$)			c_2-tip (ksi$\sqrt{\text{in.}}$)		
				K_I	K_{II}	K_{III}	K_I	K_{II}	K_{III}
21.734°	21.734°	0.223	0.223	1.0425	0.1619	0.1007	1.0031	-0.2420	0.0396
	49.063°		0.5	1.5158	0.1286	0.1479	1.1842	-0.1490	0.1903
	79.089°		0.8	2.0658	0.1138	0.1527	1.2654	-0.0479	0.2587
49.063°	21.734°	0.5	0.223	1.3343	-0.1120	0.1526	1.4530	0.3314	0.0190
	49.063°		0.5	1.9428	-0.0982	0.1613	1.7376	0.2792	0.1351
	79.089°		0.8	2.6517	0.0573	0.2155	1.8839	-0.0880	0.3922
79.089°	21.734°	0.8	0.223	1.4271	-0.0649	0.2025	1.9608	0.3734	0.1187
	49.063°		0.5	2.2386	-0.0167	0.2181	2.4191	0.3242	0.1944
	79.089°		0.8	3.1670	-0.0204	0.3251	2.7313	-0.1231	0.5219

Table B-6. The SIF Values at Two Crack Tips for a Slanted Through-Thickness Crack With a Crack Plane Angle of 15° Subjected to Reference Torque

β_1	β_2	c_1 (in.)	c_2 (in.)	c_1-tip (ksi$\sqrt{\text{in.}}$)			c_2-tip (ksi$\sqrt{\text{in.}}$)		
				K_I	K_{II}	K_{III}	K_I	K_{II}	K_{III}
21.734°	21.734°	0.223	0.223	0.0267	-0.0452	-0.0069	0.0278	0.0407	-0.0060
	49.063°		0.5	0.0393	-0.0611	-0.0176	0.0366	0.0473	-0.0176
	79.089°		0.8	0.0560	-0.0803	-0.0357	0.0434	0.0649	-0.0314
49.063°	21.734°	0.5	0.223	0.0373	0.0640	-0.0172	0.0426	-0.0546	-0.0178
	49.063°		0.5	0.0556	0.0799	-0.0331	0.0555	-0.0611	-0.0296
	79.089°		0.8	0.0782	-0.0987	-0.0586	0.0655	0.0773	-0.0506
79.089°	21.734°	0.8	0.223	0.0436	0.0879	-0.0383	0.0622	-0.0725	-0.0381
	49.063°		0.5	0.0687	0.1045	-0.0613	0.0794	-0.0751	-0.0522
	79.089°		0.8	0.0999	-0.1255	-0.0980	0.0973	0.0931	-0.0811

Table B-7. The SIF Values at Two Crack Tips for a Slanted Through-Thickness Crack With a Crack Plane Angle of 30° Subjected To Reference Shear Force

β_1	β_2	c_1 (in.)	c_2 (in.)	c_1-tip (ksi$\sqrt{\text{in.}}$)			c_2-tip (ksi$\sqrt{\text{in.}}$)		
				K_I	K_{II}	K_{III}	K_I	K_{II}	K_{III}
21.734°	21.734°	0.223	0.223	0.8174	-0.2955	0.1705	0.7100	0.4400	-0.0415
	49.063°		0.5	1.1742	-0.3338	0.3075	0.9020	0.4062	0.2721
	79.089°		0.8	1.6772	-0.3141	0.4639	0.9858	0.1856	0.4869
49.063°	21.734°	0.5	0.223	1.0572	-0.2590	0.3014	1.0327	0.5512	-0.0871
	49.063°		0.5	1.4634	-0.2959	0.4056	1.2486	0.4904	0.3649
	79.089°		0.8	2.0946	-0.2789	0.5338	1.4107	0.2302	0.6455
79.089°	21.734°	0.8	0.223	1.1314	-0.1556	0.4331	1.4055	0.7237	0.0333
	49.063°		0.5	1.6216	-0.1290	0.5320	1.7094	0.5834	0.5115
	79.089°		0.8	2.3821	-0.0835	0.6927	1.9001	0.3266	0.9746

Table B-8. The SIF Values at Two Crack Tips for a Slanted Through-Thickness Crack With a Crack Plane Angle of 30° Subjected to Reference Torque

β_1	β_2	c_1 (in.)	c_2 (in.)	c_1-tip (ksi$\sqrt{\text{in.}}$)			c_2-tip (ksi$\sqrt{\text{in.}}$)		
				K_I	K_{II}	K_{III}	K_I	K_{II}	K_{III}
21.734°	21.734°	0.223	0.223	0.0438	0.0264	-0.0039	0.0417	-0.0179	0.0004
	49.063°		0.5	0.0661	0.0347	-0.0098	0.0560	-0.0284	-0.0028
	79.089°		0.8	0.0952	0.0480	-0.0208	0.0691	-0.0487	-0.0115
49.063°	21.734°	0.5	0.223	0.0633	0.0423	-0.0050	0.0615	-0.0234	-0.0069
	49.063°		0.5	0.0901	0.0509	-0.0116	0.0802	-0.0345	-0.0095
	79.089°		0.8	0.1279	0.0633	-0.0248	0.0985	-0.0554	-0.0182
79.089°	21.734°	0.8	0.223	0.0760	0.0672	-0.0139	0.0881	-0.0327	-0.0183
	49.063°		0.5	0.1160	0.0797	-0.0285	0.1176	-0.0427	-0.0241
	79.089°		0.8	0.1529	0.0930	-0.0383	0.1349	-0.0624	-0.0262

APPENDIX C—FLOW CHARTS FOR Kb-Bar STRESS-INTENSITY FACTOR SOLUTION

Figure C-1 shows a flow chart of the procedure for calculating the stress-intensity factors (SIF) of Kb-Bar with a semielliptical crack of which the crack shape, *a*/*c* ratio, is held constant but the crack depth is allowed to grow. This flow chart illustrates a typical procedure of SIF solutions. Its details may be slightly modified to accommodate the requirement of crack growth analysis. However, the methodology in general is not affected.

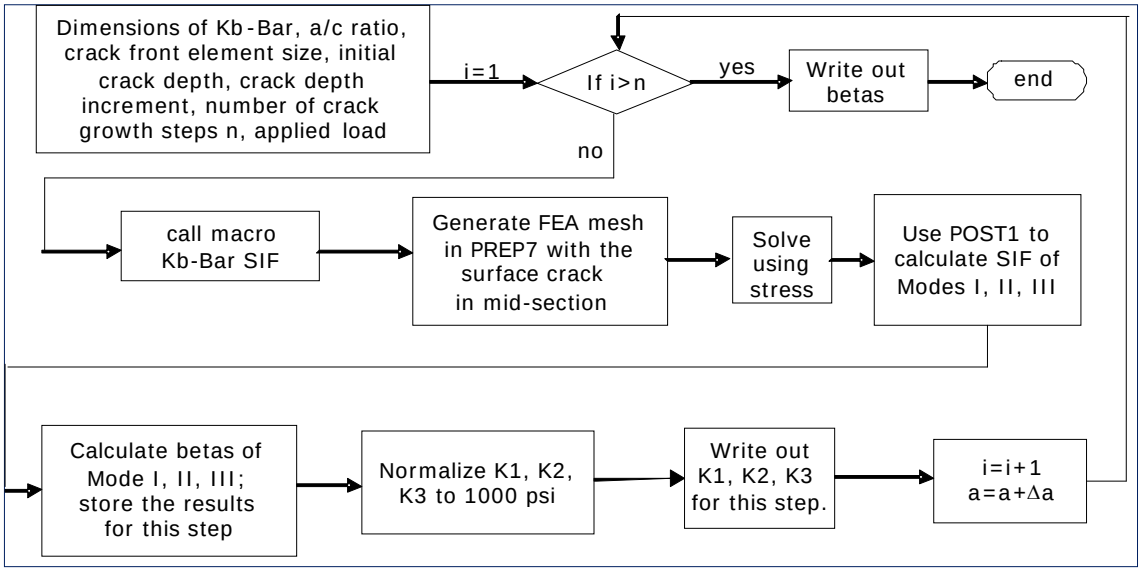

Figure C-1. Procedure for Calculating Kb-Bar SIFs

APPENDIX D—RESIDUAL STRESS DISTRIBUTIONS IN 4340 STEEL AND 9310 STEEL Kb-Bars

This work was performed and reported by Lambda Research, Inc.

D.1 CONDITIONS.

Five Kb-Bars were received from Bell Helicopter Textron, Inc. to determine the longitudinal subsurface residual stress distributions. The nominal dimensions of the Kb-Bars, identified in table D-1, were 0.4-in. (10-mm) gage width and 0.2-in. (4-mm) gage thickness.

Table D-1. Conditions of the Examined Samples

Sample ID	Sample Name	Sample Material
101-1	Baseline	4340 steel
105-1	Shot peen	4340 steel
111-2	Baseline	9310 steel
115-1	Shot peen	9310 steel
113-1	Carburized	9310 steel

D.2 TECHNIQUE.

X-ray diffraction residual stress measurements were made at the surface and at nominal depths of 2.0, 5.0, 10.0, 15.0, and 30.0 x 10-3 in. (51, 127, 254, 381 and 762 x 10-3 mm). Measurements were made in the longitudinal direction in the gage region.

The value of the x-ray elastic constant, $E/(1 + \nu)$, required to calculate the macroscopic residual stress from the strain measured normal to the <211> planes of 4340 steel. This was previously determined empirically by using a simple rectangular beam manufactured from 4340 steel loaded in four-point bending on the diffractometer to known stress levels and measuring the resulting change in the spacing of the <211> planes in accordance with ASTM E 1426.

The value of the x-ray elastic constant, $E/(1 + \nu)$, required to calculate the macroscopic residual stress from the strain measured normal to the <211> planes of 9310 steel. This was previously determined empirically by using a simple rectangular beam manufactured from 9310 steel loaded in four-point bending on the diffractometer to known stress levels and measuring the resulting change in the spacing of the <211> planes in accordance with ASTM E 1426.

Material was removed electronically for subsurface measurement to minimize possible alteration of the subsurface residual stress distribution as a result of material removal. All data obtained as a function of depth were corrected for the effects of the penetration of the radiation used for residual stress measurement into the subsurface stress gradient. The stress gradient correction applied to the last depth measured was based upon an extrapolation to greater depths and may result in overcorrection at the last depth if the stress profile was terminated in the presence of a steep gradient.

D.3 RESULTS.

The longitudinal residual stress distributions measured as functions of depth are shown in figures D-1 and D-2. Compressive stresses are shown as negative values and tensile as positive; in units of ksi (10^3 psi) and MPa (10^6 N/m^2).

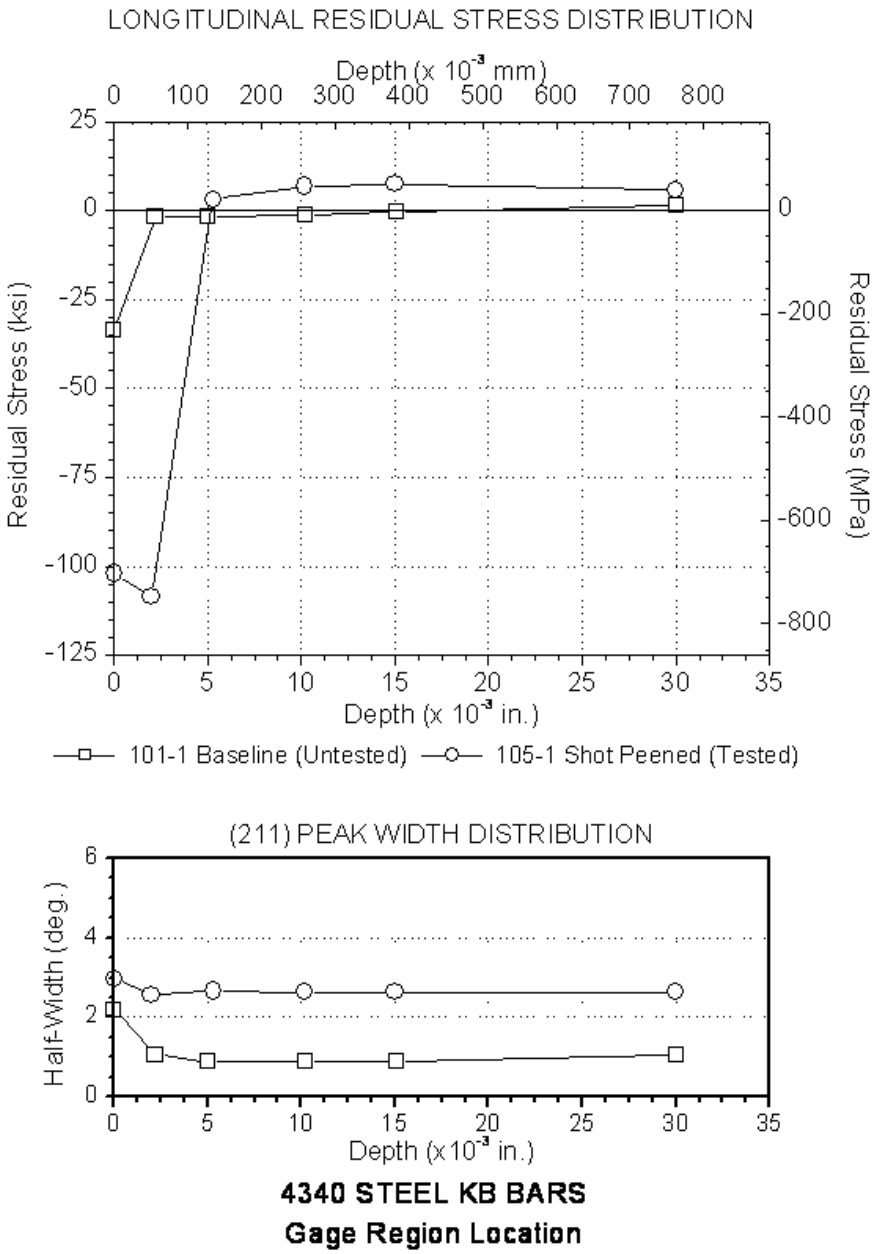

Figure D-1. Residual Stress Measurements of 4340 Steel Samples

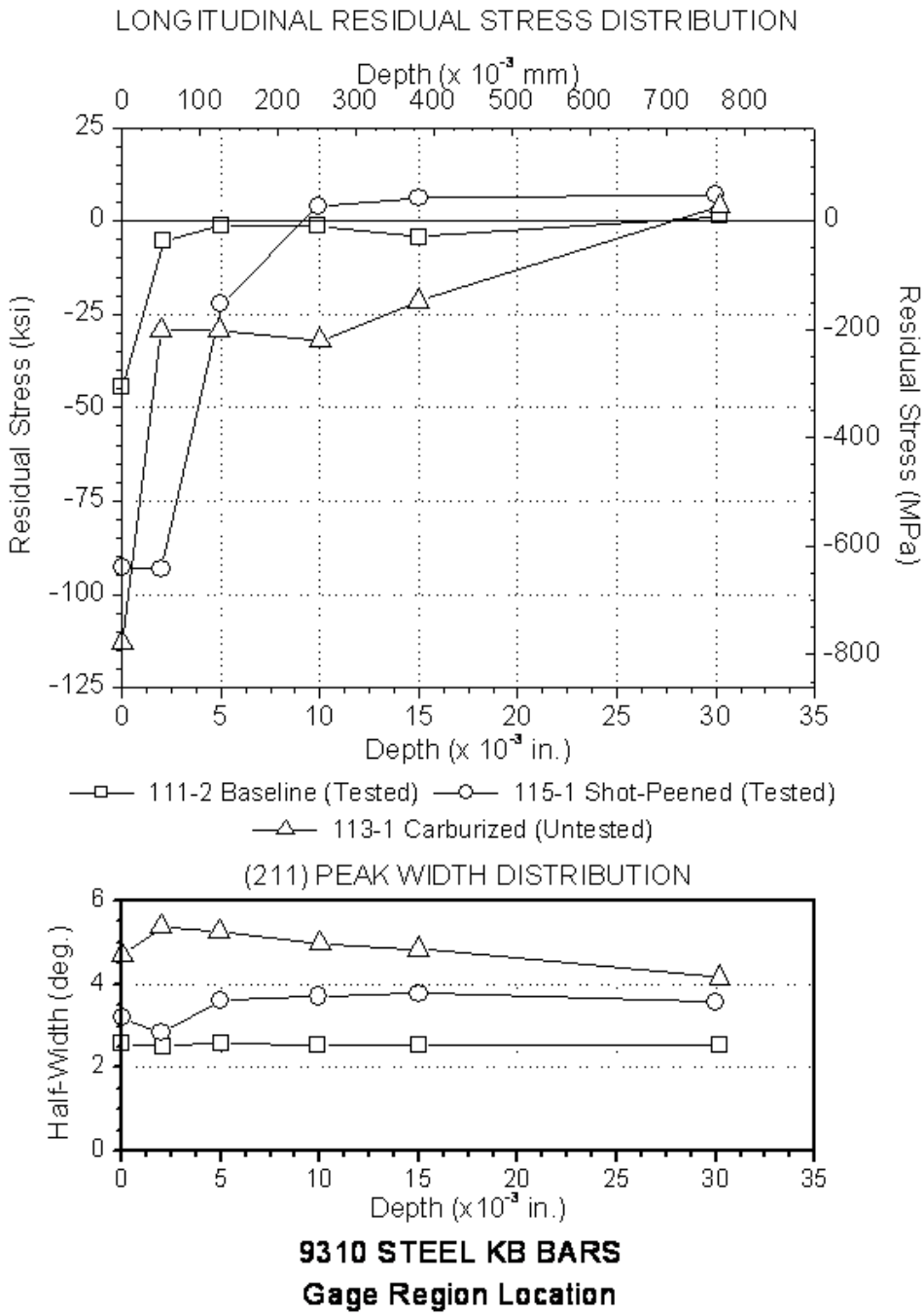

Figure D-2. Residual Stress Measurements of 9310 Steel Samples

The error shown for each residual stress measurement is one standard deviation resulting from a random error in the determination of the diffraction peak angular positions and in the empirically determined value of $E/(1 + \nu)$ in the <211> direction. An additional semisystematic error on the order of ±2 ksi (±14 MPa) may result from sample positioning and instrument alignment errors. The magnitude of this systematic error was monitored using a powdered metal, zero-stress standard in accordance with ASTM E 915 and was found to be +1.4 ksi (+10 MPa) during the course of this investigation.